The Dissertation Committee for Shravan Gowrishankar Certifies that this is the approved version of the following dissertation:

CHARACTERIZATION OF DELAMINATION IN SILICON/EPOXY SYSTEMS

Committee:

Kenneth M. Liechti, Supervisor

Rui Huang

K. Ravi-Chandar

Paul S. Ho

Desiderio Kovar

CHARACTERIZATION OF DELAMINATION IN SILICON/EPOXY SYSTEMS

by

Shravan Gowrishankar, B.Tech

Dissertation

Presented to the Faculty of the Graduate School of

The University of Texas at Austin

in Partial Fulfillment

of the Requirements

for the Degree of

Doctor of Philosophy

The University of Texas at Austin

May 2014

Dedication

To my late father, C. Gowrisankaran, for inspiring me to pursue my PhD

My mother, Jayanthi, for her love and support at every step

My brother, Ashwin, for his encouragement and support

And to my loving wife and best friend, Phrabha Shalini.

Acknowledgements

I would like to express my most sincere appreciation and gratitude to my supervisor, Dr. Kenneth Liechti, without whose valuable guidance this work would not have been possible. His insightful ideas and strong encouragement have been vital during all the difficult times over the years. I am earnestly grateful for the research experience I have obtained during the course of my work in his lab.

I am grateful to Dr. Huang, Dr. Ravi-Chandar, Dr. Ho and Dr. Kovar for their readiness to act as my dissertation committee. My sincere thanks to Dr. Huang for the constant interest and support he has shown towards my research work. His ideas have been very astute and have motivated me a lot over the years. I am grateful to Dr. Ravi-Chandar for his guidance in the DIC analysis. I would like to extend my gratitude to Dr. Kovar for allowing me to use the optical profilometer in his lab and for his support during difficult times in the early stages of my PhD. My earnest thanks to Dr. Ho for the many interesting discussions during the SRC review meetings. My acknowledgements to the Semiconductor Research Corporation (SRC) for funding my research. I would further like to thank the Department of Aerospace Engineering and Engineering Mechanics and the Department of Mechanical Engineering for providing me teaching assistantships to fund myself during my time here.

I would like to thank all the faculty whose interesting courses I have taken over my years at the University of Texas at Austin. They have been very helpful in broadening my knowledge in both Materials Science and Engineering and Engineering Mechanics.

My sincere acknowledgements to Joe Pokluda, Travis Crooks, David Gray and Ricardo Palacios from the machine shop who helped me to fabricate the parts of the loading device. I would like to wholeheartedly thank Pablo Cortez who helped me with

the electronic and mechanical problems we faced while developing the loading device. My thanks to Scott Messec for his help in tackling software issues.

I would like to thank the National Science Foundation (Grant No. 0618242) for funding the Kratos Axis Ultra XPS used in this work. My sincere thanks to the Center for Nano and Molecular Science and Technology, the Texas Materials Institute and the Welch Foundation in support of the facilities utilized in this work.

I would like to thank all the graduate coordinators and administrative associates who have helped me with equipment procurement, assistantship appointments and other logistics during my time here.

Special thanks to my friend and colleague Seung Ryul Na for all the brainstorming discussions that we have shared over the years. I am fortunate to have had such a helpful and friendly lab member. My gratitude to Thomas Mauchien and Uriel Garcia for helping me with the determination of the epoxy material properties. I would also like to thank all my colleagues (past and present) for making the work place such a pleasant environment. I could not have asked for a better atmosphere.

I have been quite fortunate to have made numerous friends during my time here. I would like to specially thank Dr. Kumar Appaiah, Harsha Kumar Maddur Chandrashekar, Dr. Lavanya Mohan. Aswin Balasubramanian, Dr. Ganesh Iyer, Dr. Apurva Chunodkar, Padmini Rajagopalan, Akarsh Simha, Sivaramakrishnan Swaminathan and many others who have made my life here at Austin very enjoyable.

I would not be the person I am today without the unconditional support and love of my family. Despite each of us being in different places, I could not have endured the PhD journey without them playing a vital role in keeping me focused and motivated. I am supremely grateful to my mother and brother for constantly supporting me in all my decisions and believing in me throughout my life. I am extremely thankful to my late

father for inspiring me to pursue my PhD and being such a wonderful role model. I would also like to express my gratitude to my in-laws for their moral support and belief in me.

I am sure I would not have accomplished much without the love and support of my best friend and wife, Phrabha. She has been my inspiration and my role model for all my years here. I cannot even begin to thank her for her patience, encouragement and everything she has done to make my life better.

Characterization of Delamination in Silicon/Epoxy Systems

Shravan Gowrishankar, Ph.D

The University of Texas at Austin, 2014

Supervisor: Kenneth Liechti

Microelectronic devices are multilayered structures with many different interfaces. Their mechanical reliability is of utmost importance when considering the implementation of new materials. Linear elastic fracture mechanics (LEFM) is a common approach that has been used for interfacial fracture analyses in the microelectronics industry where the energy release rate parameter is considered to be the driving force for delamination and the failure criterion is established by comparing this with the interface toughness. However this approach has been unable to model crack-nucleation, which plays an important part in analyzing the mechanical reliability of chip-package systems. The cohesive interface modeling approach, which is considered here, has the capability to model crack nucleation and growth, provided interfacial parameters such as strength and toughness of the system are available. These parameters are obtained through the extraction of traction-separation relations, which can be obtained through indirect hybrid numerical/experimental methods or direct experimental methods. All methods of extracting traction-separation relations require some local feature of the crack-tip region to be measured. The focus in this doctoral work has been on the comparison of the two methods for a mode-I DCB experiment and on the development of a universal loading device to extract mixed-mode traction-separation relations at different mode-mix values. The techniques that have been adopted for the local measurements are infrared crack

opening interferometry (IR-COI) and digital image correlation (DIC). Apart from the global measurements of load-displacement (P-Δ), local crack-tip parameters were measured using IR-COI or DIC. The combination of global and local measurements gave the relations between the fracture driving force (energy release rate or J-integral, J) and crack opening displacements, which were used to obtain the local tractions. IR-COI is an extremely useful technique to image and measure local crack-tip parameters. However, as IR-COI is restricted to normal measurements, the loading device was configured to accommodate a DIC system in order to make both normal and tangential measurements. In addition to measurements, fracture surface characterization techniques such as atomic force microscopy (AFM), profilometry and X-ray photoelectron spectroscopy were used to observe the fracture mechanisms.

Table of Contents

List of Tables

List of Figures

CHAPTER 1: INTRODUCTION

Technological improvements of today's microelectronics industry have been a nucleus for the development of numerous innovative materials and new interfaces. Vital to the long term durability and life predictions associated with microelectronics assemblies is a thorough understanding of interfacial failure mechanisms and debonding behavior of interfaces within these systems. Since the advent of the flip-chip packaging process (Miller 1969), the need for the predicting of mechanical reliability has increased. The primary reason for this added importance is the development of the epoxy underfill, which bonds the chip to the board (Suryanarayana et al. 1991). The principal idea here is to bond the chip with the substrate by incorporating a material that mitigates the thermal mismatch between the substrate and the chip, which tends to be quite extreme. The presence of this underfill has been shown to considerably increase the reliability of the assembly, provided that the structural integrity of the adhesive bond is maintained. As with any modern technology, the study of these materials requires an integration of various areas of research in order to obtain proper understanding of the behavior of the materials,their interfaces and the corresponding adhesion mechanisms. Fracture mechanics has proven itself to be an accepted approach in in the study of interfacial failure and predictions of durability and reliability.

From a mechanics perspective, microelectronics packaging technology has led to a wide array of fundamental and applied research. Significant growth has been observed in the field of interfacial fracture such as the development of fracture mechanics of layered materials (Hutchinson and Suo 1992, Thouless 1994, Dauskardt et al. 1998, Volinsky et al. 2002, Yu and Hutchinson 2002, Kamer et al. 2011). Furthermore, to increase understanding of non-linear material debonding, major innovations have been

made in computational techniques such as the development of cohesive zone models. The application of cohesive zone models through computational tools, introduced by Needleman (Needleman 1987, Needleman 1990), has been extensively studied by many groups (Tvergaard and Hutchinson 1992, Williams and Hadavinia 2002, Feraren and Jensen 2004, Li et al. 2006, Valoroso and Champaney 2006, Park et al. 2009). Furthermore, numerous methods for experimental testing based on material, geometry and industry (Chu et al. 1985, Liechti and Hanson 1988, Reeder and Crews Jr. 1990, Chai and Liechti 1991, Chai 1992, Hutchinson and Suo 1992, Liechti and Liang 1992, Volinsky et al. 2002, Birringer et al. 2011) have been developed over the years to characterize various interfaces. Moreover, the advancements in cohesive zone models has also led to the development of hybrid experimental/numerical techniques that integrate both experiments and simulations (Chai and Liechti 1991, Swadener and Liechti 1998, Mohammed and Liechti 2000, Mello and Liechti 2006, Sorensen et al. 2008, Gain et al. 2011, Shen and Paulino 2011).

1.1 INTERFACIAL FRACTURE MECHANICS

Interfacial fracture mechanics can be broadly classified into two main approaches: a linear elastic fracture mechanics (LEFM) perspective and a cohesive zone model (CZM) approach. The interest in interfacial fracture mechanics from the linear elasticity standpoint can be traced back to the pioneering work of Williams (Williams 1959), who studied the stresses ahead of a crack between two dissimilar isotropic materials. Since then, extensive research has gone into the development of interfacial mechanics from a linear elasticity perspective (Rice and Shih 1965, Rice 1968, Hutchinson et al. 1987, Rice 1988, Hutchinson and Suo 1992) where solutions to interfacial fracture problems have been obtained. Though all the solutions were obtained in the realm of linear elasticity,

they could still be applied to problems involving elastic-plastic materials to determine the stresses outside the plastic zone as long as it was relatively small. The major issue that separates interfacial crack tip solutions from the corresponding elastic fracture mechanics for monolithic materials is the extent of dissimilarity (Dundurs 1969) between the two materials that create the interface. When this dissimilarity is less, any coupling between the normal and shear components of the stresses can be neglected, which yields the solution based on classical elastic fracture mechanics concepts developed for homogenous materials. However, when the dissimilarity between the two materials increases, this coupling effect can no longer be ignored. Furthermore, this leads to the presence of oscillatory singularity in the solutions which suggests interpenetration of the crack faces at distances very close behind the tip (Williams 1959). However, solutions (Comninou 1977, Dundurs 1978, Comninou 1979) which account for this contact have shown that this zone is small compared to relevant crack tip features like the plastic zone or fracture process zone for most loading conditions (Rice 1988, Hutchinson and Suo 1992). However, this effect does dominate when a large shear loading component is involved.

In general, the proportion of the shear component in comparison to the normal component is defined in terms of a phase angle, ψ also referred to as the mode-mix. As a consequence of the oscillating singularity, the measure of the mode-mix introduced for interfacial cracks involves an arbitrary length scale which can be related to the position ahead of the crack tip where the mode-mix is obtained. The definition of mode-mix for an interface crack also depends on the material property of the adherend and adhesive that form the interface. Anisotropy of either material leads to the need of generalized Dundurs parameters of elastic modulus mismatch and bulk modulus mismatch which vary based on the direction of loading (Ting 1995). Furthermore, the definition of mode-mix varies

based on the approach used. A discussion of certain definitions of mode-mix is provided in section 3.3. The interfacial toughness as defined by linear elastic fracture mechanics is essentially a function of the mode-mix (Cao 1989, Wang 1990, Chai and Liechti 1992). Determination of this function not only offers predictability of toughness at different mode-mix values but also defines a criterion for interfacial crack propagation.

Cracks at bi-material interfaces and cracks in the adhesive layer of sandwich specimens have often been characterized using the approach of linear elastic fracture mechanics. Certain conditions cause the crack to deviate away from the interface (such as when the interface is much tougher than the adherend or the adhesive). This kind of situation has been researched in terms of a sub-interface crack paralleling the interface (Hutchinson et al. 1987, Marsavina and Piski 2010). Furthermore, the effect of the mode-mix on the crack depth in a sandwich specimen was demonstrated by Fleck and coworkers (Fleck et al. 1991) where the Dundur's parameters play a significant role in determining the crack depth for a specific mode-mix. Moreover He and Hutchinson studied the deviation of a crack approaching an interface providing different conditions where the crack could deviate away from the interface or propagate in the interface (He and Hutchinson 1989).

Owing to the availability of such numerous solutions, the current approach to characterizing the durability of the interfaces in layered structures is often by way of linear elastic fracture mechanics. However, limitations to this approach can arise, especially for interfaces between thin layers and materials with inelastic properties. In addition, the LEFM approach lacks the ability to model crack nucleation and propagation. Furthermore, an initial flaw is always a requirement in the course of application of LEFM to any problem. In this regard, the cohesive zone model tends to offer attractive features.

The cohesive zone model, first proposed by Dugdale and Barenblatt (Dugdale 1960, Barenblatt 1962) in order to describe the near crack tip behavior in monolithic bodies, has gained popularity in recent years for modeling crack nucleation and propagation especially since the tremendous growth of commercial finite element modeling software. When it comes to modeling quasi-brittle structural behavior with a non-negligible process zone, cohesive zone models have become established as the preferred route. They are also attractive for modeling interfacial crack growth at interfaces mainly because the crack is predetermined. Needleman (Needleman 1987) pioneered the application of cohesive zone modeling to interface fracture. The resulting development of the topic and applications of the concept have been reviewed thoroughly in the literature (Elices et al. 2002, Planas et al. 2003, Volokh 2004, Alfano 2006, Song et al. 2008, Park and Paulino 2011).

Furthermore, cohesive zone models have been effective in modeling not only interfacial delamination as shown by many groups (Shirani and Liechti 1998, Swadener and Liechti 1998, Choi et al. 2001, Feraren and Jensen 2004, Li et al. 2005, Mello and Liechti 2006, Valoroso and Champaney 2006, Parmigiani and Thouless 2007), but also a plethora of other interface problems such as crack nucleation at bi-material corners (Mohammed and Liechti 2000) and delamination of composites (Sørensen and Jacobsen 2003, Li et al. 2005, Li et al. 2006, Moroni and Pirondi 2011). However, a fundamental requirement of any cohesive zone model is the knowledge of material parameters defining the cohesive interactions of the interface in order to make meaningful predications. In addition, the criteria for mixed-mode damage initiation and fracture must be determined, which may then be used to simulate mode-dependent fracture processes (Li et al. 2006, Högberg et al. 2007, Parmigiani and Thouless 2007, Zhu et al. 2009).

The cohesive interactions between the crack faces are generally represented as tractions defined as a function of the displacement between the crack faces (separation) As shown in Figure 1.1 this traction-separation relation can take on different forms. One of the earliest traction-separation relations developed, the Dugdale model (Fig 1.1a) (Dugdale 1960) is an idealized traction-separation relation comprised of a constant traction region before failure at the critical displacement, δ_c. The trapezoidal (Fig. 1.1b) and the bilinear (Fig 1.1c) forms of the traction separation relation are relatively similar to each other, consisting of an elastic region before reaching the peak strength value. At this point the trapezoidal form contains a region of constant traction. This is then followed by a softening region before complete failure is achieved. In general however, the form of the traction-separation relation is based completely on the method of extraction but can be represented by a generic form as shown in Figure 1.1d.

The extraction of traction-separation relations is generally approached in one of two ways: a direct method and an iterative method. The direct method, as demonstrated by many groups (Stigh and Andersson 2000, Sørensen and Jacobsen 2003, Andersson and Stigh 2004, Sorensen et al. 2008, Zhu et al. 2009), delivers results based mainly on local or multi-scale experimental measurements of crack opening displacements without recourse to extensive numerical analysis. However, the extraction of traction-separation relations obtained through the direct method can be constrained by resolution issues in locating the crack front and measuring the crack opening displacements. The iterative method, on the other hand, determines parameters by comparing numerical solutions from finite element analysis and measurements from experiments. This has been frequently employed in the past by researchers by generally matching local measurements to FEM solutions (Cox and Marshall 1991, Swadener and Liechti 1998, Mohammed and Liechti 2000, Li et al. 2005, Mello and Liechti 2006, Sorensen et al.

2008, Gain et al. 2011, Shen and Paulino 2011) or by comparing global measurements like load-displacement behavior or a uniaxial tensile test response to numerical solutions (Elices et al. 2002, Kandula et al. 2005).

1.2 INTERFACIAL FRACTURE TEST METHODS

In order to fully characterize any interface, the interfacial properties must be determined for the complete range of loading configurations from a pure normal (mode-I) to a pure shear (mode-II) condition. The definition of ψ varies depending on the approach (LEFM or CZM) and the respective parameters used. A discussion on some definitions of ψ and their significance is presented in Chapter 3.

A wide array of fracture specimens and loading configurations have been developed over the years (Suo and Hutchinson 1988, Reeder and Crews Jr. 1990, Chai and Liechti 1992, Davidson and Sundararaman 1996, Birringer et al. 2011). In the case of adhesive joints, composites and other laminated structures, beam type geometries have been frequently adopted. The double cantilever beam (DCB), the end notched flexure (ENF) test (Barrett and Foschi 1977, Chai and Mall 1988), the end-loaded split (ELS) test (Wang and Vukanh 1996) and the mixed-mode bending (MMB) (Charalambides et al. 1989, Charalambides 1990) are some of the commonly used beam geometries in fracture mechanics. When adhesive joints are considered, the use of sandwich structures (Suo and Hutchinson 1988, Liechti and Freda 1989, Liechti and Marton 2002, Bing and Davidson 2010) comprising of stiff adherends bonded by the adhesive proves to be useful as they can be subject to loading configurations analogous to homogeneous specimens with relative ease.

In order to obtain the mode-I material parameters required for the cohesive zone model, one of the most commonly used specimens is the double cantilever beam (DCB) specimen (Kanninen 1973, Chow et al. 1979, Williams 1989, Zhu et al. 2009). The main advantage of using the DCB specimen is that a nominally mode-I loading can be applied to the crack, which allows the mode-I toughness of the interface to be measured. However, the DCB specimen can also be used with an uneven bending moment (Sørensen and Kirkegaard 2006) or loaded in an asymmetric manner (Mangalgiri et al. 1986, Sundararaman and Davidson 1997) in order to measure mixed-mode fracture properties. Other commonly used mixed-mode specimens include the four point bend test (Charalambides et al. 1989, Charalambides 1990) and the end loaded split (Hutchinson and Suo 1992, Wang and Vukanh 1996). The nature of mixed-mode experiments has always required the need for innovation which has brought about a lot of modifications to previously existing mixed-mode test specimens (Reeder and Crews Jr. 1990, Davidson and Sundararaman 1996, Bing and Davidson 2010). Each specimen however, has its own advantages and limitations with respect to the mode-mix range provided, the material system dependence and the ease of implementation.

Despite the existence of numerous fracture test specimens and loading configurations, the major obstacle in the implementation of cohesive zone models is that they require specific material parameters experimentally measured at the local level in order to make meaningful predictions. Crack opening interferometry (Liechti 1993), digital image correlation (DIC) (Pan et al. 2009) and laser generated stress pulses (Pronin and Gupta 1998) are some of the numerous techniques that have been developed over the past few decades in order to measure local crack tip parameters (for e.g. crack opening displacements) and extract interfacial properties. The choice of any experimental

technique depends on the material under consideration, the resolution and accuracy requirements and scale of testing.

Interferometry pertains to a family of techniques which make measurements using the principle of wave interference. Focusing on fracture mechanics, crack opening interferometry has been widely used to characterize crack tip behavior in glass/adhesive systems (Chai and Liechti 1992, Liechti 1993, Swadener et al. 1999, Mello 2003), copper/sapphire bi-crystals (Kysar 2001) and functionalized silicon surfaces (Na et al. 2011). One of the main advantages of interferometry when applied to interfacial fracture specimens is the three-dimensional information it provides. Tracking crack opening and propagation can be conducted for the entire crack front down to low resolutions depending on the wavelength of the light source. In this work, the silicon/epoxy system was characterized using interferometry with infrared (IR) light because of the IR transparency of silicon. Naturally, the major limitation of interferometry is that it is restricted to the materials transparent to the light source. Moreover, the surface of the material must be smooth and reflective. Furthermore, interferometry can be applied only in the measurement of normal crack opening displacements and is unable to provide information about the tangential behavior of the crack tip.

The digital image correlation (DIC) technique is another optical method that has the capability of measuring full-field two-dimensional or three-dimensional surface deformations. The technique of correlating images can be traced back to the 80s when the technology of computers was still in its infancy (Chu et al. 1985). With the development of high resolution image acquisition systems and high speed computational tools, tremendous growth has been observed in the development of DIC. In the past decade, the DIC technique has improved not only in its capability of making high accuracy measurements but also in its application range. Starting with in-plane measurements of

planar surfaces with a single image acquisition system, DIC has evolved to 3D-DIC (Luo et al. 1993) where binocular stereovision is incorporated in the image acquisition process. Certain groups (Bay et al. 1999, Smith et al. 2002) have also proposed a digital volume correlation technique (DVC) which is essentially a three dimensional extension of the 2D-DIC utilizing techniques like X-ray tomography to make measurements. Applications of DIC are extensive and are expanding with the enormous growth in technology (Chu et al. 1985, Sun et al. 1997, Vendroux and Knauss 1998, Comer et al. 2013). Groups have demonstrated the power of DIC in microelectronic packaging by the studying problems such as fatigue in solders (Sun and Pang 2008), deformation in interconnects (Kehoe et al. 2006), extracting thermal coefficient of expansion (Bing et al. 2009) and extracting fracture toughness values of the underfill/ chip interface (Shi et al. 2007). Furthermore, a miniature mixed-mode bending fixture conducted within a scanning electron microscope was demonstrated where the SEM images were correlated to observe microscopic delamination mechanisms (Kolluri et al. 2009). More recently, DIC has been utilized in tandem with numerical simulations in order to extract interfacial properties (Shen and Paulino 2011) in an iterative manner. As the technique can be applied to any surface with a random pattern, in this work, 2D-DIC has been incorporated to measure the normal and tangential crack opening displacements in mixed-mode experiments.

1.3 ADHESION MECHANISMS

The science of adhesion has been studied for quite a few decades and based on mechanisms observed, many theories have been put forward to rigorously define adhesion between two materials. Even though the focus of this work has been on the study of interfacial fracture between silicon and epoxy, in order to rigorously understand

the concept of adhesion, the aspects of surface chemistry and physics, rheology, polymer chemistry and physics and fracture phenomena must be taken into account for a full interpretation of the data. However, this multifaceted quality of adhesion makes the development of a unified theory quite difficult (Bateup 1981). Adhesion mechanisms between any two materials fall into five fundamental theories as reviewed by many researchers in the past (Wake 1978, Kinloch 1980, Bateup 1981, Allen 1993, Ohring 2001). These are described in brief below:

1. Adsorption
2. Surface reactions (chemical bonding)
3. Mechanical interlocking
4. Diffusion
5. Electrostatic bonding

Adsorption is the most widely accepted theory of adhesion (Kinloch 1980) where, provided there exists sufficient intermolecular contact between the adhesive and the adherend, the two materials will exhibit adhesion because of the presence of surface forces acting between the molecules. The adhesion increases with the proximity of the two molecules as per the Lennard-Jones model. Secondary forces such as van der Waal's forces play a major role in attracting the molecules of electrically neutral bodies together. The adsorption theory holds true when good wettability can be achieved between the adhesive and the adherend as this provides the necessary intermolecular contact between the two materials. Furthermore, the adsorption mechanism can be further classified into physisorption and chemisorption. Physisorption is what was just described and chemisorption is explained by the theory of surface reactions at the interface between the adherend and the adhesive.

Surface reactions or chemical bonding suggests the formation of primary chemical bonds across the interface. The curing process involves the occurrence of chemical reactions at the interface between the two materials. Surface reactions form much stronger bonds than the physisorption mechanism as the chemical bond strength tends to be much higher than the secondary forces that hold the adherend and adhesive together (Gent 1981, Schmidt and Bell 1986). Frequently, coupling agents such as silanes and other adhesion promoters are employed to enhance the surface reactions between the materials (Gledhill et al. 1990, Shijian and Wong 2000). An example of the surface reaction based adhesion mechanism is the adhesion of epoxy to metal oxide layers.

Mechanical interlocking occurs when the substrate or adherend has a rough surface with surface irregularities like crevices and pores which are used by the adhesive as mechanical keys to make adequate contact prior to curing. Naturally, the effectiveness of mechanical interlocking is based on the ability of the adhesive to penetrate the pores on the adherend surface. Furthermore, surface treatments such as abrasion must be conducted on the adherend surface in order to provide enough surface irregularities (Packham et al. 1974, Ohring 2001).

The diffusion based mechanism, originally proposed by (Voi͡ut͡skiĭ 1963) is applicable only to mutually soluble materials where the adhesive diffuses into the adherend and thus forms a bond. The diffusion based mechanism has proven to be effective in polymer-polymer systems where mutual diffusion across the interface between two polymers occurs (Gent et al. 1997). This mechanism requires the molecules of the adhesive and the adherend to possess sufficient mobility and mutual solubility.

Electrostatic bonding is a mechanism where the exchange of charge across the interface contributes to the adhesion. The concept is similar to that of a capacitor where electrical double layers consisting of oppositely charged planes develop and exert the adhesive

force. However, the adhesive forces exerted by the mechanism is considerably small compared to the contributions of the other mechanisms.

Based on the material system, the interface that is formed could be an abrupt interphase where the transition from the adherend to the adhesive, in this case from silicon to epoxy is distinct. A compound interface could be formed due to an adsorption mechanism (physisorption or chemisorption through surface reactions) where an interphase (Sharpe and Schonhorn 1964, Sharpe 1972) is formed between the materials which displays a gradient in the properties between the adherend and the adhesive. Diffusion mechanisms generally create a diffusion interface which results in a much thicker interphase region. Mechanical interlocking between the adhesive and the adherend creates a mechanically coupled interface which depends on the material system and the surface roughness of the adherend and the penetrating ability of the adhesive. Depending on the material system that is being dealt with, the interface formed varies. Furthermore, there could be a mixed interface formation where a compound interface or interphase can form along with mechanical interlocking of the components (Drzal 1986, Schmidt and Bell 1986).

1.4 OBJECTIVES

The presence of the underfill (an epoxy based adhesive) in the flip-chip packaging process has been shown to be very beneficial as it has shown to reduce the shear strain in the solder bumps of the package and also mitigate the thermal mismatch between the silicon die and the organic printed circuit board (Suryanarayana et al. 1991, Ho et al. 2004). From a reliability point of view, however, this has shifted concern to the issue of debonding of the underfill from the silicon die. Several researchers have worked on the characterization of interfacial adhesion between the silicon die and the underfill in the

flip-chip package through experiments (Fan et al. 2002, Sham and Kim 2003, Shi et al. 2007) and simulations (Auersperg et al. 2010, Yang et al. 2011, Hölck et al. 2012, Yang et al. 2013).

However, the development of new experimental techniques to extract the traction-separation relations have been relatively scarce. Furthermore, the establishment of a common mixed-mode fracture criterion which not only predicts the damage initiation of the material but also provides a damage evolution function through experimental measurements has been equally rare. Hence, the main objectives of this doctoral work are:

1. Exploring the determination of the mode-I traction-separation relations of the silicon/epoxy interface using direct and iterative methods. The direct method combined infra-red crack opening interferometry (IR-COI) measurements with an augmented analytical solution for J-integral to extract the traction-separation relation. Next, an iterative method was adopted to compare the same measurements with finite element simulations using two types of candidate traction-separation relations. The results from the two methods are compared to conclude with remarks on their effectiveness and limitations.

2. Developing a loading device suitable for IR-COI and DIC measurements and a fracture specimen to conduct mixed-mode fracture experiments on silicon/epoxy interfaces. A direct method of extracting the mixed-mode traction-separation relations is demonstrated wherein the local measurements from experimental techniques of IR-COI or DIC are combined with the global measurements of load and displacement in order to extract mixed-mode traction-separation relations. Based on the results, the mode-dependence of

the interface is studied and an effort is made to establish a fracture criterion for the silicon/epoxy interface. Furthermore, the fracture surfaces of the specimens in both tasks are characterized using techniques such as atomic force microscopy (AFM) and profilometry.

CHAPTER 2: MODE-I EXPERIMENT

The focus of this chapter is on a nominally mode-I experiment that was conducted on silicon/epoxy sandwich specimens loaded in a DCB wedge test configuration in order to obtain the mode-I interfacial traction-separation relation. The experimental component comprises of the specimen preparation, the technique adopted and the measurement procedure. Two modeling approaches were taken to understand the interfacial crack growth in the DCB wedge tests. The first was an analytical approach by combining a cohesive zone model with simple beam theory. The second was a numerical model built using the finite element method in ABAQUS® that accounted for the two silicon strips, the epoxy layer, and the adhesive interactions across the silicon/epoxy interface. The traction-separation relations for the silicon/epoxy interface were then obtained and compared.

2.1 DOUBLE CANTILEVER BEAM WEDGE TESTS

As discussed earlier, the double cantilever beam experiment is one of the most common tests to obtain the mode-I behavior of any interface. The main factors dealt with in this section are the extraction of the bulk material properties of silicon and epoxy, the experimental approach adopted and the measurements made in the course of the experiment

2.1.1 Material Properties

The properties of the materials used in the experiments were extracted by using standard testing techniques. In this work, the constitutive behavior was obtained by conducting three-point-bend tests on silicon strips and uniaxial tensile tests on epoxy

coupons. These material properties were then utilized in the analysis of the fracture experiments and in the construction of the finite element model. The experiments and the material properties obtained have been described below for both silicon and epoxy.

Silicon

The orientation of silicon is of importance as single crystal silicon exhibits anisotropy. However, it has been shown (Riney 1961, Brantley 1973) that for a silicon wafer with a (111) orientation, elastic constants for all orthogonal directions are invariant in plane. The tensile modulus of the silicon was obtained by conducting a three-point bend test on 50×5 mm silicon strips of two nominal thicknesses that have been used in the experiments (280 and 585 μm). Using Euler beam theory, the stress-strain behavior of the silicon strips was extracted from the load-displacement data obtained from the test (Fig. 2.1). Based on multiple tests, the in-plane Young's modulus and the fracture strength were 168.3 ± 2.3 GPa and 230 MPa, respectively.

Epoxy

Two epoxies have been used in this doctoral work. Even though both have the same nominal chemical compositions, it became apparent that the additives had changed over time and this affected their mechanical properties. The CIBA-Geigy epoxy that was used in the nominal mode-I experiments was prepared by mixing a resin (modified bisphenol-A epoxy, Araldite® GY502) and a hardener (polyamidoamine, Aradur® 955) thoroughly in a 100:45 ratio by weight. The epoxy used for the mixed-mode experiments was provided by Huntsman ® (Araldite GY502 and Aradur 955-2). These were mixed thoroughly in a 100:35 ratio by weight. Both epoxies were then degassed in a chamber to remove the bubbles in the respective mixtures. The properties of the CIBA-Geigy epoxy

were obtained previously (Liang and Liechti 1996, Swadener 1998) by conducting uniaxial tension and compression tests (Fig.2.2)

The mechanical behavior of the Huntsman epoxy was acquired by conducting uniaxial tensile tests in an Instron universal testing machine. An extensometer and the digital image correlation technique were used in order to measure the strain in the epoxy specimen during the tests. This not only provided the mechanical properties of the epoxy used but also validated the digital image correlation technique that is described in greater detail in Chapter 3. The stress-strain behavior of the Huntsman epoxy is shown in Fig. 2.3. The behavior is considerably different from that of the CIBA Geigy epoxy. The onset of plasticity in the Huntsman epoxy occurred at about 33.4 MPa after which, a mild softening was observed. The epoxy reached a plateau stress of about 27 MPa and eventually failed at around 11% strain. On the other hand, the CIBA-Geigy epoxy yielded at 40.1 MPa, softened to a plateau stress of about 34.3 MPa and failed at 6.7% strain. Table 2.1 summarizes the constitutive properties of the silicon and the two epoxies.

2.1.2 Preparation of Fracture Specimens

A schematic of the specimen geometry and apparatus that were used in the wedge test is shown in Figure 2.4. The specimen consists of two silicon strips joined by a layer of epoxy. The n-type Si (111) wafers used here were polished on both sides to allow the use of IR-COI and were obtained from WRS Materials. The wafers were 50 mm in diameter and nominally 280 μm in thickness. Although silicon wafers can be cut in various directions, the Si (111) is preferred because the (111) plane has the smoothest surface and presents the most dense arrangement of atoms on the surface. An automatic dicer (Disco, model DAD 321) was used to cut the silicon wafers into 45×5 mm strips, which were cleaned individually by ultrasonication in de-ionized water to remove any

particles that may have accumulated during dicing. The top adherend was coated with an Au/Pd thin film from one end of the strip to a length of 15 mm. The mode-I adhesion energy between the Au/Pd coating and the epoxy was fairly small ($\approx 0.07\,\mathrm{J/m^2}$), which allowed an initial crack to form with minimal or no damage ahead of the crack front upon application of the load.

To prepare the specimen, a silicon strip was laid on a Teflon® tape with a 27 μm-thick shim at either end to control the thickness of the epoxy layer. A bead of the degassed epoxy was dropped on the silicon surface and spread out with a spatula. Then the silicon adherend with the partial Au/Pd coating was pressed on the bead with a weight to spread epoxy into a layer between the two silicon strips. The specimen was cured for 3 hours at 65°C and then allowed to cool slowly.

2.1.3 Infrared Crack Opening Interferometry

In the experiments that are conducted for this project, IR-COI has been mainly used to measure the normal crack opening displacements (NCOD), track crack growth and observe the changes in the crack front geometries for both the nominally mode-I and mixed-mode experiments. A brief outline of the IR-COI technique is been given below but a more elaborate explanation as well as other applications of classical interferometry to fracture mechanics can be found elsewhere (Liechti 1993). Figure 2.5 shows a simple ray diagram describing interference between two faces. Considering these two crack faces and assuming the distance AC to be small compared to SD and DP, we can obtain the following relationships between optical paths

$$n_1 SD \approx n_1 SA + n_2 AE \quad \text{and} \quad n_1 DP \approx n_1 CP + n_2 FC\,, \tag{2.1}$$

where n_1 and n_2 are the indices of refraction of the media through which the radiation is passing. From these equations, the optical path difference, δ_0 between rays reflected from the top and bottom crack faces is given by

$$\delta_0 = \left[n_1 \left(SA + CP \right) + n_2 \left(AB + BC \right) \right] - n_1 (SD + DP) . \tag{2.2}$$

This can be simplified to

$$\delta_0 = n_2 \left(EB + BF \right) = 2 n_2 h \cos\gamma , \tag{2.3}$$

where γ is the angle of incidence on the surface at B and h is defined as the separation BD between the two crack faces. The total phase difference is thus given by the sum of the optical path difference and the phase change due to reflection on B, which is:

$$\delta_0 = n_2 \left(EB + BF \right) = 2 n_2 h \cos\gamma \tag{2.4}$$

This is represented by an interference pattern. The dark fringes correspond to destructive interference that is represented by

$$h = \frac{n\lambda}{4 n_2 \cos\gamma}, \qquad n = 0,1,2,3... \tag{2.5}$$

The bright fringes correspond to constructive interference that can be represented by

$$h = \frac{(2n-1)\lambda}{4 n_2 \cos\gamma}, \qquad n = 1,2,3... \tag{2.6}$$

Thus, the normal crack opening displacement for an air filled crack and normal incidence $(\gamma = 0)$ is given by

$$\delta_n = \frac{n\lambda}{2}, \qquad n = 0,1,2,3... \tag{2.7}$$

for dark fringes and for the bright fringes the NCOD is given by

$$\delta_n = (2n-1)\frac{\lambda}{4}, \qquad n = 1,2,3... \tag{2.8}$$

This set of equations defines crack opening interferometry. The resolution of IR-COI in this experimental arrangement is $\lambda / 4 = 260$ nm. The resolution is improved by

measuring the intensity between the dark and bright fringes. An example of this idea is given by (Swadener 1998), where intensity measurements were used to obtain the NCOD between fringes. Thus,

$$\frac{I}{I_{pp}} = \frac{1}{2}\left[\pm 1 \mp \cos\left(\frac{4\pi|\delta_n|}{\lambda}\right)\right], \tag{2.9}$$

where I is the intensity between consecutive bright and dark fringes and I_{pp} is the range of intensity between them.

Validation of IR-COI

As this was one of the first applications of IR-COI, two experiments were conducted to check the validity of this method. The first one was to check if the interference of infrared rays would yield Newton's rings (Fig. 2.6), which can be used to measure the radius of curvature of lenses. The second one was to check the reflectivity of the silicon surfaces by simulating a cracked specimen by placing a silicon strip over a bent silicon beam and measuring the gap between them and then comparing the result with beam theory.

A 0.27 mm-thick Si(111) wafer placed on a 48.59 mm radius glass lens was used for the first experiment. The radius of the lens is estimated by

$$R_m = \frac{r_m^2}{\lambda\left(m + \frac{1}{2}\right)} \tag{2.10}$$

where R_m is the radius of the lens obtained from the fringe whose location is r_m. The index $m = 0,1,2,3..$ corresponds to dark fringes and $m = 0.5,1.5,2.5..$ corresponds to bright fringes. The combination of the 5× objective and camera had an in-plane spatial calibration of 1.19μm/pixel. From the fringes, R_m was found to be 48.43±1.19 mm which compared very well with the 48.59 mm radius of the lens.

In the second experiment, a silicon strip of dimensions 40×5×0.267 mm was placed on a similar silicon strip that was subjected to four-point bending. This produces hyperbolic fringes from which the radius of curvature of the bending can be measured using Equation 2.10 and compared with the radius calculated from beam theory. The measured radius was 170.16 mm and the calculated radius was 169.55 ± 2.01 mm. Furthermore, the angle the hyperbolic tangent makes with the x -axis can be used to obtain the Poisson's ratio (Equation 2.11).

$$\nu = \left(\frac{1}{\tan^2 \alpha} \right) \tag{2.11}$$

A Poisson's ratio of 0.23 for silicon was obtained from the image shown in Fig (2.7). This compares well with published values (Brantley 1973, Dolbow and Gosz 1996) after taking into account the mechanical effects of doping (Hall 1967).

2.1.4 Experimental Procedure

The wedge tests were performed using an infrared microscope (Olympus BH2-UMA) that was fitted with an internal beam splitter and an IR filter (1040 ± 15 nm) to provide the normal incident beam (Fig. 2.4). A digital camera (Lumenera Corporation, Infinity 3) with a resolution of 1392×1040 pixels captured the images (Fig. 2.8a). These were processed to determine the location of the crack front and the NCOD. For the normal incidence provided by the microscope, each transition from a dark to a bright fringe or vice versa indicates an increment in NCOD corresponding to a quarter of the IR wavelength ($\lambda = 260\,\text{nm}$). However, as mentioned before, Eqn. (2.9) uses the measurement of intensities between the dark and bright fringes to measure NCOD even more accurately improving the resolution by almost an order of magnitude, bringing it down to approximately 15 nm for the NCOD measurement.

A reference image was subtracted from every image in order to reduce the effect of the background signal. Figure 2.8b shows an example of the resulting image. Then, the intensity profiles along 15 adjacent pixel rows were extracted using the ImageJ (1.42q) software and averaged over these pixel rows in order to provide some smoothing of the raw data. This was then input to MATLAB® for curve fitting, typically using high order Gaussian curves that provided the best fit to the intensity profile plots (Fig. 2.9). The crack front was identified by tracking the change in the slope of the intensity profile (i.e. the second derivative of the fit) and noting the location at which this change reached the first peak from the bonded region (dark area). This was also taken to be the location of the zero order fringe so that subsequent peaks and valleys corresponded to the locations of bright and dark fringes. The NCOD values were extracted between fringes by inserting the fitted intensity values in Equation (2.9). The average deviation of the data from the fit was used to arrive at the 15 nm uncertainty in the NCOD measurement.

The experiment, a nominally mode-I DCB wedge test configuration, was conducted using a screw-driven wedge that could be inserted and removed under displacement control. The wedge was inserted manually in 0.1 mm steps using a micrometer screw and the axial load was reacted at the un-cracked end of the specimen. The initial crack in the specimen was created when the 83.8 μm-thick wedge $\left(h_w\right)$ was inserted into the specimen at the edge where the Au/Pd coating had been applied. The low adhesion between the Au/Pd film and the epoxy gave rise to immediate delamination at the interface upon insertion of the wedge. This initial delamination arrested precisely at the end of the Au/Pd film, beyond which the silicon/epoxy interface was undamaged. The Au/Pd coating thus provided good control over the initial crack length and the damage state of the interface. However, the initial wedge insertion distance must be carefully judged as insertion of a thick wedge or a deeper insertion of the thin wedge could cause

damage to the silicon/epoxy interface which rendered the specimen unfit for the experiment.

Prior to crack growth, the wedge insertion was applied in 0.1 mm steps with a 120 s interval between them. At least one image of the crack front region was recorded at each step. As the onset of crack growth was anticipated, each loading step was maintained for 10 minutes while a time-lapse feature was used to allow interferograms to be taken at five-second intervals in the crack-front region. After the experiment was completed, the two silicon adherends were completely delaminated in order to observe the fracture surfaces. The fracture surfaces were then characterized by Kratos Axis Ultra X-ray Photoelectron Spectroscopy (XPS) system in order to observe the surface chemistry. The XPS technique basically counts the number of electrons being ejected from a surface that is irradiated by x-rays. The Kratos system used directed an incident beam of Al Kα x-rays onto the specimen and the resulting scattered photoelectrons were detected by a photo-detector. The technique uses the resonant peak characteristic of the binding state of an element in order to provide a spectrum of resonant peaks of different binding states as a function of the binding energy. Furthermore, even though the incident X-rays can penetrate up several hundred microns into the material, the photodetector in the XPS instrument absorbs only the photoelectrons being ejected from the surface. These photoelectrons are elastically scattered from a depth of approximately 10 nm, which provides the high surface sensitivity of the XPS technique. Furthermore, an Agilent 5500 Atomic Force Microscope (AFM) was used in tapping mode in order to observe the topography of the fracture surfaces. The AFM system can be used for observing features from a few angstroms to ~2 microns in size.

2.1.5 Measurements

The crack length a is defined as the distance between the wedge and the crack front (Fig 2.4), which was determined by two measurements: the displacement of wedge insertion u_w and the distance Δa that the crack front advanced from the initial position. Thus,

$$a = a_0 + \Delta a - u_w \tag{2.12}$$

where a_0 is the initial crack length. The fact that interference fringes remained visible throughout growth indicates that crack growth was predominantly interfacial in nature. This does not rule out the possibility of nanometer sized epoxy islands or ligament traces on the silicon side of the interface. Figure 2.10 shows the measured crack length with respect to the insertion displacement of the wedge. As can be seen, with the insertion of the wedge, the crack length decreased linearly to the point when the crack front began to advance and became nearly a constant as the crack growth reached a steady state. An interesting observation from the measurements is that the crack growth seems to exhibit a damped stick-slip behavior. The crack length first increased rapidly and arrested, and then the initial linear behavior resumed as the wedge was inserted further into the specimen until crack front advanced again. The increase in the crack length after the first 2-3 major advances reduced and eventually the crack growth did reach a steady state.

Figure 2.11 sketches the crack tip region and the cohesive zone, defining the coordinate systems used in this study. The origin $x = 0$ is the location of the initial crack front, and $r = 0$ defines the moving crack front. The NCOD at the initial crack front $(x = 0)$ is denoted δ_n^*. A cohesive zone ahead of the crack front $(x > 0)$ is indicated by the interfacial tractions acting to close the opening of the interface. A typical set of NCOD profiles measured during crack opening and growth is displayed in Figure 2.12. As can be observed, the crack front first remained stationary as the crack opened. Once

the crack front began to move forward, the NCOD profiles seemed to retain their shapes, an indication of steady state. Interestingly, the NCOD profiles exhibit a knee-shaped kink close to the crack front. As will be discussed later, the significance of the kink is partly attributed to the presence of the epoxy layer in the DCB specimen.

2.2 MODELING: ANALYTICAL AND NUMERICAL

This section elaborates the numerical and analytical modeling techniques adopted in this work. The concepts behind the cohesive zone model are explained along with cohesive zone simulations of the double cantilever beam experiment that were conducted using the commercial software ABAQUS. Furthermore, an analytical approach is presented where an augmented J-integral formulation are developed based a beam on elastic foundation approach which includes a traction-separation relation.

2.2.1 Cohesive Zone Models

The approach of cohesive zone modeling is particularly suitable for adhesion and debonding of interfaces between dissimilar materials (Hutchinson and Evans 2000). Typically, a nonlinear traction-separation relation is used to simulate crack opening and growth at an interface. Previous studies (Tvergaard and Hutchinson 1992, Feraren and Jensen 2004, Li et al. 2005, Parmigiani and Thouless 2007) have suggested that the strength and toughness are the two most important parameters, and that the shape of the traction-separation relation is secondary. However recent studies (Song et al. 2008, Gain et al. 2011) show that the shape of the traction-separation relation plays an important role in the debonding mechanism when the fracture process zone size relative to the structure increases, especially in quasi-brittle materials.

In general, traction-separation relations can be represented by a functional form $\sigma = f\left(\delta_n\right)$. In the present study, two types of traction-separation relations were used,

one with linear softening and the other with exponential softening, as illustrated in Fig. 2.13. Subject to an opening stress σ, the interface first opens elastically in both cases with the initial stiffness (K_0) until the stress reaches the strength of the interface ($\sigma = \sigma_0$), at which point damage initiation occurs. A damage parameter D is then used to describe the state of the interface, which evolves from 0 to 1 based on damage evolution rules:

$$D = \frac{\delta_{nc}\left(\delta_n - \delta_{n0}\right)}{\delta_n\left(\delta_{nc} - \delta_{n0}\right)} \tag{2.13}$$

for linear softening and

$$D = 1 - \frac{\delta_{n0}}{\delta_n}\left[1 - \frac{1 - \exp\left(-\alpha\dfrac{\delta_n - \delta_{n0}}{\delta_{nc} - \delta_{n0}}\right)}{1 - \exp\left(-\alpha\right)}\right] \tag{2.14}$$

for exponential softening. Here, $\delta_{n0} = \sigma_0 / K_n$ is the critical separation for damage initiation, δ_{nc} is the critical separation for fracture, and δ_n is the maximum separation experienced by the interface element over the entire loading history. The parameter α controls the shape of the exponential softening.

Once $\delta_n > \delta_{n0}$, the damage parameter D increases as the opening displacement increases $\left(0 < D < 1\right)$, and the opening stress is related to the opening displacement through

$$\sigma = \left(1 - D\right) K_n \delta_n \tag{2.15}$$

For the case with the linear softening, when $\delta_{n0} \le \delta_n \le \delta_{nc}$, the stress decreases linearly:

$$\sigma = \sigma_0 \frac{\delta_{nc} - \delta_n}{\delta_{nc} - \delta_{n0}} \tag{2.16}$$

For the exponential softening, this portion of the traction-separation relation follows

$$\sigma = \sigma_0 \left(1 - \frac{1 - \exp\left(-\alpha \left(\frac{\delta_n - \delta_{n0}}{\delta_{nc} - \delta_{n0}} \right) \right)}{1 - \exp(-\alpha)} \right) \tag{2.17}$$

In both cases, when $\delta_n = \delta_{nc}$, $D = 1$ and $\sigma = 0$ indicating that the interface element is fully fractured. During any unloading prior to fracture, the damage parameter remains constant (irrecoverable) and the stress decreases linearly as the opening displacement decreases, with the slope $K = (1 - D) K_n$, as illustrated in Figure 2.13. Any subsequent reloading follows this slope until the softening part of the traction-separation relation is again encountered.

For each traction-separation relation, the fracture toughness is obtained as

$$\Gamma = \int_0^{\delta_{nc}} \sigma(\delta_n) d\delta_n \tag{2.18}$$

For the linear softening model, $\Gamma = \frac{1}{2} \sigma_0 \delta_{nc}$. For the exponential softening, $\Gamma = \frac{1}{2} \sigma_0 \delta_{nc} \gamma\left(\frac{\delta_{n0}}{\delta_{nc}}, \alpha \right)$, with $\gamma(x, \alpha) = x + 2(1 - x) \frac{e^{\alpha} - 1 - \alpha}{\alpha(e^{\alpha} - 1)}$.

Although all the above equations have been written with regard to the opening mode with normal displacements and tractions, to account for the effects of mode-mix, the traction-separation relations can be defined separately for the opening and shearing modes (modes I, II, and III), each with a set of similar parameters. In general, both the criteria for damage initiation and final fracture depend on mode-mix (Mei et al. 2010). In this chapter, however, the effect of mode-mix is ignored, considering predominantly mode I fracture in the DCB specimen. The effect of mode-mix is discussed in detail in Chapter 3.

2.2.2 Analytical Approaches

From simple beam theory, the energy release rate (or J-integral) for a crack in a symmetric DCB specimen (Fig. 2.14a) is

$$J = \frac{12P^2a^2}{E_{Si}h_{Si}^3b_{Si}^2} = \frac{3E_{Si}h_{Si}^3h_w^2}{16a^4} \tag{2.19}$$

where P is the applied force, h_w is the crack opening at the loading point (the thickness of the wedge), E_{Si} is the Young's modulus of the beam, h_{Si} is the thickness, and b_{Si} is the width. Eqn. (2.19) is obtained under several assumptions: (1) the effect of transverse shear is negligible; (2) rotation of the beam section at the crack tip (i.e., root rotation) is negligible; (3) the size of the cohesive zone ahead of the crack tip is negligibly small. These assumptions are typically justified when $a >> h$.

A large number of researchers have suggested corrections to Eqn. (2.19) (Gillis and Gilman 1964, Wiederhorn et al. 1968, Kanninen 1973, Chow et al. 1979, Fichter 1983, Williams 1989, Williams and Hadavinia 2002, Li et al. 2004) taking into account the effects of shear, root rotation and the cohesive zone. The effect of the cohesive zone was found to be significant when the interfacial properties satisfy the condition, $\frac{E\Gamma}{\sigma_0^2 h} > 0.4$, in the regime of large-scale bridging (Bao and Suo 1992, Li et al. 2004).

In particular, elastic foundation models have been used to analyze the effect of elastic interactions across the interface (Kanninen 1973; Chow et al. 1979; Williams 1989; Williams & Hadavinia 2002). The elastic foundation model was extended to include the softening part of the traction-separation relation as an augmented analytical approach for the DCB specimen (Fig. 2.14c).The details are present in previous works (Mei 2011, Gowrishankar et al. 2012)but the key results have been summarized here.

Consider an initial crack in a DCB specimen, where the interface ahead of the crack tip is undamaged $(D = 0)$. As the crack opens up, the interface opens elastically

until the crack tip opening displacement (CTOD, δ_n^*) reaches the critical value (δ_{n0}) for damage initiation. When $\delta_n^* < \delta_{n0}$, the interface ahead of the crack tip behaves like an elastic foundation, and the energy release rate is obtained as

$$J = \frac{12P^2a^2}{Eb^2h^3}\left(1+\xi\frac{h}{a}\right)^2 \tag{2.20}$$

where $\xi = \left(\frac{E}{6K_nh}\right)^{\frac{1}{4}}$. In terms of the loading displacement, the energy release rate is given by

$$J = \frac{3Eh^3d^2}{16a^4}\left(\frac{1+\xi\frac{h}{a}}{1+3\xi\frac{h}{a}+3\xi^2\frac{h^2}{a^2}+1.5\xi^3\frac{h^3}{a^3}}\right)^2 \tag{2.21}$$

For $\xi << \frac{a}{h}$, Eqs. (2.20) and (2.21) recover the simple solution in Eqn. (2.19).

When $\delta_n^* > \delta_{n0}$, a damage zone of length c develops ahead of the crack tip. Within the damage zone $(0 < x < c)$, the damage parameter D varies between 0 and 1 and the interface is in the softening phase. Ahead of the damage zone $x > c$, the interface is undamaged $(D = 0)$ and elastic interactions are active. For a given traction-separation relation, the beam equation is solved for different parts. This solution yields the damage zone size as well as the CTOD. The energy release rate is then calculated by the J-integral over a contour around the crack tip and enclosing the entire cohesive zone (both damaged and undamaged parts). The result however depends on the traction-separation relation. For the bilinear model (Fig. 2.7a), the J-integral is obtained as:

$$J = \frac{2\Gamma\left(\delta_n^* - \delta_{n0}\right)}{\delta_{nc} - \delta_{n0}} - \frac{\sigma_0\left(\delta_n^{*2} - \delta_{n0}^2\right)}{2(\delta_{nc} - \delta_{n0})} + \frac{1}{2}\sigma_0\delta_{n0}, \tag{2.22}$$

where δ_n^* is obtained implicitly as a function of the crack length a and the opening d. For the wedge test (Fig. 1), $d = h_w$ and δ_n^* is a function of the crack length a. The

analytical solution is only valid when $\delta_n^* \le \delta_{nc}$. When δ_n^* reaches δ_{nc}, $J = \Gamma$ and the crack front advances. Subsequently, the crack grows under steady state conditions with a constant crack length $\left(a = a_{ss}\right)$ and a constant damage zone size $\left(c = c_{SS}\right)$.

The calculation of the J-integral is critical for determining the interfacial traction-separation relation. In the analytical approaches being considered here, the J-integral depends on the interfacial properties and cannot be determined precisely without knowing the traction-separation relation a priori. Figure 2.15 plots the J-integral for the wedge-loaded DCB specimen as a function of the crack length, comparing the three different formulae with the numerical results from finite element models. Using Eqn. (2.21), the interaction across the interface is purely elastic, which predicts an energy release rate slightly lower than Eqn. (2.19). Using Eqn. (2.22), the interfacial interaction includes a damage zone. However, the predicted J-integral is nearly identical to Eqn. (2.21), except for the prediction of steady-state crack growth when $J = \Gamma$. Therefore, Eqn. (2.21) may be used as an approximation for the J-integral, which agrees more closely with the finite element simulations than Eqn. (2.19).

2.2.3 FEM Simulations

To simulate interfacial delamination of the wedge-loaded DCB specimen, a two-dimensional, tri-layer finite element model was constructed in ABAQUS, with a layer of cohesive elements (COH2D4) for the interface between the top silicon beam and the epoxy layer. Both silicon beams and the epoxy layer were modeled by plane-strain quadrilateral elements (CPE8R), with linear elastic properties (Young's modulus: $E_{Si} = 168$ GPa and $E_e = 2.03$ GPa; Poisson's ratio: $\nu_{Si} = 0.22$ and $\nu_e = 0.36$). The wedge was modeled as a rigid body with frictionless, hard contact with the surface of

each silicon beam. The traction-separation relation with either linear or exponential softening was used for the cohesive elements. As was shown in Fig. 2.13, the following parameters are required to define the bilinear traction-separation relation: the initial elastic stiffness K_n, the interfacial strength σ_0, and the interface toughness Γ. For the exponential softening, a shape parameter α is required in addition to the other three parameters. It was found that the initial stiffness (K_n) plays a secondary role compared to the other parameters. In this work, the interface stiffness was fixed at $K_n = 2\text{x}10^{15}$ N/m^3, but the strength, toughness and α were varied in order to compare with the experiments.

The simulation was conducted in two steps. First, the silicon beams were given an opening displacement at the fractured end to the point that the wedge could be inserted. Next, with the wedge in between, the beams were further separated by displacing the wedge in the x-direction (Fig. 2.4). Figure 2.16 shows the numerical results from a finite element simulation using the traction-separation relation with $\Gamma = 1.8$ J/m^2, $\sigma_0 = 18$ MPa, and $\alpha = 1$ for exponential softening. In Fig. 2.16a, the NCOD are plotted as a function of x with $x = 0$ at the initial crack tip. As the wedge was inserted toward the crack tip, the crack opened up and a cohesive zone developed ahead of the initial crack tip. In the finite element model, the location of the crack tip can be identified by the damage parameter D, which equals 1 to the left of the crack tip but is less than 1 to the right of the crack tip. As shown in Fig. 2.16b, for each interface element ($x > 0$), D increased from 0 to 1 and crack growth started when the damage parameter of the first interface element reached 1. However, in an experiment, it may not be possible to precisely determine the location of the crack tip as the damage cannot be measured directly. On the other hand, the minimum NCOD that could be measured by the IR-COI technique was about 20 nm. Thus an measured crack tip is defined at the location with $\delta_n = 20$ nm. The crack lengths (a) in Fig. 2.16 were then calculated by Eqn. (2.1) with

Δ being the distance between the measured crack tip and the initial crack tip. In Fig. 2.16c, the NCOD is plotted as a function of r, with $r = 0$ at the location of the measured crack tip that moved as the crack grew. The scale has been magnified in Fig. 2.16c in order to bring out the development of the cohesive zone near the crack tip. The horizontal line corresponds to $\delta_n = 20$ nm that was used to determine the location of the crack tip. By this definition, crack growth started at a crack length of approximately 6.02 mm and reached a steady state at 5.70 mm. The NCOD profiles converged onto the steady state as expected. It is observed that the critical separation ($\delta_{nc} = 237.5$ nm) for the traction-separation relation used in this simulation is much larger than 20 nm. Consequently, normal traction is expected to act along part of the crack surfaces (r > 0), which would decrease the crack opening compared to the traction-free crack surfaces. Prior to the steady state growth, the cohesive zone was not fully developed, and thus the NCOD close to the crack tip were larger than the steady state NCOD. The order was reversed further away from the crack tip.

The distribution of the normal traction along the interface ahead of the initial crack tip is shown in Figure 2.16d. The traction was tensile within the damage zone $(0 < D < 1)$. Beyond the damage zone, the interaction across the interface was elastic with a transition from tensile to compressive, which is characteristic of the behavior of elastic foundations. The peak traction corresponded to the interfacial strength ($\sigma_0 = 18$ MPa). To its right, the traction was lower because it had not reached the strength (thus no damage). To its left, the traction was lower because the interface had been damaged and thus was softening.

The cohesive zone in the present model consisted of a damage zone and an elastic zone. The size of the elastic zone, which depends on the interfacial stiffness, K_n, is typically much larger than the damage zone. The size of damage zone on the other hand

depends on the interfacial strength and toughness. Figure 2.17a shows the steady-state damage zone size as a function of the interfacial strength for a constant toughness ($\Gamma = 1.8$ J/m^2). In general, the steady-state damage zone size decreases as the interfacial strength increases, following roughly the scaling $c \sim \sigma_0^{-2}$ as indicated by the two parallel lines. Moreover, it is found that the damage zone size depends on the shape of the traction-separation relation, with a larger damage zone for exponential softening than for linear softening, although the dependence is relatively weak. In all cases, the damage zone size became insensitive to the strength for relatively high strength values, where the condition of small-scale bridging prevails. The vertical line in Fig. 2.17a indicates the condition $\frac{E\Gamma}{\sigma_0^2 h} = 0.4$ as suggested by (Li et al. 2004). To its left, $\frac{E\Gamma}{\sigma_0^2 h} > 0.4$, large-scale bridging occurs and the damage zone size increases sharply with decreasing strength. Figure 2.11b shows two examples by the finite element simulations, for small-scale and large-scale bridging, respectively.

2.3. RESULTS AND DISCUSSION

As indicated earlier in this chapter, two methods can be used to extract the traction-separation relations: the direct and iterative methods. The former relies on differentiating the J-integral with respect to the measured NCOD at the initial crack tip, while the latter involves comparison of the numerical simulations with the measurements to determine the key parameters of the traction-separation relation. The results from both methods are presented and compared in this section.

2.3.1 Direct Method

The direct method considered here relied on calculating the J-integral with the measured crack length and taking its derivative with respect to the measured NCOD at

the initial crack tip (Sørensen and Jacobsen 2003, Sørensen and Kirkegaard 2006, Högberg et al. 2007, Zhu et al. 2009). Alternatively, with simultaneous measurements of the force and opening displacement at the loading point along with the NCOD at the crack tip, it is possible to determine the traction-separation relation experimentally without using the analytical model (Stigh and Andersson 2000). In the DCB wedge tests, the force by wedge loading was not measured, and the J-integral was calculated based on the analytical approaches in Section 2.2.2, namely

$$J = \frac{3E_{Si}\left(h_w - h_e\right)^2 h_s^3}{16a^4}\omega\left(\frac{a}{h_s}\right), \tag{2.23}$$

where h_w, h_e and h_s are the thicknesses of the wedge, epoxy layer and silicon strip, respectively. The dimensionless function ω may take different forms depending on the analytical model. Here, Eqn. (2.21) based on the elastic foundation model is chosen, since it is a better approximation than Eqn. (2.19) in comparison with finite element simulations (Fig. 2.15). At each loading step, the J-integral was calculated using the measured crack length (Fig. 2.10) and linked with the measured NCOD (Fig. 2.12). In particular, the NCOD at the initial crack tip $\left(x=0\right)$ was denoted as δ_n^* (Fig. 2.11). As a result, the J-integral was obtained as a function of δ_n^* shown in Figure 2.18. For comparison, the J-integral obtained by Eqn. (2.19) is also plotted along with two analytical results for the bilinear and exponential softening models. The parameters for the analytical models were determined from the iterative method in Section 2.3.2.

Within the resolution of the NCOD measurements by IR-COI, there was an initial rise in the value of the J-integral up to 0.66 J/m^2 before δ_n^* became measureable. The increase in J-integral thereafter was still quite steep and reached the maximum of 1.88 J/m^2 before it was stabilized. As shown in Fig. 2.10, the crack front advanced in a stick-slip fashion, leading to the J-integral values oscillating at or below 1.88 J/m^2, which was

deemed the toughness of the silicon/epoxy interface. A polynomial function was used to fit the rising portion of the data in Figure 2.18 followed by the constant value $\Gamma = 1.88$ J/m^2 for the steady state, disregarding the oscillation due to stick-slip.

As shown in Fig. 2.11, with a cohesive zone and δ_n^* as the opening at the initial crack tip, a contour integral enclosing the cohesive zone gives the J-integral as

$$J = \int_0^{\delta_n^*} \sigma(\delta_n) d\delta_n \ , \tag{2.24}$$

where the traction $\sigma(\delta)$ acts across the interface over the cohesive zone. By the path independence of the J-integral, it can also be obtained from Eqn. (2.23). Consequently, the traction-separation relation under mode I conditions can be determined by taking the derivative of the J-integral with respect to δ_n^* (Sørensen and Jacobsen 2003, Sørensen and Kirkegaard 2006)

$$\sigma(\delta_n^*) = \frac{dJ}{d\delta_n^*} \tag{2.25}$$

Note that although this is a mode I dominant case, the elastic mismatch across the silicon/epoxy interface does give rise to small tangential component for the crack opening displacements. Nonetheless, since the normal crack opening displacements were the only ones measured with IR-COI, only the normal tractions were determined by Eqn. (2.25). In this chapter, the measurement of the tangential displacements for the general mixed-mode traction-separation relation was not pursued.

The derivative of the polynomial fit to the data in Figure 2.18 was taken, thereby obtaining the traction-separation relation for the silicon/epoxy interface (Fig. 2.19). The traction-separation relations with linear and exponential softening used in the finite element simulations are plotted alongside. The traction-separation relation obtained via the direct method rises steeply to a strength of 22 MPa. The softening that follows is

relatively sharp and terminated at the critical value of the NCOD, $\delta_{nc} \sim 0.18$ μm. The area underneath the curve gives the interface toughness, $\Gamma = 1.88$ J/m^2. These values give rise to the dimensionless parameter $\frac{E_{Si}\Gamma}{h_s\sigma_0^2} = 2.35$, which places this behavior in the large-scale bridging regime (Li et al. 2004).

2.3.2 Iterative Method

The iterative method assumes a particular form of the traction-separation relation with the key parameters determined by comparing numerical simulations with experimental measurements. For the bilinear traction-separation relation (Fig. 2.13a), three parameters are to be determined; the toughness Γ, the strength σ_0, and the stiffness K_n. For exponential softening (Fig. 2.13b), an additional parameter α is needed. For the present study, the stiffness was fixed at $K_n = 2\times10^{15}$ N/m and the other three parameters were determined in three steps to obtain a traction-separation relation such that resulted in NCOD that were in good agreement with the measured values near the crack tip. In short, the toughness was first determined by comparing the steady-state crack length of the finite element model with the experiment, considering that the other two parameters have less effect on the crack length. Next, the interfacial strength was varied to compare the steady-state NCOD from the numerical simulations with the measurements, and the strength value that yielded the best fit was taken in the second step. Finally, the exponential softening with a particular shape parameter was used to bring the NCOD into better agreement than the linear softening.

As shown in Fig. 2.10, the steady-state crack length obtained from the numerical simulations depends sensitively on the interface toughness. As the first step, a toughness of 1.8 J/m^2 was determined to provide the best agreement with the measured steady-state crack length. The same toughness was obtained for both the bilinear and exponential

softening. On the other hand, it was found that the dependence of the steady-state crack length on the interfacial strength was much weaker (Fig. 2.10b).

Figure 2.20 shows the effect of the interfacial strength on the NCOD during steady state growth using the traction-separation relation with the interface toughness $\Gamma = 1.8$ J/m^2 and $\alpha = 5$ for exponential softening. With $r = 0$ defining the location of the moving crack tip, the numerical results were compared with the measurements and it was found that the strength of 18 MPa provided the best agreement. As noted in Figure 2.12, a knee was present in the measured NCOD. Similar features are also apparent in the numerical results for relatively large strengths ($\sigma_0 > 15$ MPa) in Figure 2.20. This knee may be attributed to two factors: the presence of the epoxy layer and the interfacial strength. When numerical simulations were conducted with a bilayer model without the epoxy (Mei 2011), the knee was absent. The epoxy layer is relatively soft with moderately large deformation near the crack tip as illustrated in Fig. 2.17b. In addition, the knee disappeared as the interfacial strength was low (e.g. $\sigma_0 = 10$ MPa). In this case, the large–scale bridging reduced the stress intensity at the crack tip, resulting in a nearly linear NCOD profile.

It was found that the steady-state NCOD near the crack tip depended slightly on the shape of the traction-separation relation. The comparison is made (Fig. 2.21) using the linear softening and exponential softening with different values of α, with the fixed values for the toughness and strength. For $\alpha \le 5$ there was a noticeable difference in the numerical results for the NCOD, but the results converged for $\alpha > 5$. In comparison with the measured NCOD, $\alpha = 5$ was chosen for the best fit. On the other hand, without the shape parameter, the bilinear traction-separation relation cannot achieve the same level of agreement. Furthermore, the solution based on the traction-separation relation obtained by the direct method, seems to agree well enough in the far field regime of the normal

crack opening displacements but does not obtain the same level of agreement as the exponential traction-separation relation. Consequently, this iterative method yielded a traction-separation relation for the silicon/epoxy interface with $\Gamma = 1.8$ J/m^2, $\sigma_0 = 18$ MPa and $\alpha = 5$.

2.3.3 Fracture Surface Characterization

Fracture surface characterization for the delaminated surfaces was conducted using two main characterization techniques: x-ray photoelectron spectroscopy (XPS) and atomic force microscopy (AFM)

Initial observation of the fracture surfaces under a low magnification optical microscope (Fig. 2.22) seemed to indicate that the gold that was initially deposited on the top adherend has debonded off the top adherend and could be observed clearly on the epoxy surface. During the experiment, as the specimen was being observed by the IR-microscope, the clarity of the interference fringes tends to indicate that the crack path was at or very close to the interface when the crack is traversing the Au/Pd coated region of the specimen. However, the XPS technique gives a clear understanding of the materials present on the fracture surfaces of upper and lower adherends. Each element in the periodic table has a resonant peak at a particular binding energy characteristic of the binding state. For example, silicon generally exhibits Si 2s and Si 2p peaks as shown in Figure 2.23a. Initially, the region of the adherends where the Au/Pd coating was present was first observed. As can be seen in the images shown in Figure 2.23, Au/Pd was observed on both fracture surfaces, which indicates that the Au/Pd was not actually debonded from the epoxy or silicon but was separated from itself during the process of creating the initial crack. It should be noted that the Au/Pd thickness according to the quartz crystal microbalance present in the sputtering chamber where the Au/Pd was

deposited onto the top adherend was only 10 nm. Direct comparison of XPS peak areas is not a good practice as each spectrum recorded by an XPS instrument is characteristic to the number of photoelectrons being ejected from the surface and the ability of the detector to capture these electrons. A better approach is to compare the percentage atomic concentrations which are essentially the ratios of specific intensities to the total intensity of the electrons captured during the procedure. Considering the spectra obtained from the lower and upper adherends, the percentage atomic concentrations of Au and Pd are at least 3 times higher in the epoxy fracture surface. The XPS results hence prove that the epoxy present on the lower adherend almost cleaves the Au/Pd off the silicon adherend leaving a small amount behind. Next, the fracture surfaces beyond the Au/Pd coated region were examined. Figure 2.24 shows the XPS survey scan of the various elements present on both fracture surfaces. Both adherends clearly showed the presence of epoxy by indicating the presence of elements such as C, N, O and Cl. The epoxy present on the top adherend is considerably less in quantity when the percentage atomic concentrations of N 1s are compared. The primary indicators of epoxy are C, O and N. The presence of carbon on the top adherend cannot categorically prove the presence of epoxy as the whole procedure of the sample preparation is done in the ambient atmosphere and the presence of carbon is inevitable. The oxygen peak in the survey scan of the top adherend would represent the native silicon dioxide layer on the silicon adherend, the presence of any moisture on the surface and also, the presence of the epoxy layer if any. Nitrogen, as the only inert element, can be taken as a definite indicator of epoxy on the top adherend. As the XPS technique is restricted to the surface and cannot estimate the bulk composition, comparison of the atomic percentages of N in the silicon/epoxy interface does not yield useful information. However, the top adherend showed a strong presence of silicon in the form of Si 2s and Si 2p peaks. The sampling depth of the XPS technique can be defined

as the depth from which 95% of all photoelectrons are scattered by the time they reach the surface. This sampling depth is approximated as three times the mean free path of the photoelectrons. Since most mean free path values of photoelectrons fall in the range of 1-3.5 nm for an incident Al Kα radiation, the sampling depth for XPS under these conditions is 3-10 nm. The presence of the silicon peak in the survey scan of the top adherend thus indicates that the crack path is less than 10 nm away from the top silicon/epoxy interface.

The topography of the fracture specimens, however, cannot be observed by using XPS. An Agilent 5500 Atomic force microscope was thus used in order to obtain information about the features on the surface of the adherends. Figure 2.25 displays AFM images taken at different regions of the fracture surfaces. As can be observed (Fig. 2.25a), a definite jump in the crack path is observed when the gold line is crossed. This image corresponds to the considerable blunting of the crack that was observed during the experiment just prior to crack growth. Another feature to be noted here is the presence of epoxy ligaments which seem to increase in height near the transition region and once the crack begins to propagate in steady state (Fig 2.25b), they diminish in size and reach an average height of 12 nm. However, when the upper adherend is observed, it shows the presence of ligaments but the density of these ligaments is considerably reduced.

The interfacial properties of the CIBA Geigy epoxy used have been studied previously when bonded to glass (Swadener and Liechti 1998, Swadener et al. 1999) and sapphire (Mello and Liechti 2006). The mode-I toughness levels of the epoxy when bonded with glass and sapphire were 1.8 and 1.5 J/m^2, respectively, similar to the toughness measured for the silicon/epoxy interface.

The interfacial strength however shows a stark difference compared to the cases using glass and sapphire adherends. First, it is observed that the strengths (Table 2.2)

obtained for this silicon/epoxy interface are slightly less than the strength of the epoxy, which was estimated using bulk material properties (Liang and Liechti 1996) to be 40 MPa (Fig.2.3). The glass/epoxy interface (Swadener & Liechti 1998; Swadener et al. 1999) displayed a strength value of approximately 94 MPa, which is more than two times the maximum strength of the epoxy, whereas the sapphire/epoxy interface (Mello and Liechti 2006) had a higher value of approximately 120 MPa, which is about 3 times higher than the 43 MPa maximum strength of the epoxy. As a result, the critical NCODs obtained here for the silicon/epoxy interface (Table 2.2) were much larger than the corresponding values for the glass/epoxy and sapphire/epoxy interfaces, which were 35 and 28 nm, respectively. Both the interfacial traction-separation relations obtained for the glass/epoxy and the sapphire/epoxy interfaces were bilinear in form, which was not the case for the directly determined traction-separation relation for the silicon/epoxy interface.

CHAPTER 3: MIXED-MODE EXPERIMENT

The aim of this portion of the work was to design an experiment to extract the mixed-mode properties of the silicon/epoxy interface. The chapter begins with the design aspects associated with the selected fracture test specimen and then explains the operation of the custom designed loading device that was fabricated. Next, the mixed-mode experiment is described with a section explaining the incorporation of the DIC technique. Subsequent to the experiment, the analysis section describes the approach to determine the mode dependence of the interfacial traction-separation relations. The results obtained are then discussed along with the fracture surface characterization of the mixed-mode fracture specimens.

3.1 DESIGN

The choice of a test specimen and the loading conditions it is subjected to play a vital role in the design of any experiment. Through load-displacement predictions based on the Euler beam theory and linear elastic fracture mechanics, major decisions can be taken about:

1. Specimen dimensions
2. Load cell range
3. Displacement range of the linear actuator

Though this work has been focused on conducting mixed-mode experiments based on the end-loaded-split (ELS) configuration, the device that has been designed can be easily modified to conduct pure mode-II experiments with end-notched flexure (ENF) specimens and mixed-mode flexure (MMF) tests by making changes to accommodate load levels and modifying the loading configuration.

3.1.1 Specimen Geometry

Schematics of three specimen geometries are shown in Figure 3.1. All of them are laminated beam specimens with epoxy sandwiched between double-side polished silicon strips. A gold layer is deposited on the upper silicon strip to form a crack on the interface of interest due to the lower adhesion between the underfill and silicon. The end-loaded split (ELS) specimen (Wang and Vukanh 1996) will be used for fracture experiments at multiple mode-mixes by varying the epoxy thickness (Fig. 3.1a). The lower silicon adherend is wider than the upper one so that it can be clamped along its length to the fixed base of the loading device. The second specimen (Fig. 3.1b) is the end notched flexure (ENF) specimen (Chai and Mall 1988), which provides pure mode-II or shear fracture if the crack is located at the mid plane of the underfill. For an interface crack, the mode-mix is still likely to be mode-II dominant. An intermediate mode-mix is provided by the mixed-mode flexure specimen (MMF) (Charalambides et al. 1989, Charalambides 1990), where the specimen is loaded via a loading block (Fig. 3.1c). The crack front is in the constant moment segment of the carrier beam, making the energy release rate and mode-mix independent of crack length for crack lengths greater than $2h_{Si}$, where h_{Si} is the silicon beam thickness.

3.1.2 Specimen Design

A critical issue in designing a mixed-mode sandwich specimen is the potential for fracture of the adherends prior to interfacial crack growth. The nominal thicknesses of the double sided polished silicon wafers that were available were 300, 600 and 1000 μm. From the adherend cracking perspective, thicker is better, but this is constrained by transparency to infra-red, which diminishes with increasing thickness. One way of approaching this is to increase the wavelength of the IR source as this tends to increase the depth of penetration of the infrared light. However, increasing the IR- wavelength

decreases the resolution as the NCOD measurements, which in turn, are dependent on the wavelength of the IR source (Section 2.1.3). The other constraint is the toughness of the interface. One of the important goals of designing a new device and specimen was to tackle a range of interfacial toughness values ranging from 2 to 200 J/m^2. These constraints were incorporated via linear elastic fracture mechanics analyses and summarized in design curves, which are presented for each case (Fig 3.2). For the ELS specimen, for a given toughness G_c, the load is given by

$$P = \frac{b_{Si}}{a}\sqrt{\frac{G_c E_{Si} h_{Si}^3}{6}} \tag{3.1}$$

Where E_{Si} is the Young's modulus of the silicon and h_{Si} and b_{Si} are the height and width of the upper adherend and *a* is the crack length. The corresponding load point displacement is:

$$\Delta = \frac{Pa^3}{3E_{Si}I_{Si}} \tag{3.2}$$

The load-displacement envelopes for G_c = 2, 20 and 200 J/m^2 and h_{Si} = 300, 600 and 1000 μm are shown in Figure 3.2 for crack lengths ranging from 5 to 20 mm. For G_c = 2 J/m^2, for the thicknesses considered, the load levels ranged from 7.5 to 0.5 N. When the toughness values rose to 20 and 200 J/m^2, the loads ranged from 17 to 1 N and 55 and 4 N, respectively. Based on simple beam theory, the maximum stress in the adherend occurs at the crack front for a specific G_c value . It is given by

$$\sigma = \sqrt{\frac{3E_{Si}G_c}{h_{Si}}} \tag{3.3}$$

and is shown normalized by the allowable strength of silicon (230 MPa, Section 2.1.1) in Figure 3.3 as a function of silicon thickness and interfacial toughness. The results indicate that failure of the silicon is not expected for toughness values of 2 and 20 J/m^2

for strip thickness values less than 0.25 mm, but thicker silicon strips are required for interfacial toughness values of 200 J/m^2 and higher.

For the ENF specimen, for a given toughness G_c, the maximum load is given by

$$P = \frac{4b_{Si}}{3a}\sqrt{G_c E_{Si} h_{Si}^3} \tag{3.4}$$

and the corresponding displacement is

$$\delta = \left(2 + 3\left(\frac{2a}{L}\right)^3\right)\frac{PL^3}{8E_{Si}b_{Si}h_{Si}^3}\,. \tag{3.5}$$

The load-displacement responses for interfacial toughness values of 2, 20, and 200 J/m^2 are shown in Figure 3.4 for the same range of crack lengths and silicon thicknesses as before. For $G_c = 2$ J/m^2, for the thicknesses considered, the load levels range from 25 to 0.5 N. When the toughness values are increased to 20 and 200 J/m^2, the loads range from 80 to 1 N and 550 and 23 N, respectively. The maximum stress occurs at the top of the lower adherend at the mid span. It is given by

$$\sigma_{\max} = \frac{1}{2}\left(\frac{L}{a}\right)^2\sqrt{\frac{G_c E_{Si}}{h_{Si}}}\,. \tag{3.6}$$

The range of maximum stress levels is shown in Figure 3.5. For toughness values less than 20 J/m^2, the thickness of the silicon adherends should be greater than 0.3 mm to prevent failure in the silicon. For 200 J/m^2, the minimum thickness is about 3.2 mm.

For the MMF specimen, for a given toughness G_c, the maximum displacement is given by

$$\delta = \sqrt{\frac{16G_c L^2\left(3N-4L\right)^2 b_{Si}^2}{216E_{Si}I_{Si}^2}\left(\frac{h_{Si}^3\left(h_{Si}+h_{Si}\right)^3}{\left(h_{Si}+h_{Si}\right)^3 - h_{Si}^3}\right)} \tag{3.7}$$

and the corresponding maximum load is

$$P = \frac{6E_{Si}I_{Si}\delta}{L^2\left(3N-4L\right)}\ , \tag{3.8}$$

where E_{Si} is the Young's modulus of the carrier beam, L is the span of the constant moment section and N is the distance between the outer supports.

The load-displacement responses for interfacial toughness values of 2, 20, and 200 J/m^2 are shown in Figure 3.6 for the same range of silicon thicknesses as before. The energy release rate is independent of crack length as this specimen is assumed to be a steady state fracture specimen. . For $G_c = 2$ J/m^2, for the thicknesses considered, the load levels range from 16 to 2 N. When the toughness values are increased to 20 and 200 J/m^2, the loads range from 25 to 4 N and 180 and 30 N, respectively.

The maximum stress occurs at the top of the lower adherend at the mid span. It is given by

$$\sigma_{\max} = \frac{3PL(N-L)}{2b_{Si}h_{Si}^2}\ . \tag{3.9}$$

The range of maximum stress levels is shown in Figure 3.7. For toughness values of 2 J/m^2, the thickness of the silicon adherends does not play an important role. However, for 20 and 200 J/m^2, the minimum thickness is 0.1 and 1.2 mm, respectively. Although the device was effectively designed for all three configurations, the ELS specimen was chosen for the experiments because of its ability to provide a range of mode-mix values.

3.1.2 Loading Device

A schematic of the loading device is shown in Figure 3.8. The loading device consists of a linear actuator coupled with a load cell connected to a loading head. Experiments were conducted in two configurations. Initially, prior to the incorporation of the DIC technique, the specimen was clamped to the loading device as shown in Figure 3.8a (the clamps are not shown for the sake of clarity). The device and specimen were

subsequently modified in order to allow for the microscope to capture the side view of the specimen (Fig 3.8b) although the boundary conditions were preserved. The main modifications in the DIC specimen were the introduction of the aluminum base on which the specimen is mounted and the 45^{o} angle prism mirrors to direct the normal incident beam from the microscope to the side of the specimen. The loading device consists of a stepper motor (ZST6, Thor Labs Inc.), having a travel range of 6 mm and a load capacity of 32 N. The choice of this actuator was based on its ability to cover small distances (0.1 μm) over the entire travel range essentially providing a fine resolution coupled with flexible travel velocities as low as 0.1 μm/s. The linear actuator was then coupled to a subminiature load cell (Model 31, Honeywell Inc.) with a range of 9.8 N. The load cell was chosen based on the load levels expected from the design curves discussed in the previous section. The displacement of the linear actuator was controlled by a Thor Labs TST001 controller driven by a GUI program called APTUser interface. The response of the load cell was amplified using a Vishay® signal conditioning amplifier the data from which was obtained by a National Instruments® Data Acquisition (DAQ) system. The frame of the loading device was machined using Al-2024 procured from Trident Metals Inc.

Calibration

The load-displacement response of the ELS specimen was to be used in the fracture analysis of the data, based on the measured load and the actuator displacement, which relies on the device being sufficiently stiff. This was established with a cantilever beam consisting of a single strip of 585 μm-thick silicon with planar dimensions of 40×5 mm, which was clamped at one end and loaded at the other with the linear actuator attached to the load cell. In order to check for compliance issues, a miniature differential

variable reluctance transducer (DVRT) from Microstrain Sensing Systems Inc. was added to the setup in order to measure the beam displacement on the opposite surface to the one being contacted by the actuator. The DVRT has a 1.5 mm diameter stainless steel solenoid with a 0.5 mm super elastic NiTi alloy core with a stroke of 1.6 mm. The load cell and actuator were calibrated separately beforehand; the load cell calibration was -4.0667 N/V and the DVRT calibration was $163.8\,\mu$m/V .

The cantilever beam response is shown in two ways (Fig. 3.9); first the actuator displacement under load is compared with the displacement measured by the DVRT on the upper side of the beam. It can be seen (Fig. 3.9a) that there was indeed some compliance in the actuator/load train as the actual displacement was 84.5% of the value displayed by the actuator output. When this was accounted for, the load-displacement of the cantilever matched (Fig. 3.9b) the response from simple beam theory. This system calibration was then used in the fracture experiments where it was not possible to use the DVRT for IR-COI and the DVRT simultaneously.

3.2 EXPERIMENT

In the mixed-mode experiment, the measurements of crack opening displacements were made with IR-COI and DIC . As described in detail in the previous chapter, the former was used in order to obtain normal crack opening displacements over most of the crack front. However, information on the tangential component of the displacements was still lacking owing to the limitations of the interferometry approach. Both the normal and tangential displacements were measured using DIC by making minor modifications to the specimen and loading device.

3.2.1 Sample Preparation

Sample preparation for the ELS specimens followed a similar protocol to the one explained in Section 2.1.2. However, only the Huntsman epoxy was used for the ELS experiments. The specimen consists of two silicon strips bonded by a layer of epoxy. The n-type Si (111) wafers used here were polished on both sides to allow the use of IR-COI and were obtained from WRS Materials. The wafers were 125 mm in diameter and nominally 585 μm in thickness. An automatic dicer (Disco, model DAD 321) was used to cut the silicon wafers into two sets of dimensions. The bottom adherends for the IR-COI measurements were 40×15 mm strips whereas in the case of DIC, the bottom adherends were 40×5 mm strips. The top adherends in both cases were 50×5 mm strips. These were then cleaned individually by ultrasonication in de-ionized water to remove any particles that may have accumulated during dicing. The top adherend was coated with an Au/Pd thin film from one end of the strip to a length of 25 mm. Because of the low mode-I toughness of the Au/Pd coating ($\approx 0.07\ \mathrm{J/m^2}$), a wedge was initially inserted to introduce an initial crack with minimal or no damage ahead of the crack front.

To prepare the IR-COI test specimen, the wider silicon strip was laid on a Teflon® tape. In order to prevent epoxy from spreading out of the desired contact area,

the silicon strip was masked with Teflon tape leaving an area of 40×5mm in the center exposed. A bead of the degassed Huntsman epoxy was dropped on the exposed surface and spread out with a spatula. For specimens with epoxy layers of thicknesses greater than 20 μm, shims that were 25.4 μm and 38.5 μm thick were placed at the ends of the bottom adherend. For very thin layers of epoxy (<12 μm), a glass slide was used to remove excess epoxy from the exposed adherend leaving behind epoxy layers that were as thin as 4-5 μm. Then the top silicon adherend with the partial Au/Pd coating was pressed on the bead with a 138.26 g weight to mold the epoxy into a uniform layer between the two silicon strips. The specimen was cured for 3 hours at 65°C and then allowed to cool slowly.

The sample preparation for the DIC specimens followed the same procedure as the IR-COI test specimens except for the fact that the lower adherends in the DIC specimens were 40×5 mm. After the epoxy cures, the DIC specimens require a random pattern on the region of interest in order for the correlation software to be able to match subsets of the images. Furthermore, in order for 2D-DIC to be utilized, the area under consideration must be planar which dictates that the silicon adherends in the DIC specimens must be of the same width and should be properly aligned prior to the curing of the epoxy. Despite proper alignment, it is always possible for some spillover of the epoxy to occur either during application or curing. Hence, after curing, a razor blade was used to remove any excess epoxy from the sides of the specimen. The specimens were then subject to grinding with a high grit (>600) sandpaper on a polishing wheel. This generated a random pattern on the silicon and epoxy while ensuring that the specimen became planar. In order to mount the DIC specimen on to the loading device, it was initially bonded to an aluminum base of the same 40×5 mm area with a thickness of 4 mm. This base was designed to be screwed on to the loading device. Prior to mounting,

the surface of the aluminum base and the bottom face of the specimen were cleaned with ethanol. After the specimen and base had dried, a drop of fast curing cyanoacrylate based glue was dropped on the base and spread out with a glass slide to ensure a very thin layer. The specimen was then bonded to the aluminum base, making sure of proper alignment. The alignment was maintained by keeping steel blocks adjacent to the specimen. In order to prevent the steel alignment blocks from getting bonded, they were coated with a thin layer of mold release. Despite the fast curing nature of the glue, at least 6 hours of curing time is required to attain its full bonding strength. This assembly was then screwed on to the loading device.

3.2.3 Digital Image Correlation

Two dimensional digital image correlation (2D-DIC) is a non-intrusive full field measurement technique for measuring in-plane deformation. A speckle pattern or a random texture on the surface of the object is observed throughout the measurement period. By the use of advanced correlation algorithms the motion of the speckle pattern with respect to the reference image (usually an image of the undeformed specimen) is tracked. The displacement of the speckle pattern is then directly related to the surface deformations of the specimen. Extensive research by communities worldwide (Pan et al. 2009) and development in commercial algorithms and image acquisition systems have established 2D-DIC as a robust and accurate method of measuring surface deformations on a planar surface.

2D-DIC is a valid technique only when certain necessary assumptions hold true. It is assumed that while the measurements are being made, the surface being observed is planar and parallel to the image plane. Furthermore, it is assumed that the out-of-plane

deformations are minimal and their effect on the in-plane deformations are negligible (Chu et al. 1985).

The basic concept of DIC relies on the maximization of the correlation coefficient determined by observing two sub images (or two pixel intensity array subsets) from two corresponding images and extracting the deformation mapping function relating the images. Each and every point in any image has a specific signature affiliated to it. A generic image correlation algorithm works by searching for the point in the deformed image that will maximize the similarity or cross correlation with the point in the undeformed state. In reality however, this signature is not as unique to a point as it is to a subset of the image. Hence, by tracking this subset in the deformed image for the maximum similarity between the undeformed and deformed images, the deformation of the image can be measured.

The smaller the subset size, the higher the resolution of the measurements that can be obtained. The size of the subset however, is entirely based on its uniqueness, which is determined by the pattern on the surface of the specimen. The computation of displacements and strains in DIC are based on the theory of continuum mechanics which has been covered in many resources (Fung 1965, Chu et al. 1985). The basic set of equations that correspond to the deformations and strains is shown below. DIC uses the principle in continuum mechanics that states that differentially small line segments (say PQ as shown in Figure 3.9) with components dx, dy and dz will remain differentially small line segments P*Q* with components dx^*, dy^* and dz^* which correspond to the deformed lengths. The lengths of the vectors PQ and P*Q* can be given by

$$\begin{aligned} |PQ|^2 &= dx^2 + dy^2 + dz^2 \\ |P^*Q^*|^2 &= dx^{*2} + dy^{*2} + dz^{*2} \end{aligned} \tag{3.10}$$

With u, v and w the displacements in the x, y and z coordinate system, the deformed lengths can be related to the original components of the undeformed line segment by Eqn (3.11).

$$\begin{aligned} dx^* &\cong \left(1+\frac{\partial u}{\partial x}\right)dx+\frac{\partial u}{\partial y}dy+\frac{\partial u}{\partial z}dz \\ dy^* &\cong \frac{\partial v}{\partial x}dx+\left(1+\frac{\partial v}{\partial y}\right)dy+\frac{\partial v}{\partial z}dz \\ dz^* &\cong \frac{\partial w}{\partial z}dx+\frac{\partial w}{\partial y}dy+\left(1+\frac{\partial w}{\partial z}\right)dz \end{aligned} \tag{3.11}$$

In order to compute the strains in 2D-DIC, the digital image correlation algorithm uses the Eqn. (3.12).

$$\begin{aligned} \varepsilon_{xx} &\cong \frac{\partial u}{\partial x}+\frac{1}{2}\left[\left(\frac{\partial u}{\partial x}\right)^2+\left(\frac{\partial v}{\partial x}\right)^2\right] \\ \varepsilon_{xy} &\cong \frac{\partial v}{\partial y}+\frac{1}{2}\left[\left(\frac{\partial u}{\partial y}\right)^2+\left(\frac{\partial v}{\partial y}\right)^2\right] \\ \varepsilon_{xy} &\cong \frac{1}{2}\left[\frac{\partial u}{\partial y}+\frac{\partial v}{\partial x}+\left(\frac{\partial^2 u}{\partial x\partial y}\right)+\left(\frac{\partial^2 v}{\partial x\partial y}\right)\right] \end{aligned} \tag{3.12}$$

As per the main assumption of 2D-DIC, the effects of the out-of-plane displacements and their derivatives are neglected.

In order to obtain the best results from the application of DIC, the uniqueness of the signatures of every subset has to be provided. This is accomplished by generating a random pattern on the surface of the specimen. The main constraints for this random pattern are as follows:

1. Randomness: each and every subset must have a unique pattern. Patterns developed from a saw or milling often tend to leave some regularity on the surface. This causes difficulty in tracking the subsets. Processes such as

polishing on a wheel generally provide more randomness to the surface pattern.

2. Have high contrast: the digital image acquisition system used must be properly calibrated to provide an optimal balance of contrast and brightness. Furthermore, this calibration must be preserved for the entirety of the experiment as each and every measurement is made based on the first reference image.
3. Be isotropic: randomness can be achieved even by having anisotropy present in the pattern. Providing a randomness in both x and y directions is necessary for preserving the uniqueness of subsets.

The work by Lecompte et al. (Lecompte et al. 2007) describes the optimal speckle pattern for a surface as one having speckles with radii between 2-5 pixels. The finer the speckle pattern, the smaller the subset that can be used. Generating this fine random texture has been approached by many methods depending on the scale of the specimen. At macro-scales, spray painting of black against white has been the most common way to generate a random pattern in a quick and efficient manner. At smaller scales, where optical microscopes are used, the methods chosen to generate a random pattern varies from one material system to another. Sun et al. (Sun et al. 1997) demonstrated the application of two methods of generating random patterns suitable for high magnifications. In one case carbon particles were sputtered onto the surface of the specimen under vacuum. However they indicate that this method was not very efficient as the control of carbon particle size was difficult and resolving the pattern under an optical microscope proved impossible. The other more successful method described by the same group was application of a colloidal suspension of 5 μm Ti particles mixed with collodion (a polymer liquid) in a 2 % amyl acetate solution to the surface. On drying, the liquid

leaves behind a plastic film with a random pattern that stuck firmly to the surface and was flexible to deformation. At even smaller scales where the images were captured using a scanning electron microscope, (Scrivens et al. 2006) demonstrated that nano-scale remodeling of metallic thin films coated on the surface of a substrate and then transferred to the specimen produced a speckle pattern with speckle sizes as small as 50-500 nm. Furthermore, Chasiotis and Knauss (Chasiotis and Knauss 2002) demonstrated that the surface roughness measured by an atomic force microscope can be used as a speckle pattern equivalent by means of a micro-tensile test.

However, in the case of the mixed-mode experiment described here, as mentioned previously, it was determined that grinding the side of the specimen to be observed using a high grit (>600) sandpaper on a polishing wheel after preparing the specimen proved to be the optimal method of not only generating a random pattern but also ensuring that the side of the specimen is planar in the image plane.

3.2.4 Experimental Procedure

The conduct of the mixed-mode experiment can be divided into two sections. A set of inspections and measurements need to be made first, with small variations with respect to the systems employed for IR-COI and DIC. The major difference between the two configurations, however, arises during the image acquisition phase of the experiment.

Once the specimen was prepared, a series of preliminary steps had to be completed prior to testing. Before mounting the specimen on to the loading device (in the case of the IR-COI experiment) or on to the aluminum base (in the case of the DIC experiment), a micrometer screw gauge was used to record the thickness of the epoxy by measuring the total thickness of the specimen and subtracting out the thickness of the

silicon strips which were measured prior to specimen preparation. Furthermore, the side-view of the DIC specimens when observed under a microscope was used to measure the epoxy thickness and corroborate the screw gauge measurements.

Next, to provide an initial crack, the Au/Pd coated region of the specimen had to be delaminated. To accomplish this, a wedge of thickness 83.8 μm was inserted between the adherends. As mentioned in the mode-I experiment, the low toughness of the Au/Pd layer gave rise to its immediate delamination providing an initial crack at the silicon/epoxy interface with minimal or no damage ahead of the crack front. Another advantage of the Au/Pd layer was that the IR- optimized microscope could be used to clearly define the beginning of the silicon/epoxy interface (which is the undamaged crack front) as is shown in Figure 2.8. Once the Au/Pd layer was completely delaminated and its boundary (henceforth referred to as the gold line) was established, the specimen was ready for mounting on to the loading device or the aluminum base depending on the configuration to be employed.

The first step after mounting the specimen on to the device was to measure the initial crack length a_0, starting from the gold line to the point at which the actuator made contact with the top adherend. In order to accurately measure the initial crack length, it was necessary for the loading head of the actuator to be positioned extremely close to the top adherend. This positioning was achieved by initially moving the loading head of the actuator closer to the top adherend but making sure that no contact was made. Subsequently, to prevent the specimen from damage, small jogs of 0.05 mm were applied to the actuator through the APTUser interface program. Concurrently, the LabView program was launched in order to collect data from the load cell. The point at which the loading head makes contact with the specimen was indicated by a jump in the load value displayed by the real time load tracking plot in the program. The small jog displacements

prevent the load from reaching values that would damage the interface. Successive changes in the displacement of the actuator helped position the loading head at a distance of 0.1-0.5 μm to the top adherend. This positioning step ensures that the loading head was visible through the upper silicon adherend. The initial crack length a_0 was then measured by first acquiring images of the top view of the specimen from the gold line till the loading point. Next, by making use of natural markers on the silicon surface and using ImageJ software for image processing, the total distance between the two points could be measured. This concluded the initial steps required for the IR-COI based experiment.

The experiment with the DIC configuration required some additional steps. The correlation conducted on the images captured during the DIC experiments were analyzed by using the commercial image correlation software, ARAMIS® (version 6.3, GOM Corporation) which computed the displacements and the strains based on the concepts discussed in the previous section. However, in order for ARAMIS to be able to analyze the images, the compatibility of the pattern on the specimen with the software must be examined. This is achieved by initially capturing multiple images of a stationary specimen under the microscope and consequently analyzing these images through ARAMIS®. This provides two important results:

1. The effectiveness of the pattern. ARAMIS® provides a value called the residual when the images captured in the microscope are uploaded to the software and the pattern is checked. In order for the pattern to be effective and provide good resolution in the computation of the displacements and the strains, the value of the residual must be around 5.
2. The error involved in displacement and strain calculations. Ideally all the displacements and the strains computed must be zero. Figure 3.11 shows two images of a stationary specimen taken subsequently. ARAMIS® computes the

displacements and strains in the second image considering the first image (Fig 3.11a) to be the reference. As these images are taken of specimens that are stationary, any displacement or strain value computed is attributed to the error in the measurement and provides the minimum resolution of the DIC technique. The histogram provided in Figure 3.11b gives an estimate of the error to be ± 0.08 μm.

Secondly, the 45^o prism mirrors had to be fixed in a specific position in the grooves parallel to the specimen such that the side-view image corresponded to the location of the crack tip. Unlike the IR-COI case, where the crack front was readily visible through the microscope, the side-view of the specimen did not provide enough visibility to ascertain the crack tip location. To do this, the gold line was first brought into focus in the top view image of the specimen. Next, by translating the microscope stage in the direction towards the prism mirror using the gold line as the axis, the microscope was focused on the side-view of the specimen. The point at which the gold line axis intersected the silicon epoxy interface in the side-view image, determined the location of the crack tip (Fig 3.12).

The experiments were performed using an infrared microscope (Olympus BH2-UMA) that was fitted with an internal beam splitter and an IR filter ($\lambda = 1050 \pm 2$ nm) to provide the normal incident beam (Fig. 3.8). A digital camera (Lumenera Corporation, Infinity 3) with a resolution of 1392×1040 pixels captured the images (Fig. 3.12a)

Irrespective of the configuration the mixed-mode experiment was conducted in, the procedure of loading /unloading remained the same. The experiment was performed by applying a transverse load in displacement control via the linear actuator to the free end of the top silicon adherend. The APTUser interface was configured to apply

displacements at a rate of 0.1 μm/s. Data from the load cell was collected by the LabView program at a sample rate of 16 samples/s and displayed in a real-time load tracking plot. The image acquisition, controlled by the Infinity Analyze software (Lumenera Corporation), was executed in a time-lapse mode to capture images at an interval of every 5 seconds for the duration of the entire experiment. The experiment was conducted by triggering all the programs in order for them to be as synchronized as possible. Both loading and unloading of the specimen followed the same procedure.

Image Acquisition- IR-COI

The mixed-mode experiments conducted in the IR-COI configuration (Fig 3.8a) followed a similar procedure as described in section 2.1.4 with respect to image processing. However, the image acquisition process was considerably different from that of the mode-I experiment. As all the mixed-mode experiments were conducted on specimens with the silicon thickness being nominally 585 μm (as compared to the mode-I experiments which were conducted on silicon thicknesses of 280 μm), a longer central wavelength ($\lambda = 1050 \pm 2$ nm) of the IR band-pass filter was chosen in order to increase penetration of the light source into the silicon. This increase improved the clarity of the interference fringes, but decreased the resolution of the NCOD measurements by approximately 5 nm.

Unlike the mode-I experiment, all the images in the mixed-mode experiment were captured in the time-lapse mode. In the initial stages of loading, images were captured at a low magnification using a 5X objective. Furthermore, the microscope was positioned such that the bonded region ahead of the gold line occupied only a small area in the field of view ensuring that the images captured the appearance of the fringes as they started to move closer to the crack front. On image processing, this positioning proved to be

advantageous in observing the development of the NCOD during the crack opening phase.

As the experiment progressed, the fringes moved closer to the crack front. When the number of dark fringes in the field of view exceeded three and the gap between the first dark fringe and the crack front became narrower, the magnification of the microscope was increased by shifting to the 10X objective. Furthermore, the microscope was translated such that the crack front was now at the center of the field of view with at least one fringe present in the image. This was to ensure that crack nucleation and initial propagation phases were accurately captured during the experiment. Once the crack started to propagate, the microscope was translated in order to follow the new crack front. However, the original crack front remained visible. When the moving crack front approached the limit of the field of view, the 5X objective was again used to observe the moving crack front while maintaining visibility of the original crack front location and the associated crack opening displacements there.

When the crack growth reached a value of approximately 1-1.2 mm (800-900 pixels), the loading was stopped and unloading of the specimen was initiated. However, despite this, the crack usually continued to grow till the load dropped to a certain level. Hence, the moving crack front was continuously monitored by translating the microscope till the crack arrested.

The images captured were processed to determine the location of the crack front and the NCOD. Each transition from a dark to a bright fringe or vice-versa, corresponds to an increment in the NCOD by a quarter of the wavelength ($\lambda = 265\,\text{nm}$). However as mentioned previously in section 2.1.4, Eqn. (2.9) was applied, utilizing the measurement of intensities between the dark and bright fringes to measure NCOD even more accurately improving the resolution by almost an order of magnitude bringing the

resolution down to 20 nm. Subsequently, the image processing for the IR-COI based experiment followed a similar procedure as described in the mode-1 experiment.

An issue that was often encountered in the early stages of the experiment, was the healing of the Au/Pd layer following the initial wedge insertion and removal. Despite the Au/Pd layer being delaminated prior to the experiment, in most cases, it was observed that the layer healed to a certain extent. Due to this, the crack front was actually behind the gold line at the beginning of the experiment. As the loading progressed, however, this healed region was did delaminate, bringing the crack front into registration with the gold line. As will be seen later, this process could be also observed in the load-displacement response.

Image Acquisition- DIC

The experiments with the DIC configuration were performed with the same infrared microscope (Olympus BH2-UMA) with the internal beam splitter to provide the normal incident beam which was directed to the side of the specimen by the 45^{o} prism mirrors (Fig 3.8b). However, despite the roughening of the silicon surface at the polishing stage of specimen preparation, the side of the silicon reflected more light than the epoxy, preventing the camera from capturing all the features of the side-view of the specimen which decreased the effectiveness of the speckle pattern in the region of interest. Increasing the intensity of the light source in the microscope enhanced the reflection from the silicon adherends darkening the features of the epoxy which was undesirable. To resolve this problem, two Nikon MK-II fiber optic gooseneck lamps were utilized to provide focused illumination from either side of the prism mirror. The location and angle

of the gooseneck lamps could be modified in order to obtain an optimal image (Fig. 3.12b) that clearly displayed the speckle pattern on both the silicon and the epoxy.

Since the DIC technique worked by comparing subsequent images with the first image as the reference, all the images in an experiment were taken under identical settings. In all experiments, the images were captured by the camera with the 10X objective. Once the experiment commenced, there was absolutely no translation of the microscope. Due to the nature of the DIC configuration, the indication of crack growth was obtained by closely monitoring the real time load displayed on LabView. A considerable change in the slope of the load displayed signified the onset of crack growth. In many cases, the load value plateaued indicating steady state crack growth. At this point, the specimen was unloaded following the same procedure.

The image processing of the DIC images was conducted by utilizing the commercial software ARAMIS®. Processing images in ARAMIS® could be achieved by two methods. The entire experiment could be conducted with the ARAMIS® software controlling the camera, capturing the images and then processing them. However, in the DIC experiment conducted in this study, the images were acquired separately using the Infinity Analyze software and camera as mentioned, and then uploaded separately into ARAMIS® for processing. On uploading the images, two factors need to defined for ARAMIS® to compute the displacements and strains.

1. Project parameter: In all images, the project parameter was a rectangle that defined the region of interest which needed to be processed. Figure 3.13 shows an overlay of the project parameter on the original image. Furthermore, the facet (or sub-image) size and the facet step (distance between two sub-images) need to be defined at this point. Depending on the speckle pattern on the specimen, the facet size for the DIC images was defined between 10-15

pixels and the facet step was defined as 8-13 pixels. Each calculated facet became a data point and a smaller facet step led to more calculation of data points.

2. Start point. In order for the program to start displacement calculations, a starting facet had to be defined. This instructs the program to start calculations from that specific facet. The choice of the location of the start point must be a region where minimum deformation has occurred. The presence of cracks could obscure the starting facet and end the calculation prematurely. It was thus preferable to define multiple start points and choose the start point locations in the silicon surface of the project parameter.

Defining these two parameters for all the images to be processed allowed ARAMIS® to compute the displacements and the strains which were displayed once the calculation was completed. In order to obtain the actual displacement corresponding to the scale of the experiment, the calibration factor of the microscope defining the distance to pixel ratio for the 10X objective had to be incorporated into ARAMIS®. This was done by choosing an option known as the 2D Parameter where the distance per pixel ratio could be entered.

Unlike the IR-COI case, obtaining the NCOD profiles or tracking the crack growth using DIC is non-trivial. However, the crack tip opening displacements (CTOD) at the gold line could be obtained with relative ease.

3.2.5 Measurements

In both configurations of the mixed-mode experiment, the global measurements were extracted in an identical manner. The displacement applied at the end of the top adherend and the corresponding load were extracted by utilizing their respective

calibration factors determined previously (Section 3.1.2). A typical load-displacement response of the mixed-mode experiment is shown in Figure 3.14. An examination of the response at the early stages of the experiment (i.e. at very small displacements) showed a large initial stiffness till the load reached a value of about 0.2 N. This initial stiffness was attributed to growth of the healed crack. Beyond this load, the stiffness was seen to decrease to a lower value and remain constant till the onset of crack growth. Crack growth was indicated by a gradual stiffness decrease in the load-displacement response. As the crack growth reached a steady state, the load value displayed a tendency to plateau. Once this plateau was observed, the unloading process was initiated. Despite the initiation of the unloading process, the crack was observed to continue growing, thereby eliciting non-linear behavior in the unloading response. Below a certain load level, however, the unloading response followed a linear path back to zero which indicated that the crack had arrested. The local measurements were dependent on the configuration in which the mixed-mode experiment was conducted. Figure 3.15 sketches the crack tip region and the cohesive zone, defining the coordinate systems used in the mixed-mode experiment for the local measurements. The origin $x = 0$ is the location of the initial crack front, and $r = 0$ defines the moving crack front. The COD at the initial crack front ($x = 0$) is denoted δ_v^* A cohesive zone ahead of the crack front (x > 0) is indicated by the interfacial tractions acting to resist the opening of the interface

IR-COI Measurements

The IR-COI technique was applied to make two local measurements: tracking the crack growth as a function of the applied displacement and measuring the NCOD as a function of distance from the crack front as the loading progressed.

After the initial measurement of the crack length from the loading point to the gold line, the crack growth is tracked by measuring the distance between the crack front and the gold line (Fig 3.16). Initially, when the crack front was coincident with the gold line, the crack length remained constant as a function of applied displacement. As the crack began to grow, the dependence of the crack length on the applied displacement started to increase. At the onset of steady state growth, the crack length increased drastically with respect to the applied displacement.

A typical set of NCOD profiles measured during crack opening and growth is displayed in Figure 3.17. Initially the first few NCOD profiles corresponded to the delamination of the healed region till the crack front became coincident with the gold line. Subsequently, it was observed that the crack front first remained stationary as the crack faces separated further. Once the crack front began to move forward, the NCOD profiles seemed to retain their shapes, which was an indication of steady state. Furthermore, by obtaining NCOD values at $x = 0$, the normal CTOD values were obtained as a function of the applied displacement (Fig. 3.18). The dependence of the CTOD values on the applied displacement seemed to display two major trends. Initially, the CTOD values exhibited a gradual increase till the point at which the crack growth reached a steady state. At the onset of steady state crack growth, the CTOD values increased much more rapidly, indicating that the interface has fully damaged.

DIC Measurements

The DIC technique does not possess the resolution to make measurements of crack length. However, based on the load-displacement response, the crack length could be calculated from the beam on elastic foundation theory. This analysis is discussed in detail in Section 3.3

However, the DIC technique had the ability to compute displacements at every point in a defined project parameter. This was applied to make local measurements of the CTOD at the specimen edge in both normal and tangential directions. This was accomplished by a feature in ARAMIS® known as a stage point. By creating a stage point at a particular location inside the project parameter (i.e. the region of interest), it was possible to obtain any displacement or strain information computed for that point. Hence, by choosing stage points above and below the initial crack tip location, it was possible to obtain the CTOD values as a function of the applied displacement. Figure 3.19 displays the normal and tangential CTOD values $\left(\delta_n^* \text{ and } \delta_t^*\right)$ measured as a function of applied displacement for a typical mixed-mode experiment conducted in the DIC configuration. As can be observed, both the CTOD responses exhibit two distinct trends as the load is applied. Initially both the CTOD values seem to increase slowly with respect to the applied displacement. However, at the onset of steady state crack growth, the CTOD values increase with a much higher dependence on the applied displacement.

3.3 ANALYSIS

Several approaches have been developed in order to extract the mode-I traction separation relations. However, studies focusing on the extraction of mixed-mode traction-separation relations are relatively limited. Even then, the majority of the approaches proposed for the extraction of mixed-mode traction-separation relations have been based on iterative methods. One approach suggested has been to extract pure mode-I and pure mode-II traction-separation relations experimentally and then conduct an iterative study by varying the parameters of a pre-selected traction-separation relation to match the experiment results (Yang and Thouless 2001, Li et al. 2006) at other mode-mixes. Another approach has been to locally measure the displacement field around the crack tip for a variety of mode-mix values and then match these measurements to the displacement field generated by a cohesive zone model (Mohammed and Liechti 2000). The parameters of the cohesive zone model yielded the components of the mixed-mode traction-separation relation. Hybrid techniques involving potential based cohesive zone models have been demonstrated by groups previously (Gain et al. 2011, Shen and Paulino 2011). Introduced by Needleman (Needleman 1987), and recently reviewed in detail (Park and Paulino 2011), potential based models have generated interest because of their ability to generalize the traction-separation relation for a specific interface under any mode-mix. These models are based on a potential function of a specific form (polynomial, exponential etc.) the derivative of which, provides the traction-separation relationship. .Direct methods to extract traction-separation relations have been fairly scarce. However, Sørensen and Kirkegaard (Sørensen and Kirkegaard 2006) proposed a direct approach where simultaneous measurements of the J-integral, δ_n^* and δ_t^* can be used to derive the mixed-mode traction-separation relation. This approach was further examined by experiments (Högberg et al. 2007).

In the method developed in this work, a similar approach was used based on the J-integral along with the incorporation of a damage model for relating the tractions with the displacements. Furthermore, the mode-mix values were experimentally determined by using the DIC technique. The path independence of the J-integral allowed the global and local parameters measured to be related. This was already demonstrated in the mode-I experiment by equating the J-integral value calculated with the measured crack length to the local J-integral value defined around the crack tip (Sørensen and Jacobsen 2003, Zhu et al. 2009, Gowrishankar et al. 2012).

3.3.1 J-integral formulation

Based on the loading and geometry, the ELS specimen can be considered as a single cantilever beam for the purpose of J-integral calculations. Furthermore, it was observed from the load-displacement response (Fig 3.14), that the beam on elastic foundation model exhibited a better match to the experimental measurements than the simple beam theory. Hence, the J-integral formulation was based on the analytical approaches described in section 2.2 where the elastic foundation effect is incorporated into the simple J-integral equation. The important equations describing the J-integral formulation are given here. A detailed analysis is provided in the doctoral work of Mei (Mei 2011) and in the appendix section of the publication based on Chapter 2 (Gowrishankar et al. 2012).

The load displacement response for the beam on elastic foundation was defined by the equation

$$P = \frac{3E_{Si}I_{Si}\Delta}{a^3}\left(1+\frac{3}{\lambda a}+\frac{3}{(\lambda a)^2}+\frac{3}{2(\lambda a)^3}\right)^{-1}, \tag{3.13}$$

where $\lambda = \left(\frac{6K_0}{E_{Si} h_{Si}^3} \right)^{\frac{1}{4}}$ and $K_0 = \frac{2E_e}{h_e}$. Here, a is the crack length, E_{Si} and E_e are the Young's modulus values of silicon and epoxy respectively. P and Δ represent the load and displacement while h_{Si} and h_e correspond to the thicknesses of silicon and epoxy, respectively. Based on this relationship and the analysis explained previously, the J-integral could be calculated by the following equations (Eqs.(3.14), (3.15) and (3.17)) based on the measurements available.

$$J(\Delta, a) = \frac{3E_{Si} h_{Si}^3 \Delta^2}{8a^4} \left(\frac{1 + \frac{1}{\lambda a}}{1 + \frac{3}{\lambda a} + \frac{3}{(\lambda a)^2} + \frac{3}{2(\lambda a)^3}} \right)^2 \tag{3.14}$$

$$J(P, a) = \frac{6(Pa)^2}{E_{Si} b_{Si}^2 h_{Si}^3} \left(1 + \frac{1}{\lambda a} \right)^2 \tag{3.15}$$

However, in the case of the DIC experiment, measurements of crack length are unavailable. In order to calculate the crack length based on the beam on elastic foundation approach, the Equation (3.13) was solved for a. This provided an effective crack length a_{eff},

$$a_{eff} = \frac{1}{\lambda} \left[\left(3E_{Si} I_{Si} \left(\frac{\Delta}{P} \right) \lambda^3 - \frac{1}{2} \right)^{\frac{1}{3}} - 1 \right] \tag{3.16}$$

that could be obtained from the compliance of the load-displacement response.

The accuracy of this calculated crack length was evaluated by comparing the computed a_{eff} value with the measured crack length of an IR-COI based experiment when plotted with respect to applied displacement. Figure 3.16 shows good agreement between the a_{eff} value and the measured crack length. To calculate the J-integral for the DIC experiments, this a_{eff} value was substituted into Equation (3.15) to provide a J-integral formulation based on load and displacement.

$$J\left(P,\Delta\right)=\frac{6P^2}{E_{Si}b_{Si}^2h_{Si}^3}\left(\frac{E_{Si}b_{Si}h_{Si}^3\lambda^3}{4}\left(\frac{\Delta}{P}\right)-\frac{1}{2}\right)^{\frac{2}{3}} \tag{3.17}$$

The comparison of the three J-integral formulations with respect to crack growth in an IR-COI experiment is shown in Figure 3.20. It can be seen that the error between them is less than 2.2%. However, for the sake of consistency, Equation (3.17) was used for calculating the J-integral in all the experiments.

The local J-integral when a contour integral enclosing the cohesive zone is evaluated (Sørensen and Kirkegaard 2006, Högberg et al. 2007) is

$$J\left(\delta_n^*,\delta_t^*\right)=\int_0^{\delta_n^*}\sigma(\delta_n,\delta_t)d\delta_n+\int_0^{\delta_t^*}\tau(\delta_n,\delta_t)d\delta_t \ , \tag{3.18}$$

where the tractions $\sigma\left(\delta_n,\delta_t\right)$ and $\tau\left(\delta_n,\delta_t\right)$ act across the interface over the cohesive zone.

Furthermore the path independence of the J-integral can be utilized to equate Eqn. (3.18) to Eqn. (3.17). Previously in the mode-I experiment, the absence of the shear component in the local J-integral formulation simplified the extraction of the traction-separation relation as the J-integral calculated by crack length measurements was able to be differentiated with respect to the normal CTOD. In the mixed-mode experiment, however, the presence of the shear component makes this process a little more complicated and requires a measure of mode-mix to be defined.

3.3.2 Defining Mode-Mix

Extracting mixed-mode traction-separation relations requires the mode-mix to be known. However, it turns out that there are a number of definitions of mode-mix, which are not necessarily consistent. These are reviewed here. Depending on whether the approach is from a LEFM perspective or a CZM perspective, the basic motivation behind

a mode-mix definition has been to quantify the proportion of the shear interactions to the normal interactions.

For homogeneous, isotropic and linearly elastic solids, LEFM defines the mode-mix as

$$\psi_H = \tan^{-1}\left(\frac{K_{II}}{K_I}\right) \tag{3.19}$$

where K_I and K_{II} are the normal and shear stress intensity factors. However, interface cracks demand a more complex definition of mode-mix due to the oscillating singularity. In order to understand the definition of mode-mix in an interface from an LEFM perspective, two constants (α and β) known as the Dundurs parameters (Dundurs 1969) need to be defined. These parameters correspond to the elastic and bulk modulus mismatch between the two materials forming the interface. Assuming E , μ and ν to be the elastic tensile modulus, the shear modulus and the Poisson's ratio of materials 1 and 2 (Fig 3.21) , the Dundurs parameters (Dundurs 1969) can be defined by

$$\alpha = \left(\frac{\overline{E}_1 - \overline{E}_2}{\overline{E}_1 + \overline{E}_2}\right)$$

and , (3.20)

$$\beta = \frac{1}{2}\frac{\mu_1(1-2\nu_2) - \mu_2(1-2\nu_1)}{\mu_1(1-\nu_2) + \mu_2(1-\nu_1)}$$

where $\overline{E_i} = E_i/\left(1-\nu_i^2\right)$ in plane strain and $\overline{E_i} = E_i$ in plane stress.

Furthermore, the stress intensity factors at an interface are defined by the complex stress intensity factor $K = K_1 + iK_2$ where K_1 and K_2 cannot be decoupled into the local mode-I and mode-II stress intensity factors when the materials forming the interface are dissimilar $\beta \neq 0$.

The mode-mix for interface cracks (Rice 1988) has been defined as

$$\psi_K = \tan^{-1}\left(\frac{\mathrm{Im}\left[Kl^{i\varepsilon}\right]}{\mathrm{Re}\left[Kl^{i\varepsilon}\right]}\right), \tag{3.21}$$

where $\varepsilon = \frac{1}{2\pi}\ln\left(\frac{1-\beta}{1+\beta}\right)$ and l is an arbitrary length scale.

The reason for the appearance this length scale is that the proportion of mode-II to the proportion of mode-I in the vicinity of an interfacial crack tip varies with distance to the crack tip when $\beta \neq 0$. For a specific choice of l in the field of K-dominance, Eqn. (3.21) is equivalent to

$$\psi_K = \tan^{-1}\left[\left(\frac{\sigma_{12}}{\sigma_{22}}\right)_{r=l}\right] \tag{3.22}$$

The choice of l is generally based on either an in-plane length of the specimen geometry (such as the thickness of the epoxy layer in the case of the experiments conducted here) or on a material length scale (such as a fracture process zone size or a plastic zone size near the crack tip)

However, using the definition of mode-mix based on the interfacial stress intensity factors from LEFM in the extraction of a traction-separation relation for a cohesive zone model is not recommended as the definitions of tractions/stresses near the crack tip are different.

A definition of the mode-mix which connects the concepts of LEFM and cohesive zone modeling was provided by Parmigiani and Thouless where the energy density of the interface was partitioned into normal and shear components (Parmigiani and Thouless 2007).

$$\psi_G = \tan^{-1}\left(\sqrt{\frac{G_2}{G_1}}\right) \tag{3.23}$$

The G_1 and G_2 components are obtained by computing the area under the normal traction-separation relation and the tangential traction-separation relation. However, this

approach requires prior knowledge of the traction-separation relation. Note that this relationship can be obtained for $\beta = 0$ in the LEFM case where it is possible to decouple the mode-I and mode-II energy release rates. Otherwise the components of the energy release rate oscillate as the crack tip is approached (Chai and Liechti 1991).

A definition of mode-mix that can be obtained directly by measurements is by comparing the normal and tangential crack tip opening displacements (CTOD). This approach has been followed by groups in the past where the CTOD values were able to be experimentally determined (Mohammed and Liechti 2000, Sørensen and Kirkegaard 2006). In this definition, the mode-mix is defined as

$$\psi_{\delta} = \tan^{-1}\left(\frac{\delta_t^*}{\delta_n^*}\right) \tag{3.24}$$

In the case of the experiments conducted in this work, the DIC technique was exploited to measure the normal and tangential CTOD values for all experiments. Figure 3.19 shows the measurement of normal and tangential CTOD values by the DIC technique with respect to the applied displacement. It could be observed that the development of the CTOD with respect to the loading followed two distinct linear trends based on the state of the crack growth. Initially from applied displacement values from 0.15 mm to 0.3 mm, both normal and tangential CTOD displayed a slow growth that corresponded to the development of the cohesive zone. However, at an applied displacement value of about 0.3, both the CTOD values began to increase drastically; an indication that the crack had propagated along with the cohesive zone and there were no tractions holding the crack faces together anymore. Hence, in order to obtain the mode-mix at the crack tip, linear fits were applied to the initial growth of the CTOD. Applying the chain rule, the ratio between the slopes of these fits were used to compute the mode-mix. By obtaining the mode-mix values for specimens of different epoxy thicknesses, a

relationship was extracted between the mode-mix and the thickness of the epoxy. Moreover, this relationship was extended to obtain the mode-mix values of the IR-COI specimens as well. As the CTOD value provides the opening displacement along the cohesive zone, this definition of local mode-mix appears to be more pertinent in the extraction of traction-separation relations than the definitions based on LEFM concepts. The CTOD measure of mode-mix will be compared to the energy based one (Parmigiani and Thouless 2007) in the discussion section, once traction-separation relations have been extracted.

Figure 3.22 shows the dependence of mode-mix on the thickness of the epoxy in the ELS specimens considered here. For comparison, LEFM models were constructed of specimens with different epoxy thicknesses in ABAQUS to obtain the K_1 and K_2 values. The length scale for obtaining the mode-mix was chosen to be the thickness of the epoxy. This provided the mode-mix for the experiment based on LEFM. It can be seen that the two definitions of mode-mix differ in such a way that no length scale adjustment would bring them into registration. In view of the fact that the definition based on cohesive zone modeling does not suffer from issues related to the oscillating singularities all subsequent references to the mode-mix will be based on the CTOD.

3.3.3 Extraction of Mixed-Mode Traction-Separation Relations

The J-integral equation obtained by taking the contour around the crack tip (Eqn. (3.18)) can be differentiated to yield

$$dJ = \sigma d\delta_n^* + \tau d\delta_t^* \tag{3.25}$$

Dividing by $d\delta_n^*$ and invoking the mode-mix definition based on Eqn. (3.24) gives.

$$\frac{dJ}{d\delta_n^*} = \sigma + \tau \tan\psi_\delta \tag{3.26}$$

A similar result could be obtained by dividing by δ_t^*, but it is not independent of (3.26) and therefore does not provide any additional information. Such information needs to be introduced in order to extract the two individual traction separation relations $\sigma(\delta_n, \delta_t)$ and $\tau(\delta_n, \delta_t)$. This relationship was provided by using a damage model to define the traction-separation relations.

$$\begin{aligned} &\sigma(\delta_n, \delta_t) = (1-D)K_n\delta_n \\ &\text{and} \\ &\tau(\delta_n, \delta_t) = (1-D)K_t\delta_t \end{aligned} \quad , \tag{3.27}$$

where K_n and K_t were the stiffness values of the initial elastic region of the traction-separation relation and $D = f(\delta_n, \delta_t)$ was the damage parameter which defined the evolution of damage once the peak traction value was attained. Furthermore, this damage parameter function was assumed to be the same for both normal and shear traction-separation relations. By dividing the shear traction by the normal traction and applying the mode-mix definition based on CTOD, the relationship between the tractions was

$$\frac{\tau}{\sigma} = \frac{K_t}{K_n}\tan\psi_\delta \ . \tag{3.28}$$

Substituting Eqn. (3.28) in Eqn. (3.26) and rearranging, the normal component of the traction separation relation could be obtained from

$$\sigma(\delta_n^*, \psi_\delta) = \left(\frac{\partial J}{\partial \delta_n^*}\right)_{\psi_\delta} \left(1 + \frac{K_t}{K_n}\tan^2\psi_\delta\right)^{-1} \ . \tag{3.29}$$

Inserting the extracted normal tractions (Eqn. (3.29)) back into Eqn. (3.28) yielded the shear tractions.

A common way of representing the traction for each mode-mix is by combining the normal and shear traction as a vectorial traction

$$\sigma_v^2 = \sqrt{\sigma^2 + \tau^2} \quad . \tag{3.30}$$

Similarly, it is common to represent the crack tip opening displacements in terms of a vectorial CTOD

$$\delta_v = \sqrt{\delta_n^2 + \delta_t^2} \tag{3.31}$$

The process just outlined allowed the extraction of the traction-separation relations for both the DIC and IR-COI based experiments. However, it does depend on knowing the stiffness ratio K_t / K_n. One way of approximating the stiffness ratio is to assume that it is the ratio of the shear and Young's moduli of the epoxy.

$$\frac{K_t}{K_n} \approx \frac{\mu_e}{E_e} = \frac{1}{2(1+\upsilon_e)} = 0.369 \quad . \tag{3.32}$$

As will be seen later, another approach was to select an optimum value based on the toughness as a function of mode-mix

Toughness Prediction Model

In order to be able to predict the toughness Γ of the silicon/epoxy interface at any mode-mix, an analytical model was developed from Eqn. (3.18) by replacing the upper limits of the integral with, δ_{nc} and δ_{tc}, the critical end opening displacements of the traction separation relation so that

$$\Gamma = \int_0^{\delta_{nc}} \sigma d\delta_n + \int_0^{\delta_{tc}} \tau d\delta_t = G_{Ic} + G_{IIc} \tag{3.33}$$

where G_{Ic} and G_{IIc} are the mode-I and mode-II contributions to the toughness. This equation can be rewritten in terms of the stiffness values and critical displacements by substituting the tractions with the damage parameter relations defined in Eqn. (3.27), yielding

$$\Gamma = \frac{1}{2} K_n \delta_{n0}^2 + \int_{\delta_{n0}}^{\delta_{nc}} (1-D) K_n \delta_n d\delta_n + \frac{1}{2} K_t \delta_{t0}^2 + \int_{\delta_{t0}}^{\delta_{tc}} (1-D) K_t \delta_t d\delta_t \quad , \tag{3.34}$$

where δ_{n0} and δ_{t0} correspond to the normal and tangential opening displacements at the respective peak traction values. In order to solve the integral, the damage evolution function was assumed to be dependent only on the normal displacements. Thus

$$D = f\left(\delta_n\right), \tag{3.35}$$

This implies that the normal tractions are mode-independent as they are dependent only on the normal displacements from Eqn.(3.27). Furthermore, the mode-I component of the toughness becomes equal to the mode-I toughness $G_{Ic} = \Gamma_I$ Moreover the toughness could be obtained for as a function of the mode-mix normalizing with the mode-I toughness (Eqn. (3.33)). This provided a relationship of the toughness with respect to mode-mix that solely depended on the stiffness ratio

$$\frac{\Gamma}{\Gamma_I} = 1 + \frac{K_t}{K_n}\tan^2\psi_\delta \tag{3.36}$$

By fitting this model to the normalized toughness measurements that were made at different mode-mix values, the toughness could be predicted for the whole range of mode-mixes. Furthermore, as will be seen, an optimal stiffness ratio could be obtained to calculate the traction-separation relations for all experiments.

3.4 FINITE ELEMENT MODELING: MIXED-MODE EXPERIMENT

In order to apply the results obtained from the analysis developed, a finite element model was built in ABAQUS for the ELS mixed-mode experiment. The model was a two dimensional, tri-layer finite element model was constructed in ABAQUS, with a layer of cohesive elements (COH2D4) for the interface between the top silicon beam and the epoxy layer. Both silicon beams and the epoxy layer were modeled by plane-strain quadrilateral elements (CPE8R), with linear elastic properties (Young's modulus: $E_{Si} = 168$ GPa and $E_e = 1.85$ GPa; Poisson's ratio: $\nu_{Si} = 0.22$ and $\nu_e = 0.355$). The cohesive layer is defined by the traction separation relation which is extracted based on the analysis shown in the previous section. The results of this analysis are shown in the next section. Similar to the mode-I experiment, the traction-separation relation input into ABAQUS comprises of an elastic region and a softening region. The elastic region is defined in terms of a normal stiffness and a shear stiffness K_n and K_t till damage initiation occurs. In ABAQUS, the input parameters of the softening region are divided into three sections: damage initiation, damage evolution and the mixed-mode behavior. Damage initiation for the mixed-mode experiment is defined in terms of a quadratic stress criterion defined by

$$\left(\frac{\sigma}{\sigma_0}\right)^2 + \left(\frac{\tau}{\tau_0}\right)^2 = 1 \tag{3.37}$$

where σ_0 and τ_0 are the maximum normal and shear strength values for the entire range of mode-mix values. σ and τ represent the normal and shear strength values reached by the interface for a specific mode-mix. As the loading progresses, the normal and shear tractions increase linearly with respect to the corresponding separations with stiffness values of K_n and K_t respectively till the damage initiation criterioin is satisfied. The definition for damage evolution or the softening part of the traction-separation relation

varies in ABAQUS based on whether the damage defining parameter is the critical effective displacement $\left(\delta_{vc}-\delta_{v0}\right)$ (where δ_{vc} is the critical vectorial displacement and δ_{v0} is the vectorial displacement at peak traction) or the fracture energy, Γ_m. Based on the experiments, it was observed that the δ_{nc} values obtained were relatively independent of mode-mix. This was used to define the critical vectorial displacement as a function of the normal critical displacement and the mode-mix (Eqn. (3.38))

$$\delta_{vc}=\delta_{nc}\sqrt{1+\tan^2\psi_\delta} \tag{3.38}$$

The vectorial displacement at peak traction was defined in a similar manner in terms of the normal displacement at peak normal traction and mode-mix by

$$\delta_{v0}=\delta_{n0}\sqrt{\frac{1+\tan^2\psi_\delta}{1+\left(\frac{K_t\sigma_0}{K_n\tau_0}\right)^2\tan^2\psi_\delta}} \tag{3.39}$$

However, the mode-mix definition in ABAQUS is different as it is based on energy. Specifically, it is defined as the ratio of the mode-II component of the fracture energy to the total fracture energy. The mode-mix defined as a function of critical displacements can be related to the ABAQUS mode-mix by using the relationship developed in the toughness prediction model (Eqn. (3.36)).

$$\tan^2\psi_\delta=\frac{K_n}{K_t}\frac{\psi_{Ga}}{1-\psi_{Ga}} \tag{3.40}$$

where $\psi_{Ga}=\frac{G_2}{\Gamma_m}=1-\frac{G_1}{\Gamma_m}$.

The vectorial displacements can now be rewritten in terms of the ABAQUS mode-mix as shown.

$$\delta_{vc} = \delta_{nc}\sqrt{1+\frac{K_n}{K_t}\frac{\psi_G}{1-\psi_G}}$$
$$\delta_{v0} = \delta_{n0}\sqrt{\frac{1+\frac{K_n}{K_t}\frac{\psi_G}{1-\psi_G}}{1+\frac{K_t}{K_n}\left(\frac{\sigma_0}{\tau_0}\right)^2\frac{\psi_G}{1-\psi_G}}} \tag{3.41}$$

Similar to what was described previously in Chapter 2, the softening can be defined in terms of linear damage or exponential damage. As discussed before, if exponential damage is chosen, a shape factor α must also be provided. However, in ABAQUS, depending on the driving parameter (critical displacement or fracture energy) and the softening behavior, the mixed-mode behavior that can be input varies. With the critical displacement as the driving parameter and exponential softening, the mixed-mode behavior needs to be input as a table of values containing the critical effective displacement and the shape factor as a function of the mode-mix defined in ABAQUS.

The mixed-mode behavior in the traction-separation relation can be defined in multiple ways depending on the damage defining parameter. When energy is chosen as the driving parameter with exponential softening, the mixed-mode behavior can be defined in terms of tabular values or a power law criterion (Mei et al. 2010). The actual input fed into the simulation is discussed in the next section after obtaining the experimentally obtained traction-separation relations.

3.5 RESULTS AND DISCUSSION

By applying the analysis discussed previously, the extraction of the mixed-mode traction-separation relations of the silicon/epoxy interface was accomplished via a direct experimental approach. Because the formulation of the epoxy changed when this portion of the work was initiated, mode-I experiments with the silicon/Huntsman epoxy interface had to be repeated in order to be able to compare the interfacial properties extracted from the mixed-mode experiments to the nominal mode-I properties of the interface.

3.5.1 Mode-I Results

As the experimental procedure and the process of extracting mode I traction-separation relations were described in Chapter 2, only the results have been provided here. At each loading step, the J-integral was calculated using the measured crack length and linked with the measured NCOD. In particular, the NCOD at the initial crack tip $(x=0)$ was denoted as δ_n^*. As a result, the J-integral was obtained as a function of δ_n^* as shown in Figure 3.23. The overall behavior of the silicon/Huntsman epoxy interface was very similar to that of the silicon/CIBA-Geigy epoxy interface (Fig. 2.21). The Huntsman epoxy specimen shown here, rose to a value of 1.9 J/m^2 before settling at a steady state value of 1.76 J/m^2 compared to the steady state toughness of the silicon/CIBA-Geigy epoxy interface which reached 1.88 J/m^2. Furthermore, the stick-slip behavior exhibited by Huntsman epoxy specimen was far less significant compared to that observed in Figure 2.21. Following the same procedure as before, a polynomial function was used to fit the rising portion of the data in Figure 3.23

Utilizing Eqn. (2.23), the derivative of the fit was taken to obtain the mode I traction-separation relation for the silicon/Huntsman epoxy interface (Fig. 3.24). However, initial portions of the traction-separation relations obtained for the two interfaces by the direct methods were different. In order to maintain consistency, the

same stiffness value ($K_n = 2 \times 10^{15}$ N/m^3) continued to be used. The intersection of the elastic region of the traction-separation relation ($K_n \delta_n$) with the derivative of the fit defined the peak strength of the interface. Hence, the traction-separation relation of the silicon/Huntsman epoxy interface obtained via the direct method rose steeply to a strength of 33 MPa (as compared to the 22 MPa reached by the CIBA/Geigy epoxy). The softening that follows was relatively sharper and terminated at the critical value of the NCOD, δ_{nc} ~ 0.12 μm. The area underneath the curve provided a consistent value of the interfacial toughness, $\Gamma = 1.76$ J/m^2.

3.5.2 Mixed-Mode Experiment Results

Following the analytical procedure developed in section 3.3, the extraction of the traction-separation relations for the specimens in either configuration (DIC or IR-COI) was conducted in three main stages. Initially, the J-integral was calculated by using the measurements made for each specimen. Next, the toughness dependence on mode-mix was explored in order to estimate the stiffness ratio. Finally the traction-separation relations were obtained by adopting the procedure defined in the analytical section.

The first step in extracting the traction-separation relations was the determination of the J-integral value which in turn, provided the toughness of the interface when the crack growth reached a steady state. Based on the measurements of load and displacement, the J-integral value was obtained using Eqn. (3.17). Furthermore, depending on the configuration the mixed-mode experiment was conducted in, the fracture resistance curves were obtained by using the measured crack length (for IR-COI) or by calculating the effective crack length (for DIC) using Eqn. (3.16).

Figure 3.25 shows typical fracture resistance curves obtained by plotting the J-integral values against the crack growth. The IR-COI data (Fig. 3.25a) used the J-integral

values with the corresponding measured crack growth values to obtain the resistance curve. On the other hand, the plot from DIC data (Fig. 3.25b) was based on the effective crack length calculated using Eqn. (3.16) . The initial crack length a_0 in both cases, however, was measured by the IR-COI technique.

Though the resistance curves were from different specimens and mode-mix values, they displayed similar characteristics. The IR-COI data for this particular specimen, showed that the crack growth began when the J-integral reached a value of 3.5 J/m^2. As the experiment progressed, the crack growth rate began to increase compared to the loading rate before attaining steady state value of 9.4 J/m^2. The DIC data displayed similar behavior where the crack growth started at an initiation toughness value of 3 J/m^2. Correspondingly, the steady state toughness in the DIC data was obtained as 4.15 J/m^2.

The steady state toughness values were obtained from the fracture resistance curves for all the specimens tested in the manner just described. Furthermore, as already defined in the analysis, each specimen could be associated with a specific mode-mix via the mode-mix *vs.* thickness relationship defined in Figure 3.22. Armed with the toughness measurements and this relationship, a mixed-mode fracture envelope was obtained (Fig 3.26a) for the mode-mix values that were provided by the various values of the epoxy layer thickness that were accessed in this work. The data sets provided in the course of the experiments with IR-COI and DIC were very consistent.

The toughness at different mode-mix values was computed using the analytical model reflected in Eqn. (3.36) with various stiffness ratios. It can be seen (Fig. 3.26b) that the trend established by the stiffness ratio corresponding to the ratio of the shear and tensile moduli (0.369) did not match the data. In fact, a value of 2.18 was required for the best least squares fit to the normalized toughness envelope.

Similar envelopes were previously obtained for interfaces with the CIBA-Geigy epoxy and glass(Swadener and Liechti 1998) and sapphire (Mello and Liechti 2006). However, the toughness values in both cases were plotted against the nominal mode-mix values defined using stress intensity factors. The glass/epoxy toughness envelope (Swadener and Liechti 1998) matched (Fig. 3.26c) the toughness values obtained here with the silicon/epoxy interface for a length scale of 100μm. Nonetheless, the fact that Eqn. 3.36 is symmetric in mode-mix, suggests that the match for positive shear would not be so good due to the asymmetric nature of shielding established in a number of previous studies (Chai and Liechti 1992, Liang and Liechti 1995, Swadener and Liechti 1998, Mello and Liechti 2006).

Furthermore, on obtaining the mode-mix, the mode dependence of the critical CTOD measurements can also be obtained. This is shown in Fig 3.27 where the critical normal CTOD values from the IR-COI measurements and critical normal and shear CTOD values from the DIC measurements are observed with respect to mode-mix. The critical normal CTOD δ_{nc} does not show much variation with respect to mode-mix and has a mean value of 241 ± 45 nm. There was no clear trend for the critical shear CTOD from the DIC measurements. At this stage, it appears that both critical CTOD components are independent of mode-mix for the relatively small range that was provided by the ELS specimen. This means that the critical vectorial CTOD is independent of mode-mix for this silicon/epoxy interface. This has been observed for other interfaces previously (Liechti and Knauss 1982, Mello and Liechti 2006)

Based on the analysis, the main parameters needed to extract the normal and tangential traction-separation relations were the derivative of the J-integral with respect to the CTOD (normal or tangential), the stiffness ratio and the mode-mix of the specimen. As the stiffness ratio is a constant and each specimen could be associated with a specific

mode-mix based on the epoxy thickness, the derivative of the J-integral with respect to the CTOD was the chief factor that determined the uniqueness of each traction-separation relation.

Hence, the next step was to obtain the correlation of the J-integral with respect to the crack tip opening displacements (CTOD). The IR-COI technique as mentioned before, could be used to obtain the normal CTOD as a function of the applied displacement as shown in Figure 3.18. Correspondingly, the J-integral could be calculated for each value of the applied displacement as seen from the resistance curves. By associating these two quantities, the relationship between the J-integral and the normal CTOD can be obtained for the IR-COI experiments. Figure 3.28 shows this relationship for an experiment conducted using the IR-COI technique at a mode-mix of -51.3^{o}.

In the case of DIC, both the normal and tangential CTOD could be measured (Fig 3.19) as a function of the applied displacement. Correspondingly, similar to the IR-COI based experiments, the J-integral could be calculated for each value of the applied displacement. In the DIC based experiments, the J-integral can be linked with both normal and tangential CTOD values (Fig 3.29). Moreover, as mentioned previously (section 3.3.3), the extraction of the traction-separation relations through the DIC measurements can be accomplished by the use of either CTOD measurement.

In order to obtain the derivative of the J-integral with respect to the CTOD, a polynomial fit was applied to the data obtained as shown in Fig 3.28 and Fig. 3.29 using the curve fitting toolbox available in MATLAB. Care was taken to ensure that the fit covered the rising portion of the data as this determined the peak traction value during the analysis. Moreover, beyond this rising portion, the J-integral value tended to plateau to reach a steady state behavior. This region corresponds to zero tractions and thus was not

given much consideration during the fitting process. Since the extraction of the traction-separation relations depended heavily on the quality of the fit, each dataset analyzed was fit with a regression coefficient of no less than 0.92.

Once the fitting process was completed, the next step was to take the derivative of the fit and substitute it in Eqn. (3.29) to obtain the normal and tangential components of the mixed-mode traction-separation relation of the silicon epoxy interface (Fig 3.30). Irrespective of the technique used, the resolution is not high enough to capture the elastic region of the traction-separation relations. Hence the elastic region was assumed to be the characterized by the same stiffness as the value used in the analytical model developed in the mode-I experiment where $K_n = 2\text{x}10^{15}\ \text{N/m}^3$. Based on the stiffness ratio that best fit the toughness data, the value of the shear stiffness then became $K_t = 4.362\text{x}10^{15}\ \text{N/m}^3$. Furthermore, the nature of the fit generally tends to prevent a distinct critical crack opening displacement from being defined from the traction-separation relations. Hence, the critical CTOD measured (Fig 3.27) was used to define the point of zero tractions.

This analysis of the experiments provides the normal, tangential and vectorial traction-separation relation for each specimen analyzed and mode-mix. This not only provided information about the dependence of the normal, shear and vectorial strengths on the mode-mix value, but also suggested a damage initiation criterion that could be used in modeling the silicon/epoxy interface. The normal and the shear strengths as a function of the mode-mix are shown in Figure 3.31 and the vectorial strengths are plotted against the mode-mix in Figure 3.32. At this juncture, it should be remembered that the normal and shear strengths are related to each other by the relationship defined in Eqn. (3.28). It can be observed from Figure 3.31 that the normal strengths displayed a very slight dependence on mode-mix.

The shear strengths, on the other hand, increase along with the mode-mix because of the stiffness ratio and the mode-mix dependence established in Eqn. (3.28). Furthermore, at high mode-mix values (-68^o), it can be observed that the magnitude of the shear strength reached values as high as 82 MPa as compared to normal strengths whose value over the entire range of the mode-mixes tested remained quite independent for a mixed-mode experiments conducted at $17.8 \pm 1.34\,\text{MPa}$. The vectorial strengths varied based on the shear strengths (which are higher) and displayed the same trend with respect to mode-mix. Extrapolation of the vectorial and shear strengths can be conducted by applying the relationship between the normal and shear strengths. The vectorial strengths for the mode-mix values can be represented by Eqn (3.42).

$$\sigma_{v0} = \sigma_0 \sqrt{1 + \left(\frac{K_t}{K_n}\right)^2 \tan^2 \psi_\delta} \tag{3.42}$$

Based on the dependences observed in Figure 3.31 and Figure 3.32, it is clear that the shear strength were definitely higher at the mode-mixes considered. The normal strengths extracted from the mixed-mode experiments were observed to be independent of mode-mix and had a value of $17.8 \pm 1.34\,\text{MPa}$. Correspondingly, the shear strengths displayed a trend of tending towards zero at lower mode-mix values. These observations led to a hypothesis that damage in the cohesive zone initiates when either the normal or shear traction first exceeds the corresponding strength at a given mode-mix based on the data in Figure 3.31. The mode-I strength displayed here, however, cannot be compared to the normal strengths of the mixed-mode experiments conducted as the mode-mix value based on the CTOD measurements of the nominally mode-I experiment is not known.

Once the damage initiation is defined for an interface, the evolution of damage must be specified. Damage evolution corresponds to the softening behavior exhibited after the interface crosses the adhesive strength. In order to develop a common damage

evolution criterion, the damage evolution functions from all the experiments have to be obtained. Since the traction-separation relations were extracted on the basis of the normal CTOD, the damage evolution follows naturally from a rearrangement of Eqn. (3.27)

$$D = 1 - \frac{\sigma}{K_n \delta_n} \ . \tag{3.43}$$

Accordingly, the evolution of damage in the mode-I experiment and all the IR-COI based mixed-mode experiments were plotted together (Fig 3.33a) with respect to the normal CTOD in order to seek any similarity which might provide a common damage evolution function. The IR-COI measurements were chosen because of their higher resolution of the normal CTOD. It could be seen that except for the tail of the plot which is dependent on the fit, the relationship between the damage parameter functions of the mode-I and mixed-mode experiments were in very good agreement. Figure 3.33b demonstrates that the mode-I damage evolution compared well with the damage evolution obtained from one of the mixed-mode experiments conducted using IR-COI. Thus the mode-I damage evolution was taken to be the common damage evolution function for this interface.

In order to obtain a functional form for the damage evolution, the mode-I damage behavior was compared with the linear damage function (Eqn.(2.13)) and exponential damage function (Eqn.(2.14)) with different values of α (Fig 3.34). It can be seen that the exponential damage evolution with $\alpha = 3$ exhibits good agreement with the mode-I damage function with a correlation coefficient of 0.99.

On obtaining the traction-separation relations, the areas under the normal and shear traction-separation relation were computed to yield G_1 and G_2. Fig 3.22 shows a comparison of the mode-mix based on energy (Eqn. (3.23)) and the mode-mix based on the CTOD measurements Eqn. (3.24). A difference is observed between the two mode-mix values with respect to thickness. However, this is expected as the normal and shear

tractions have the stiffness ratio incorporated in their relationship (Eqn. (3.28)). This causes the mode-mix defined using the energy to be proportional to the definition based on the CTOD measurements.

The fracture surfaces of the mixed-mode experiments were characterized by conducting stylus profilometry and atomic force microscopy. Another technique that was considered was optical profilometry. Despite the non-destructive nature of this characterization technique, the transparency of the epoxy proved to be an issue when it came to measuring the transition between the Au/Pd coated region to the silicon/epoxy interface.

AFM images of the silicon/epoxy interface were taken using an Agilent 5500 atomic force microscope in tapping mode. Figures 3.35 and 3.36 show the fracture surfaces of the silicon/epoxy interface and the corresponding root mean square (RMS) roughness values for the fracture surfaces are tabulated in Table 3.1. Figure 3.35 shows the silicon/epoxy interface region of the top adherend well beyond the gold line. All three surfaces show similar features with regard to the topography of the surface. However, the corresponding roughness values increased by about an order of magnitude from mode I to the mixed-mode experiments, which were all quite similar.

Contrary to the trend exhibited by the top fracture surface, the bottom fracture surfaces displayed considerable differences in the topography with respect to mode-mix. At lower mode-mixes, (Fig 3.36a) the fracture surface seems to be quite similar to that of the mode-I fracture surface (Fig 2.25), though the roughness value of the surface is substantially higher than that of the mode-I surface. However, as the mode-mix value increased to -42^{o}, formation of 25-30 nm tall ridges was observed on the epoxy surface (Fig 3.36b). The formation of ridges for this particular mode-mix (-42^{o}) was accompanied

by a relatively smoother fracture surface with a RMS roughness value of 2.84 nm and the presence of ligaments was scarce. A similar ridge formation was observed in the fracture surface of a specimen with a larger mode-mix of -51.3^o as shown in Fig 3.37b. Here the ridges were observed to be fewer in number and more widely spaced (>50 μm). However, when the fracture surface of a specimen that delaminated at a mode-mix of -60.8^o was observed (Fig. 3.36c), the ridge formation had diminished and ligaments were more prevalent. This type of ridge formation has been observed previously for glass/epoxy interfaces (Swadener et al. 1999) for both mode-I and mixed-mode fracture surfaces where the creation of the ridges was attributed to the incremental propagation of the crack front. However the fracture surfaces seem similar to some of the fracture surfaces reported in the literature. Button shear tests conducted by Sham and Kim (Sham and Kim 2003) to study the adhesion behavior of underfill epoxy resins have shown that the shear tests caused multiple modes of fracture depending on the material the underfill was bonded with. For underfill resins bonded to inorganic passivation surfaces such as SiO_2 and Si_3N_4, they report that the resin delaminated from the surface by a combination of interfacial and cohesive failure within the underfill leaving behind tiny underfill resin particles on the passivation surfaces.

The transition between the Au/Pd region and the silicon/epoxy interface was then observed by using AFM and stylus profilometry. Figure 3.37 shows AFM images of the bottom fracture surface of a specimen delaminated at a mode-mix of -51.3^o in the Au/Pd region (Fig 3.37a) and in the silicon/epoxy interface (Fig 3.37b). It can be seen that the roughness value decreases considerably during the transition. Next, the whole transition region was observed for two mode-mix values (-34.5^o and -51.3^o) by conducting a 50 x 90 μm scan using the AFM. Figure 3.37 shows an AFM image of a bottom adherend of a specimen with a mode-mix of -51.3^o after fracture and a stylus profilometer scan of the

transition region. A crack jump of about 100 nm is observed when the crack grows from the Au/Pd region to the silicon/epoxy interface (Fig 3.38b). Furthermore, the RMS roughness in the Au/Pd region was observed to increase from 14.3 nm to 35 nm as the gold line was approached. Moreover, this transition in roughness could be observed as the ligaments closer to the gold line in Fig 3.38a on the Au/Pd coated region grow in size till the crack began to grow into the silicon/epoxy interface. This can be attributed to the end effect exhibited by the gold line. However, as expected from the image, the RMS roughness of the region after the crack progressed into the silicon/epoxy interface was at a relatively much lower value of 3.4 nm.

On the other hand, the top adherend of the same specimen did not exhibit a sharp transition region as expected (Fig. 3.39). However, the gold line could still be observed based on the transition from a sparsely populated surface with large ligaments to a surface with fine ligaments in high density. Contrary to the bottom fracture surface, the RMS roughness difference between the Au/Pd region and the silicon/epoxy interface was not as distinct as that of the bottom adherend. The RMS roughness value of the Au/Pd region was 10.2 nm while the corresponding epoxy surface roughness value was 8.5 nm. However, compared to the roughness values observed in the mode-I experiment, the roughness values of both the top and bottom fracture surfaces were much larger in the mixed-mode experiment (Table 3.1).

Figure 3.40 shows the AFM images of the gold line in the bottom adherend of specimens with different mode-mix values. It could be seen that at a lower mode-mix, the transition region is much more gradual than the one with the higher mode-mix.

Based on the AFM images, it can be observed that the top adherend did not display distinct features such as ridge formation. However, the average ligament height of the areas observed, varied between 4-40 nm for mode-mix values from nominally mode-I

to a mode-mix value of -60.8^{o} (Fig. 2.25 and Fig 3.35). This indicated that the crack grows closer to the interface under nominally mode-I conditions than under mixed-mode conditions. Furthermore, observation of the variation of ligament and ridge formations on the fracture surface of the bottom adherends with respect to mode-mix showed that the delamination process occurred through the fracture of ligaments at lower mode-mixes. However, intermediate mode-mixes displayed ridge formations though these ridges diminish as even higher mode-mixes are reached. In order to observe correlation between the roughness values in the mixed-mode experiments, a comparison was made with the epoxy thickness of the respective specimens (Fig 3.41). Overall a correlation could not be observed between the roughness and the mode-mix or the thickness of the epoxy, though the roughness value shows a gradual increase with the thickness of the epoxy. The major point of difference was that the mode-I fracture surfaces were observed to be much smoother..

The formation of the ligaments can also be related to the type of interface that is formed during the curing process. Depending on the wettability of the epoxy and the surface chemistry between the epoxy and the native silicon dioxide present on the silicon surface along with the presence of hydroxyl ions at the surface (as the specimen preparation takes place in ambient conditions), the formation of a compound interface comprising of an oxide rich interphase region is possible. It has been shown previously (Sham and Kim 2003) that at the interface, the underfill reacts with the silicon dioxide to form organosilanes which could happen in the case of the silicon/epoxy system here. Furthermore, at the molecular level, the epoxy is in contact mainly with the silicon dioxide layer present on the silicon surface, there is a possibility of mechanical interlocking of the epoxy molecules with the silicon dioxide molecules thus forming a mixed interface with chemisorption and mechanical interlocking as the adhesion

mechanisms. The mechanical interlocking of epoxy with inorganic oxide layers such as Al_2O_3 has been observed previously by certain groups (Schmidt and Bell 1986).

Thus, a factor to be considered here is that the crack path could be traversing the interphase between the silicon and the epoxy. The interphase is defined as a region of finite thickness between the adherend and the adhesive where the adhesive interacts with the adherend creating a phase which possesses different material properties (Sharpe and Schonhorn 1964, Sharpe 1972). The thickness of the interphase has been reported to vary for different material systems depending on the measurement technique, and the materials involved (Downing et al. 2000). It is widely accepted that the mechanical behavior of polymer based composites is considerably dependent on the interphase between the fiber and the matrix. Epoxy/metal systems have been shown in the past to display the formation of an oxide rich interphase formed due to the surface reaction between the metal oxide and the hydroxyl ions of the epoxy (Schmidt and Bell 1986). Theories developed by researchers previously (Drzal 1986, Schmidt and Bell 1986, Sancaktar 1996) have suggested that the interphase could govern the interfacial delamination process and would have to be characterized as a separate entity. Characterization of the interphase and its effect on the mechanical properties of the system has been reported in the literature previously by many groups (Downing et al. 2000, Wang 2004, Sperandio et al. 2010). In metal epoxy interphases, Schmidt and Bell (Schmidt and Bell 1986) report that the curing epoxy mechanically embeds into the oxide layer structure. On failure, considerable plastic deformation of the epoxy occurs with the pore and fibrous ends of the epoxy acting as the nucleating sites for the deformation. This seems to agree with the fracture surfaces with the ligaments observed in the AFM images.

Next, the obtained traction-separation relations were input into an ABAQUS simulation of the ELS experiment. On obtaining the mixed-mode traction separation

relations for the experiments, a common fracture criterion was established with the following parameters provided as the input to the model. The elastic part of the traction-separation relation was defined by the values of $K_n = 2\,\text{x}10^{15}$ N/m^3 for the normal stiffness and $K_t = 4.36\,\text{x}10^{15}$ N/m^3 for the shear stiffness. To force the normal strength to be the driving criterion, the values of the maximum normal and shear strengths in the quadratic stress criterion (Eqn. (3.37)) were fixed as the normal strength being similar to the mode-independent value obtained in the experiments ($\sigma_0 = 18$ MPa) and the maximum shear strength was set as a large value ($\tau_0 = 1$ GPa). This made sure that the damage would initiate as soon as the normal strength reached σ_0. In order to observe the trend in the toughness as the thickness of the epoxy increases, four different thickness values were considered for the model (5,8,9.3 and 35 μm).As we know the mode-I toughness to be 1.76 J/m^2 , the peak strength value to be 18 MPa and the normal critical displacement, δ_{nc}, to be equal to 241 ± 40 nm (Fig. 3.27), we can estimate the value of the shape factor α as equal to 1. Furthermore, the normal critical separation at peak traction, δ_{n0}, can be estimated by using the normal strength σ_0 and normal stiffness K_n as 9 nm. With both these values (δ_{nc} and δ_{n0}) the critical effective displacement ($\delta_{vc} - \delta_{v0}$) can be extracted using the Eqn. (3.41) to obtain δ_{vc} and δ_{v0}. The input for the range of mode-mix values is shown in Figure 3.42 where $\delta_{vc} - \delta_{v0}$ is plotted against ψ_{Ga} (Eqn. (3.40)). The input parameters of the traction-separation relation used in ABAQUS are summarized in Table 3.2.

Figure 3.43 shows a comparison between the load-displacement response obtained from the experiment and the one obtained from the model for a specimen with an epoxy thickness of 8 μm and an initial crack of 21.4 mm. It can be observed that

initially, the response of the load with respect to the displacement in the model agrees well with that of the experiment. However, the load at which the crack propagates in the model is considerably different as compared to that in the experiment. In the experiment the crack growth starts at about 1.2 N whereas in the model, the crack growth is observed to start at about 0.88 N. This is again reflected in the fracture resistance curve for the specimen (Fig. 3.44). Because of the low load at which the crack propagates in the model, the steady state toughness obtained, (2.52 J/m^2) is considerably lower than the toughness value obtained for the experiment (9.3 J/m^2). It can be seen that the fracture resistance curve from the experimental measurements is seen to be a distinct rising curve while the model exhibits a flat resistance curve initially but after the crack grows to about 0.8 mm, a very gradual rise is observed. Next, the mode-mix based on the CTOD definition (Eqn.(3.24)) was obtained by extracting the normal and shear crack tip opening displacements from the model. The behavior of the CTOD was very similar to that of the experiment with respect to the shape of the CTOD curves (Fig. 3.45). Prior to crack growth the CTOD values increased gradually with respect to the displacement. At the onset of crack growth, the CTOD values increased tremendously with respect to the displacement. A comparison plot of the mode-mix with respect to the thickness of the epoxy is shown in Figure 3.46. The mode-mix obtained from the model with respect to epoxy thickness does not agree with the mode-mix obtained from the DIC measurements. Rather, the mode-mix obtained from the model, agrees well with the mode-mix defined based on the stress intensity factors. In order to observe the toughness differences between the model and the experiments, the toughness was plotted with respect to the

epoxy thickness (Fig. 3.46). It can be observed that the toughness obtained in the model does not vary much even though it exhibits a small decrease as the thickness of the epoxy layer increases. However, as the model is purely elastic, no plastic dissipation is taken into account. It has been observed previously by researchers that the plastic dissipation contribution becomes dominant as the shear component of the mode-mix increases (Swadener et al. 1999)

The traction-separation relation for the specimen was extracted and is shown in Fig 3.47. Based on the input provided, the normal strength does drive the delamination process. However, the shear strength was not as high as was observed in the experiments for this specimen. Furthermore, in the experiments, the analysis that was employed forced the shear tractions to be proportional to the normal tractions by Eqn. (3.28). In the case of the model, this was clearly not observed.

Local plastic yielding of a material or both materials of a bi-material system has been known to change the local mode-mix of the interface. (Tilbrook et al. 2005). Even if at the bulk level the yielding of the epoxy is not noticed, the AFM images show that there is evidence of the epoxy yielding at the interface/interphase region discussed earlier. The effect of the interphase on mechanical properties of a polymer thin films on silicon substrates have been shown to extend to relatively large depths using nanoindentation measurements (Wang 2004). Research in composites has shown that the strength of the interphase plays a crucial role in determining the strength of the composite itself and needs to be taken into account while modeling (Drzal 1986, Taliercio 2007, Needleman et al. 2010). Furthermore, local effects such as crack blunting (Evans et al. 1989) prior to

crack propagation can play a major role in defining the local mode-mix based on the CTOD. Incorporating such effects could bring about a better agreement between the model and the experiments.

CHAPTER 4: CONCLUSIONS AND FUTURE WORK

In order to characterize delamination along an interface under any loading condition using the cohesive zone modeling approach, it is essential that a common criterion be established which defines the damage initiation required for predicting the onset of the failure process. Furthermore, knowledge of the damage evolution process, that succeeds the initiation, is required to define the path that would lead to complete failure of the interface.

In order to establish such a criterion, the mode-dependence of the interfacial properties was studied by subjecting a silicon/epoxy interface to different mode-mix conditions. Silicon/epoxy sandwich specimens were fractured under mode-I and mixed-mode loading conditions in order to first observe interfacial crack growth at steady state. This enabled the determination of steady state fracture toughness for a range of mode-mix values. Furthermore, the mode-dependence of normal, shear and vectorial components of the adhesive traction-separation relations was obtained. Although the two epoxies that were used in the study were supposed to be the same product, they were provided by different suppliers and had slightly different formulations that affected their mechanical behavior, their adhesive behavior turned out to be quite similar.

The first task was to conduct nominally mode-I fracture experiments on DCB sandwich specimens in order to extract the mode-I cohesive relations. Direct and iterative methods for extracting traction-separation relations of the silicon/epoxy interface were compared. The direct method for extracting the mode-I traction-separation relation through the J-integral approach was based only on measurements of NCOD and some analysis. Infra-red crack opening interferometry (IR-COI) determined the normal crack opening displacements near the crack tip at a resolution of 20 nm. Moreover, IR-COI was

used to track the crack front during propagation and make measurements the crack length. The analysis was limited to models based on simple beam theory and beams on elastic foundations.

The iterative approach involved a parametric study using finite element simulations with candidate cohesive traction-separation relations to determine the NCOD. The results were compared with the measurements to in order to identify the actual traction-separation relation. The comparison study showed that the calculation of an accurate J-integral value steered the precision of the traction-separation relation that was determined by the direct method. Furthermore, the damage evolution derived from the direct method and the best solution from the iterative method was observed to be exponential in form. Nonetheless there were some differences in the details of the traction-separation relations obtained by the two approaches and, in the end, the iterative approach provided the best agreement with the measured NCOD (Fig. 2.22).

The next task was to conduct mixed-mode experiments and extract the interfacial traction-separation relations for different mode-mix values. This was accomplished by developing a new loading device to conduct mixed-mode fracture experiments on silicon/epoxy sandwich specimens in an end-loaded split configuration. The device could be modified easily to enable compatibility with IR-COI or digital image correlation (DIC) as techniques for measuring displacements near the crack front. The advantage of DIC was that both normal and tangential displacements at the crack tip could be measured. As demonstrated, these measurements provided a direct measure of the mode-mix of each specimen, which was dictated by the thickness of the epoxy layer. The variation of toughness with mode-mix was used to select the stiffness ratio of the tangential and normal traction-separation relations prior to the initiation of damage. The evolution of damage was based on a maximum strength criterion, thereby completing the

determination of the normal and shear traction-separation relations for any particular mode-mix.

Each mode-mix provided a steady state toughness value along with the normal, shear and vectorial traction-separation relationship. Based on the mode-dependence of the normal and shear tractions, it was concluded that the normal tractions controlled the fracture process. This allowed the establishment of the maximum stress damage criterion for the interface. Furthermore, the damage evolution process, which was determined by comparing the damage functions of different mode-mix values, was observed to exhibit a common exponential softening form.

The portions of the toughness envelope obtained in this work were for the silicon/Huntsman epoxy interface. Owing to the similarity in composition to the CIBA-Geigy epoxy, the toughness envelope of the silicon/epoxy interface was compared to the interfacial toughness envelope of glass/epoxy (Swadener and Liechti 1998). Both interfaces seem to show similar toughness values for the range of mode-mixes considered. Furthermore, quartz/epoxy and sapphire/epoxy have shown very similar toughness values (Mello and Liechti 2004, Mello and Liechti 2006) at the mode-mixes considered as well.

Extraction of the traction-separation relations for different mode-mixes thus provided a damage criterion that not only indicated the point of damage initiation for each mode-mix but also specified the critical displacement at which a steady state condition is attained. From the standpoint of microelectronic devices, this proves to be very significant as length scales of the order of micrometers tend to be vital in the reliability of chip packages.

Analysis of the fracture surfaces was conducted to study the mechanisms involved in the fracture process. XPS conducted on mode-I fracture surfaces showed that the Au and Pd were present on both surfaces after the experiment, which indicated that the Au/Pd layer was partly peeled off the silicon by the epoxy during the initial crack creation process. Beyond the gold line, both fracture surfaces contained nitrogen, indicating that the crack path was cohesive in the epoxy. Furthermore, the presence of silicon in the survey scan of the top adherend indicated that the crack path was less than 10 nm away from the top silicon/epoxy interface. Moreover, in both mode-I and mixed-mode experiments, since the crack front was visible through the microscope and the fringes were present throughout crack propagation, the crack growth was definitely close and almost parallel to the interface. Furthermore, in the mixed-mode experiments, DIC images of crack propagation clearly show the crack propagating near the top interface between silicon and epoxy. Stylus profilometry based studies of the mixed-mode fracture surfaces showed that the transition of the crack from the Au/Pd region to the silicon/epoxy interface displayed a jump of about 100 nm into the epoxy when the bottom adherends were observed.

In order to obtain information at an even smaller scale, AFM analysis of the fracture surfaces was conducted. Observation of the epoxy surface and the top adherend showed the presence of ligaments which were very dense on the epoxy surface but relatively scarce on the silicon surface. This explained why the profilometer was unable to observe the presence of any features on the top surface. Furthermore, observation of the transition region showed that ligaments are much finer on the epoxy side than on the Au/Pd coated surface. Prior to crack growth from the initial crack front (i.e. the gold line) the ligaments increase in height before the crack crosses over into the silicon/epoxy interface where the surfaces are much smoother than the Au/Pd coated region. However,

mixed-mode specimens with thicker epoxy layers (i.e. corresponding to lower mode-mix values) did not display such a stark contrast between the two regions. This difference between the fracture surfaces of thick epoxy specimens and thin epoxy specimens can also be related to the respective toughness values. The thicker epoxy specimen corresponding to the lower toughness value showed less deformation of ligaments at the initial crack front than that of the specimen with the thin epoxy layer. Furthermore, ridge formation in the fracture surfaces of the mixed-mode specimens was observed beyond the gold line and in the silicon/epoxy interface similar to what was observed in the glass/epoxy interface previously (Swadener et al. 1999). However at higher mode-mix values the ridge spacing began to increase and the ridge height tended to diminish. However, the crack path at the silicon/epoxy interface could be hypothesized by considering the kind of interface that develops between the native silicon dioxide and the epoxy to be a mixed interface formed by a chemically bonded interphase formed by the creation of organosilanes and mechanical interlocking of epoxy and silicon dioxide molecules.

A purely elastic tri-layer model was constructed in ABAQUS in order to simulate the mixed-mode experiment and employ the traction-separation relation and observe the mode-dependence obtained in the experiments.. However, reasonable agreement between the solutions obtained from the model and the experimental measurements was not obtained. Major reasons for the differences observed can be attributed to the absence of plasticity present in the model, effects of crack blunting and the absence of an interphase layer. Nevertheless, the toughness obtained from the model could be attributed to the intrinsic toughness component of the interface because of the almost constant nature of the toughness value with respect to thickness of the epoxy. Further investigation into this

as conducted previously (Swadener et al. 1999) could confirm this value as the intrinsic toughness of the silicon/epoxy interface

4.1 FUTURE WORK

This doctoral work has provided a direct approach to extract the mode-dependence of the silicon/epoxy interface and obtain a criterion that could be used to model the fracture process. However, considerable amount of research and development can be conducted which could provide deeper insight into understanding the failure mechanism. Further analysis of the ligaments that formed on the fracture surfaces could lead to better understanding of the failure mechanism. Relating higher toughness values to larger differences in ligament height and density could provide more quantitative information about the plastic dissipation at higher mode-mixes. Based on the results obtained for this interface a study of the plastic dissipation of this epoxy could be pursued which would help in obtaining the intrinsic toughness values of the interface at various mode-mixes. Previous studies have shown the intrinsic toughness of glass/epoxy, quartz/epoxy and sapphire/epoxy to be independent of mode-mix (Swadener and Liechti 1998, Mello and Liechti 2004, Mello and Liechti 2006). However, functionalization of the surface led to mode-dependent intrinsic toughness values (Mello and Liechti 2006).

The incorporation of DIC to measure local properties in the mode-I experiments could be helpful in obtaining the small shear component for the DCB tests. Furthermore, the automation of the mode-I loading device would be a substantial improvement in conducting the experiments in a more controlled manner. Moreover, rate-dependent mode-I tests could be conducted to study the effect of viscoelastic properties of the epoxy on the interfacial properties.

In order to obtain a deeper understanding of the fracture experiments conducted and study the adhesion mechanism, it would be a good notion to investigate the interphase region at the interface of the silicon and epoxy. In polymer matrix composite systems, the interphase region has been widely accepted as the governing component of the mechanical properties of the polymer (Drzal 1986). Quite a few characterization techniques have shown that the effect of the substrate on the properties of the adhesive causes differences in the mechanical properties close to the interface. Characterization techniques such as nanoindentation (Wang 2004), phase imaging AFM (Downing et al. 2000), force modulation AFM (Mai et al. 1998), controlled pressure SEM (Sperandio et al. 2010), scanning force microscopy (Munz et al. 1998) and other methods have been used to determine the properties of the interphase in different material systems. As mentioned in the introduction, a rigorous understanding of adhesion between two materials can only be obtained when the surface chemistry and physics, polymer chemistry and physics, rheology and fracture mechanics are combined and studied.

A way to enhance our knowledge about the polymer chemistry of the epoxy (or interphase) would be to characterize the epoxy by using a technique such as Fourier transform infrared (FT-IR) spectroscopy. This technique has the ability to provide the gradient in the chemical structure of the epoxy resin at the interface as a result of the curing process. It has been shown to be useful in studying the polymer chemistry of the epoxy at glass/epoxy interfaces in composites (González-Benito 2003).

The plane strain trilayer model that was developed for the mixed-mode experiment could be improved by incorporating plasticity or furthermore, viscoelastic/viscoplastic behavior (Mello and Liechti 2006) in the epoxy layer, after characterizing the respective properties through relaxation tests on epoxy coupon specimens. Incorporation of an interphase layer into the model after the characterization

suggested above could improve the model to provide better agreement with the experiment. Deformation of the interphase layer has been shown in the past to greatly influence the mechanical properties of polymer based CNT composites (Needleman et al. 2010). This could be the case here as well. Moreover, the CTOD measurements made using 2D-DIC to extract the mode-mix are restricted to one side of the specimen unlike the IR-COI technique which provides 3D information. Hence, the variation of the CTOD values along the width of the specimen is unknown. Knowledge of this variation could further enhance the understanding of the delamination process and the definition of the mode-mix. A higher resolution can be attempted by using a higher magnification objective to capture the DIC images as well.

Another important factor that can be studied is the effect of moisture on the interfacial properties of the silicon/epoxy specimen. Previous studies have shown that epoxies can absorb 1-7% moisture (Soles and Yee 2000). Studies have also shown that the effect of moisture affects interfacial toughness in epoxy underfills used in microelectronics (Ferguson and Qu 2003, Ferguson and Qu 2004). Modifying the mode-I and mixed-mode loading devices by integrating the capability of controlling the environment but retaining the full use of the measurement techniques would be an interesting development to consider. Controlling the moisture level or vacuum level inside the device could provide valuable information about the effect of moisture.

A number of modifications can be made to the loading device. A study on nominal mode-II experiments could be pursued by modifying the loading device for ENF specimens. This would provide a good range of mode-mix values and also provide the mode-II fracture toughness, which would be helpful in modeling the interface. Furthermore, incorporating DIC in these tests would enable direct determination of

mode-II traction-separation relations, as the tangential CTOD can be measured using DIC. The same interface could be studied by conducting experiments at different rates. This can be used to extract rate-dependent mixed-mode traction-separation relations. The advantage of DIC is that there is no material dependence. Unlike COI, where the material needs to be transparent to the source, The DIC technique can be used on any surface as long as there is a speckle pattern fine enough to resolve the displacements. This opens up possibilities of studying multilayered specimens with other metallic substrates involved.

FIGURES

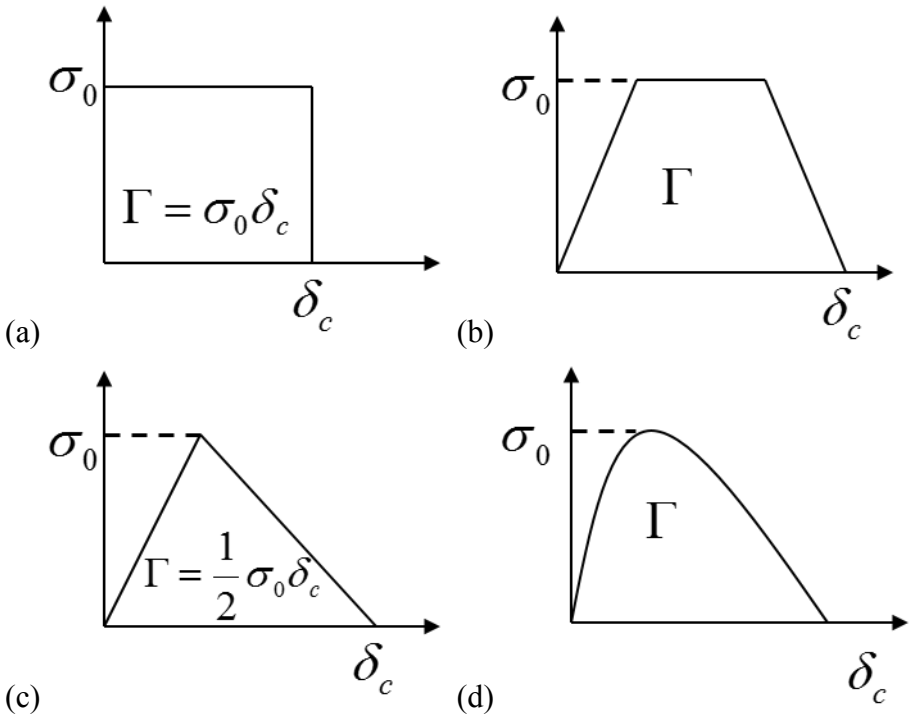

Figure 1.1: Traction-separation relations (a) Dugdale Model (b) trapezoidal model (c) bilinear model (d) generalized form

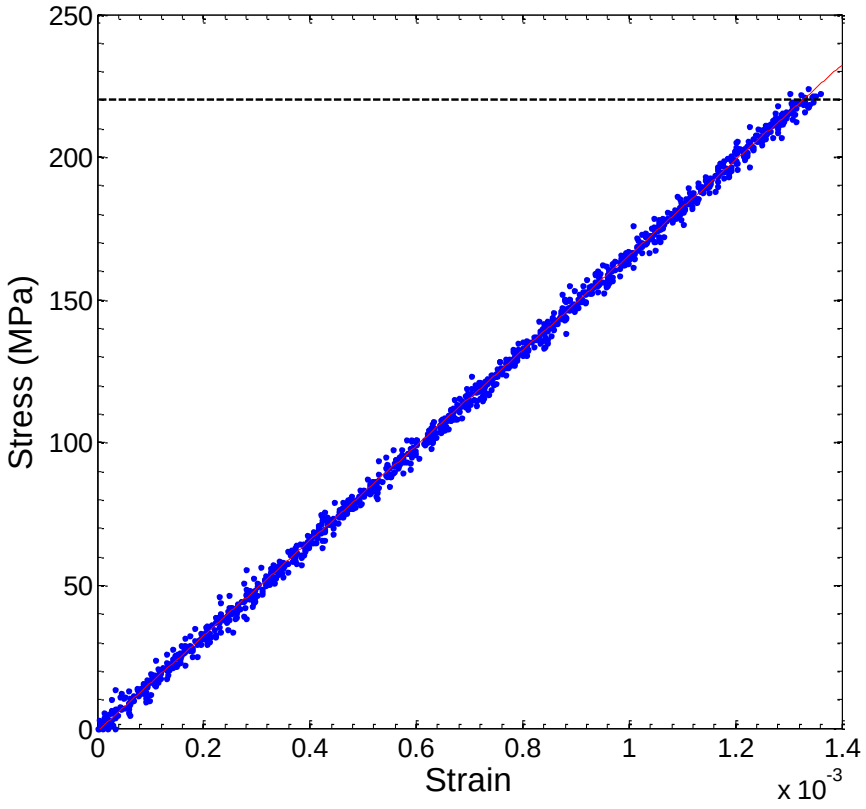

Figure 2.1: Stress-strain behavior of silicon (111)

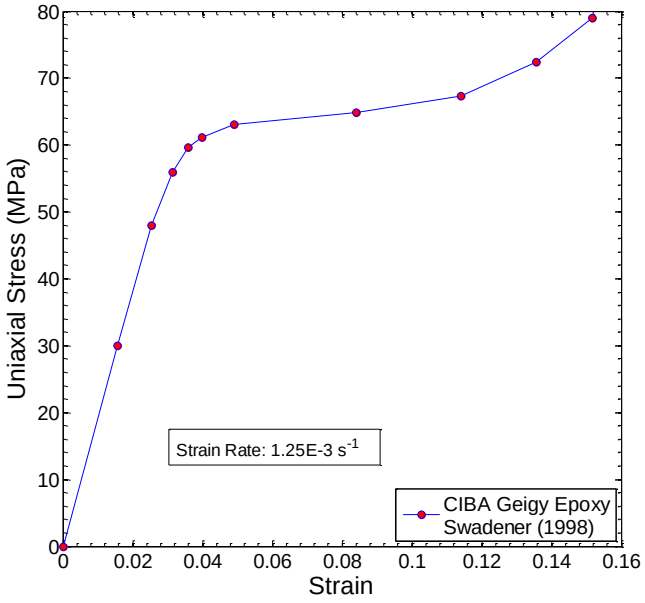

(a)

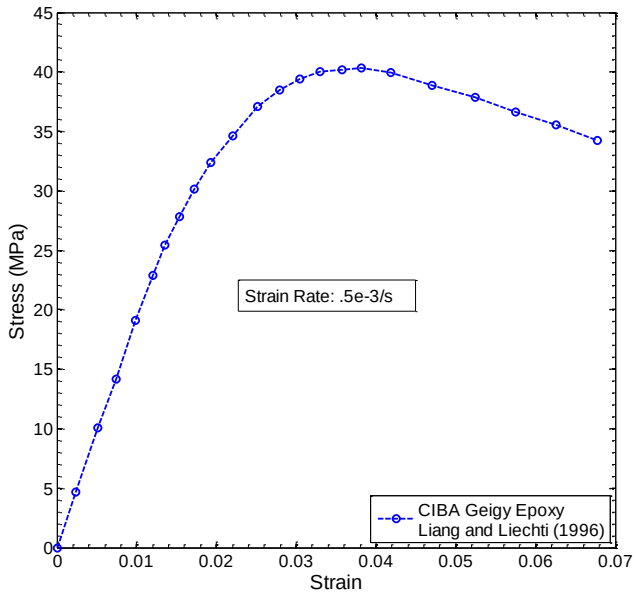

(b)

Figure 2.2: Stress-strain behavior of CIBA-Geigy® epoxy (a) under uniaxial compression (Swadener 1998) (b) uniaxial tension (Liang

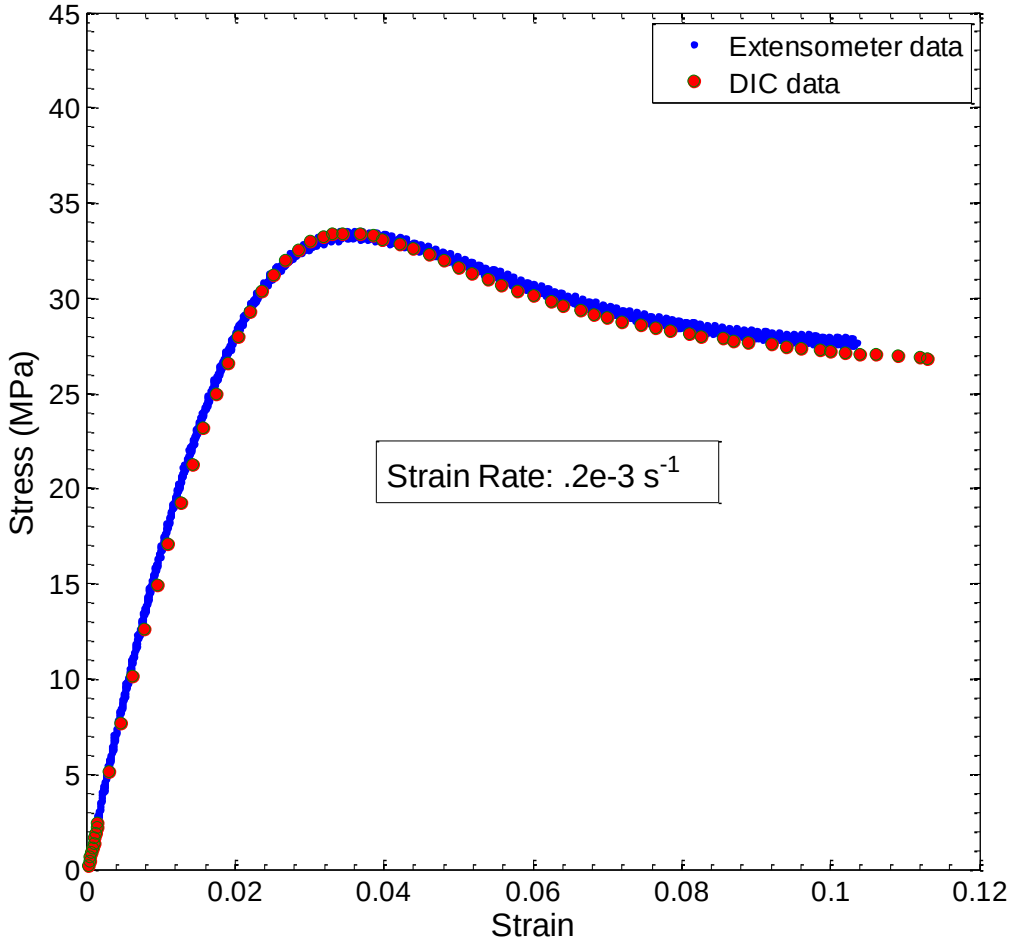

Figure 2.3: Stress-strain behavior of the Huntsman® epoxy under uniaxial tension.

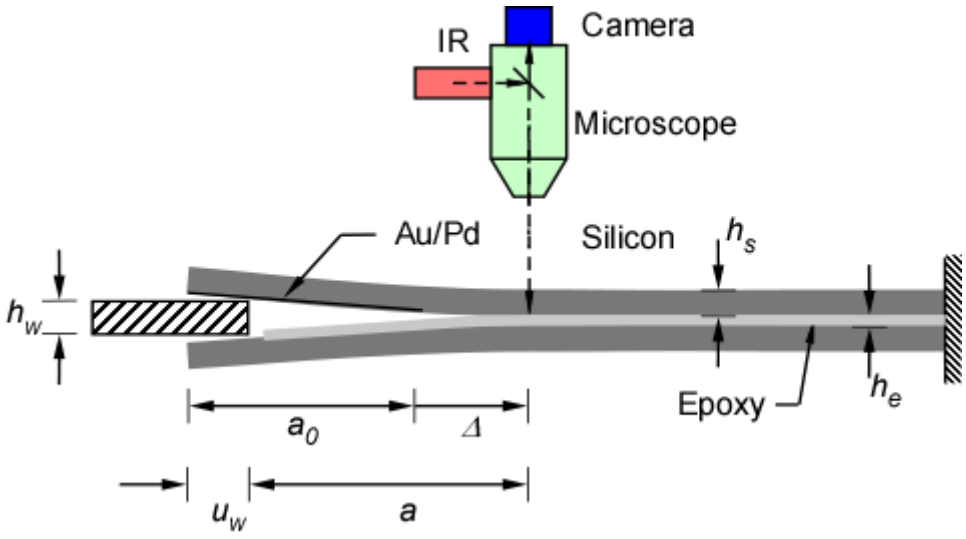

Figure 2.4: Schematic of the DCB specimen and apparatus

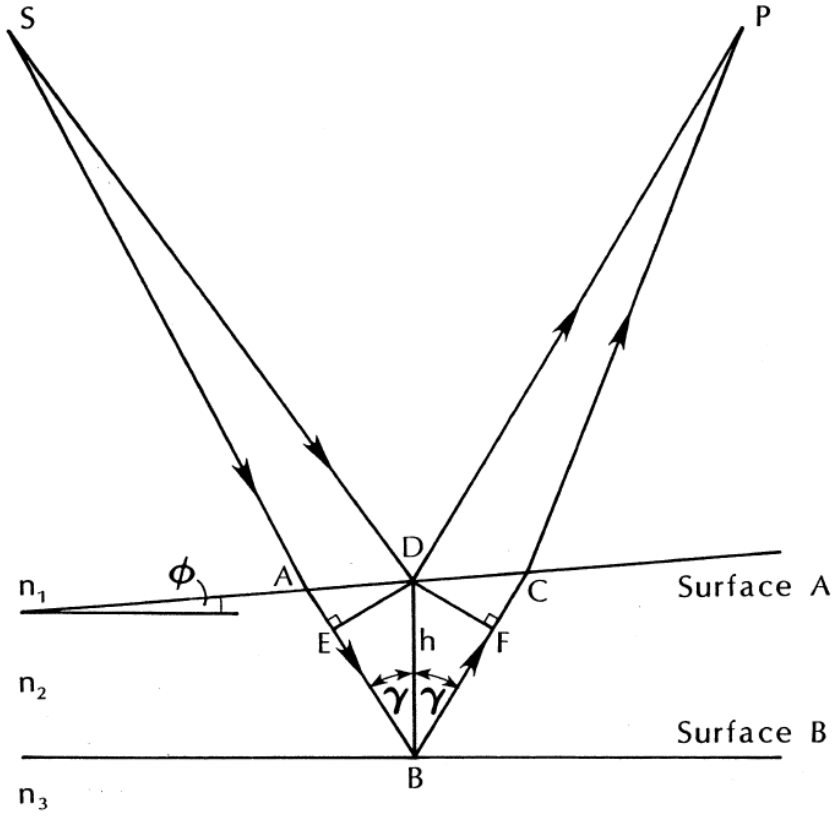

Figure 2.5: Ray diagram for the formation of interference fringes between crack faces. (Liechti 1993)

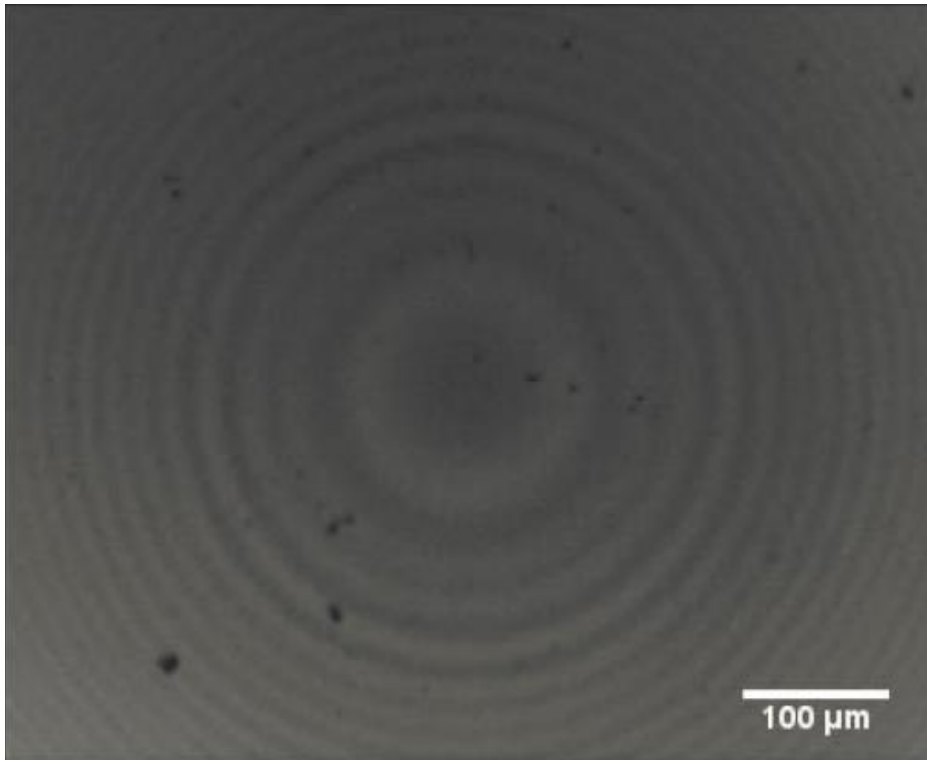

Figure 2.6: IR-COI validation- Newton's Rings

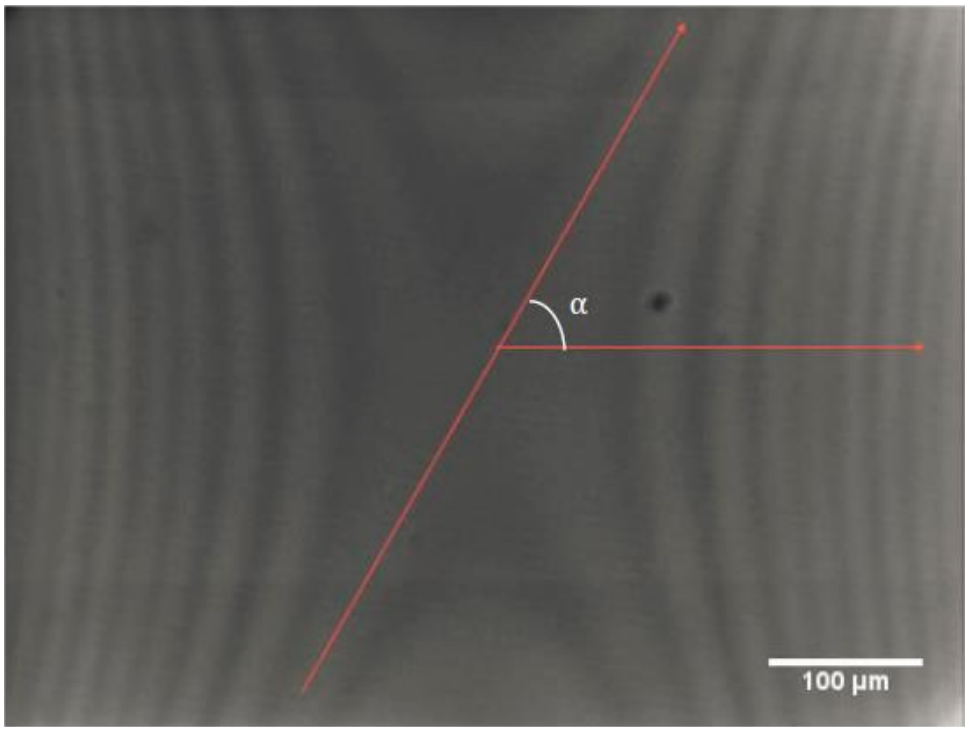

Figure 2.7: IR-COI validation- hyperbolic fringes from the four point bend test

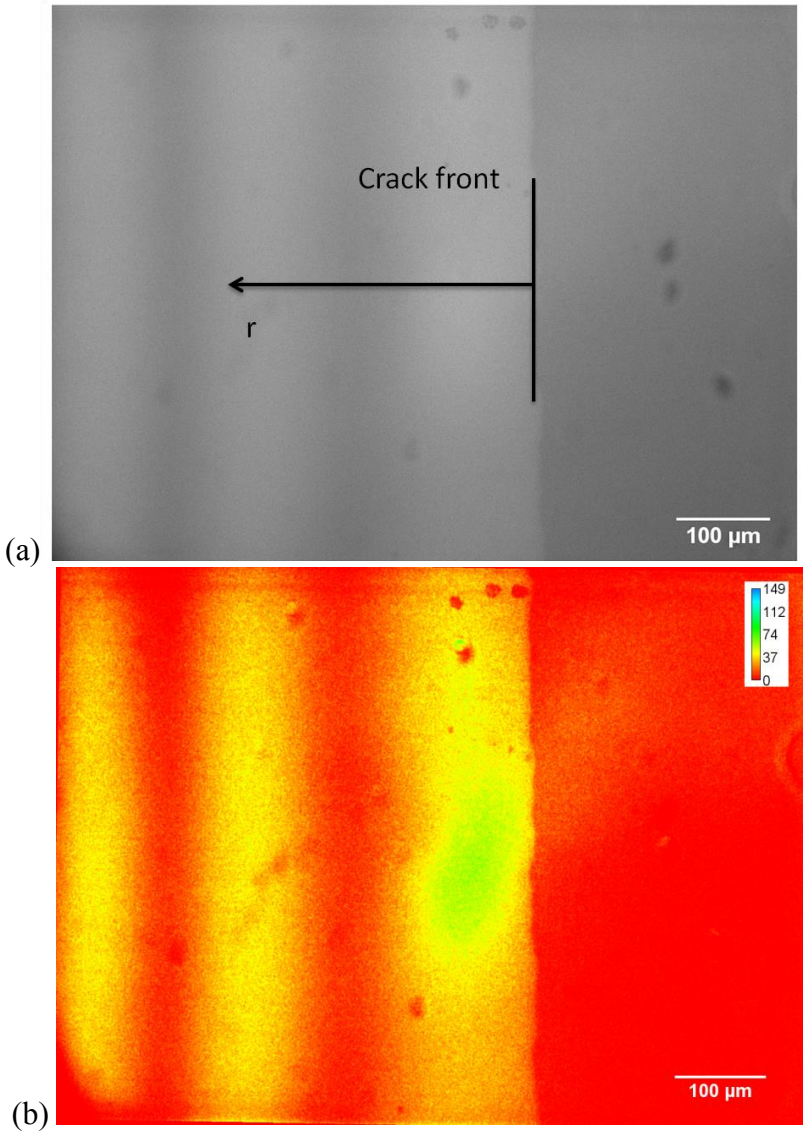

Figure 2.8: A typical interferogram of the crack-front with the fringes due to crack opening and the dark area representing the bonded region of the silicon/epoxy interface. (a) A grayscale image and (b) a red-green colored image with background variations removed.

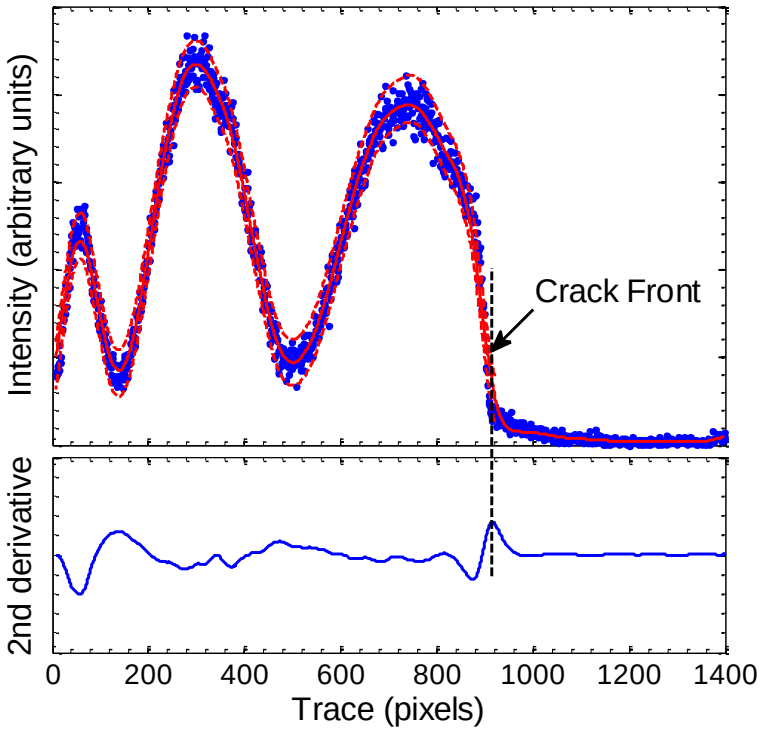

Figure 2.9: An intensity profile and the curve fit to the data along with the 95th percentile bounds and the second derivative of the fit.

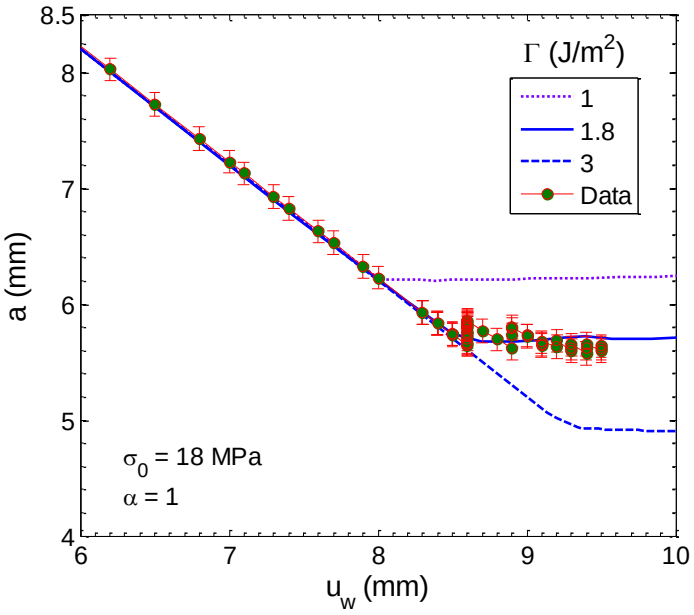

(a)

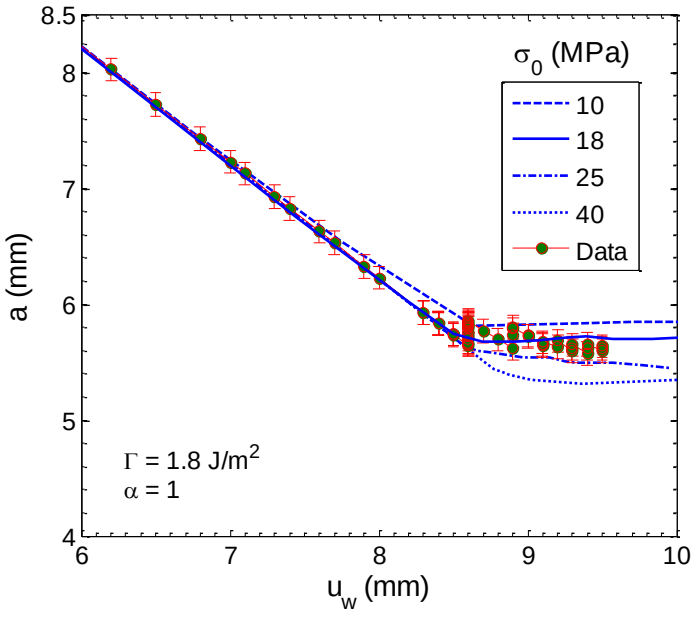

(b)

Figure 2.10: Measurement of crack length with respect to wedge insertion, in comparison with numerical simulations with: (a) different interfacial toughness values and (b) different interfacial strength values.

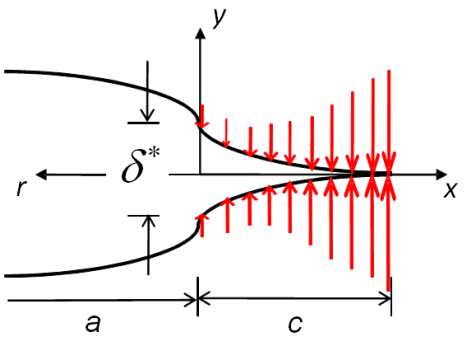

Figure 2.11: A schematic of the crack front geometry and cohesive zone.

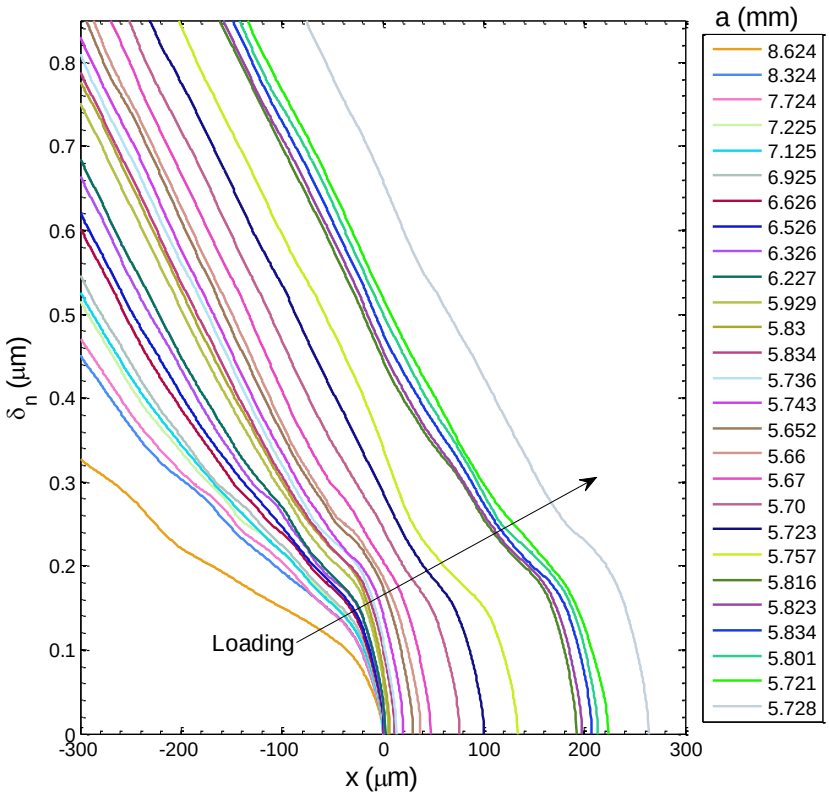

Figure 2.12: The normal crack opening displacement (NCOD) measured by IR-COI as a function of the distance from the initial crack front ($x = 0$).

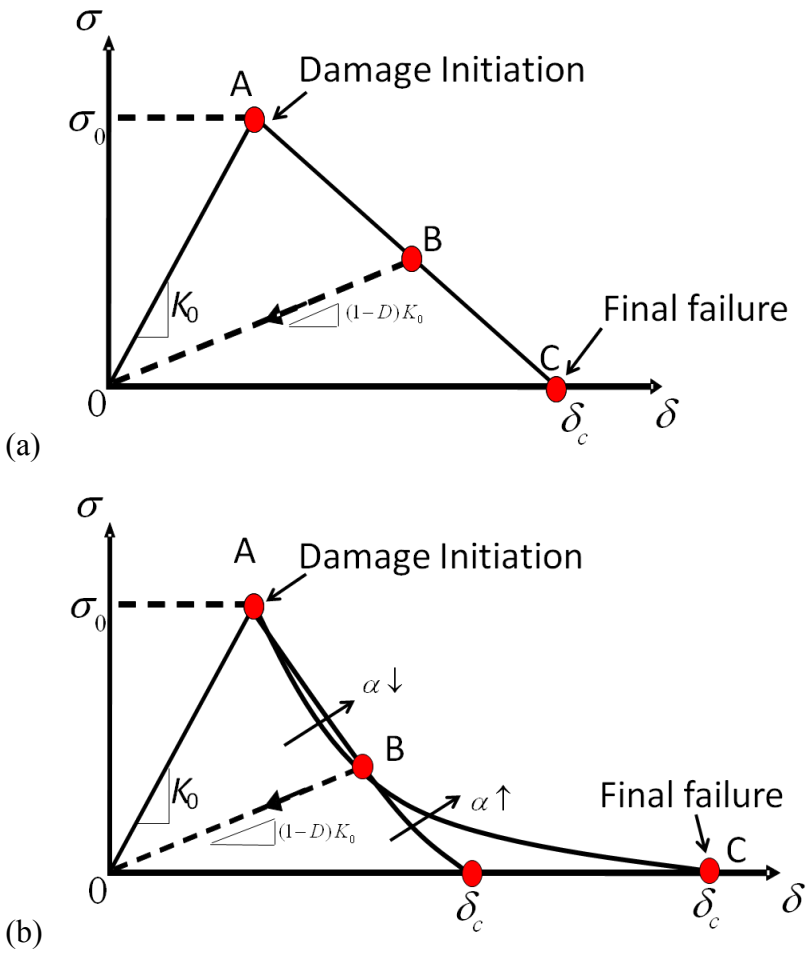

Figure 2.13: Two types of traction-separation relation: (a) a bilinear model, and (b) a linearly elastic relation followed by exponential softening. The quantity δ_m in Eqs. (3)-(7) equals δ during loading (crack opening) but remains a constant during unloading (crack closing).

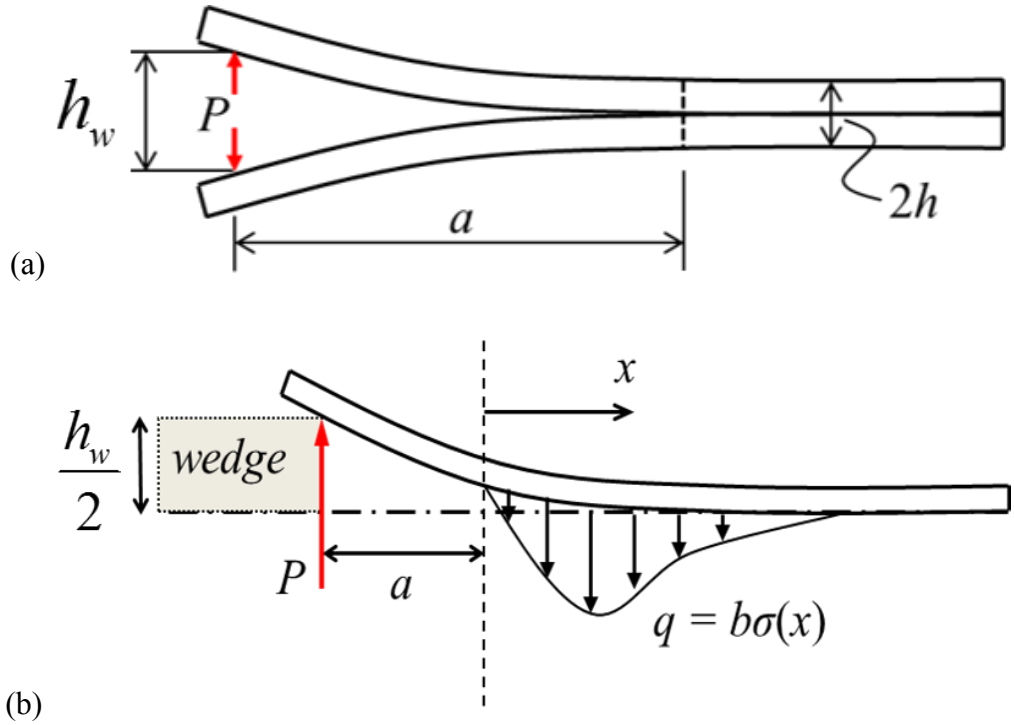

Figure 2.14: Schematics of DCB models. (a) A simple beam model with zero root rotation; (b) The upper beam in a wedge-loaded DCB specimen with cohesive interactions ahead of the crack tip.

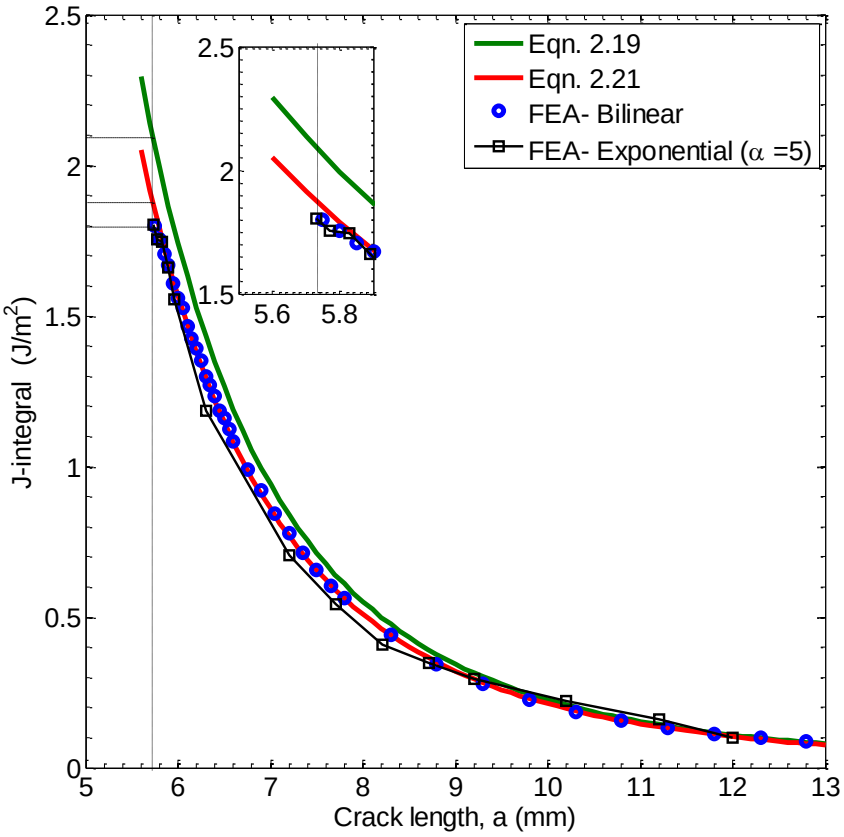

Figure 2.15: J-integral as a function of the crack length, comparing the results from different models. The inset shows the behavior near the fracture toughness $\Gamma = 1.8$ J/m^2.

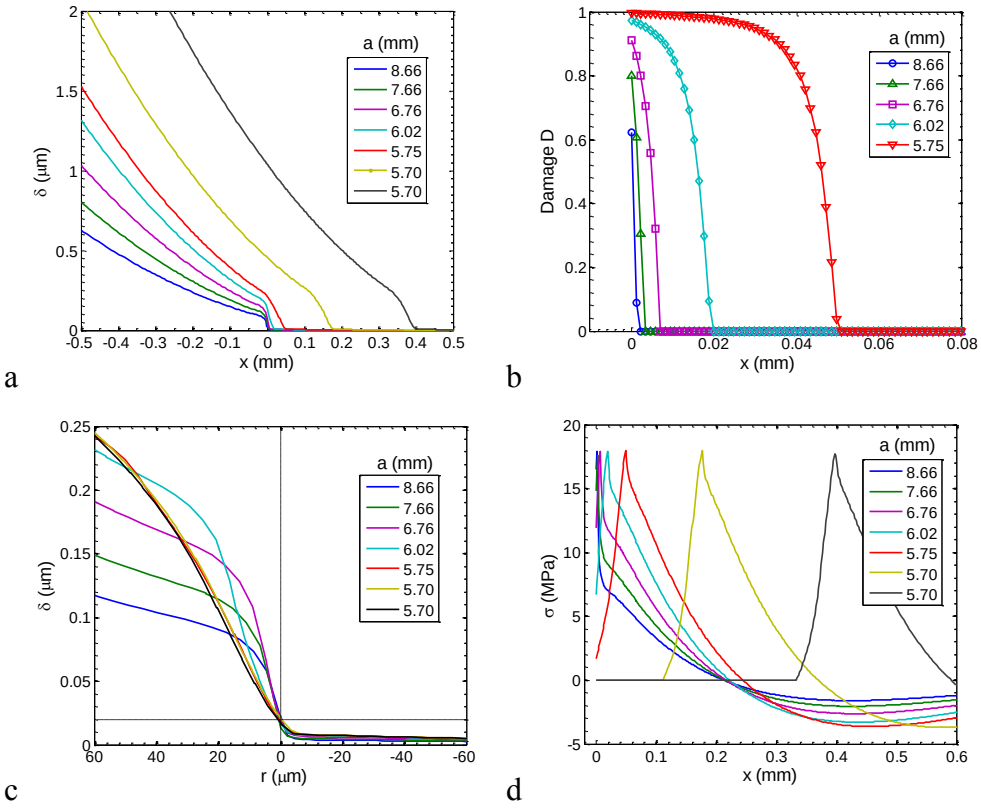

Figure 2.16: Numerical results from a finite element simulation with the cohesive interface model ($\Gamma = 1.8$ J/m^2, $\sigma_0 = 18$ MPa, and $\alpha = 1$): (a) NCOD, (b) Damage evolution, (c) NCOD near the crack tip, and (d) normal traction along the interface.

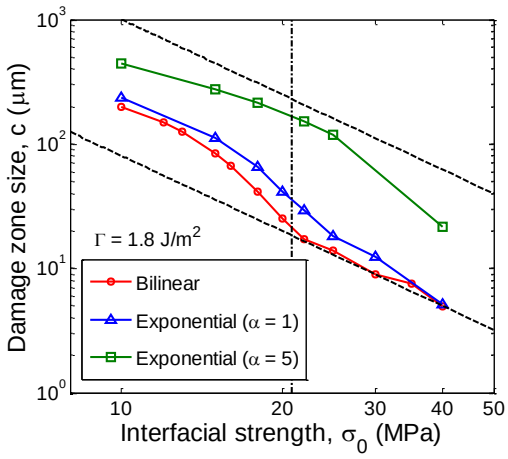

(a)

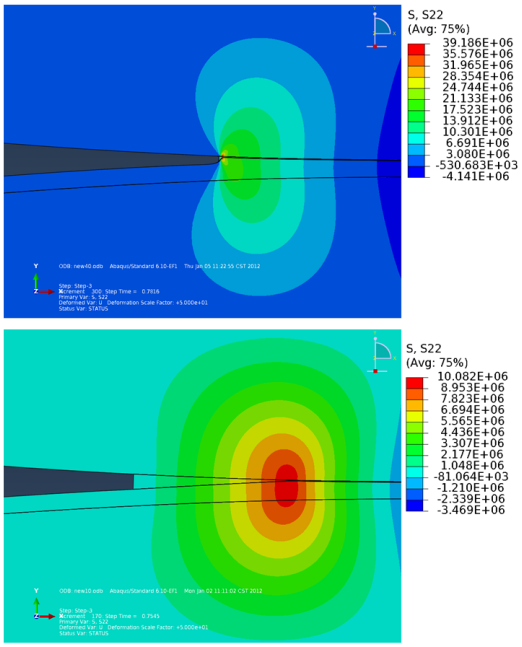

(b)

Figure 2.17: (a) Steady-state damage zone size as a function of interfacial strength. (b) Stress distribution near the crack tip for small-scale bridging ($\sigma_0 = 40$ MPa and $c = 21.7$ μm) and large-scale bridging ($\sigma_0 = 10$ MPa and $c = 439.2$ μm)

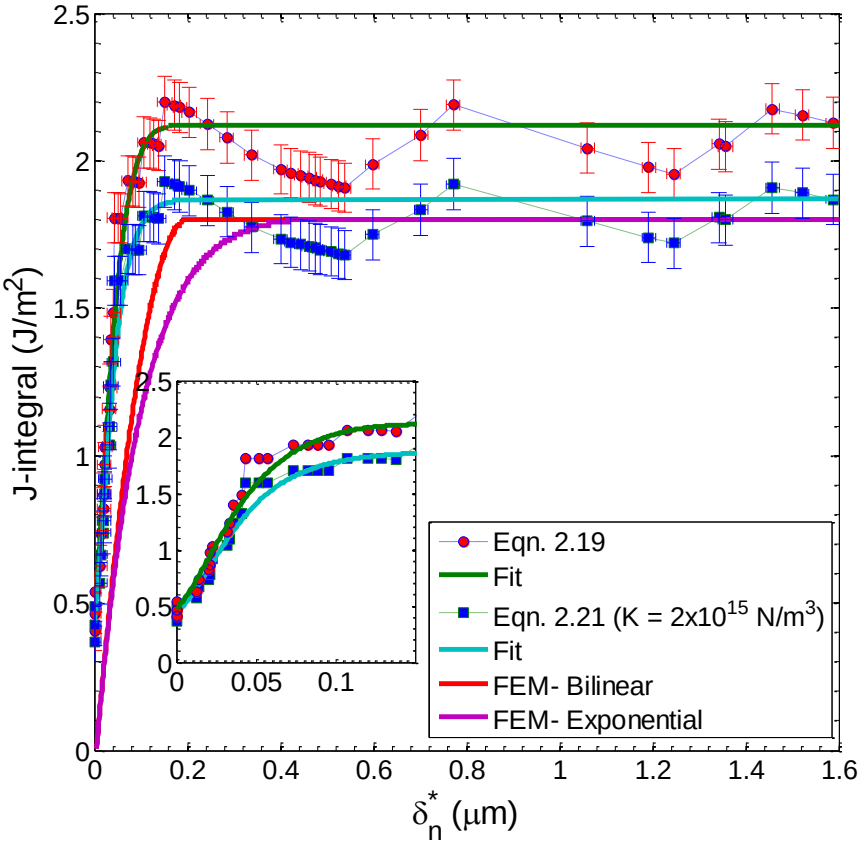

Figure 2.18: J-integral as a function of the normal opening displacement at the initial crack tip.

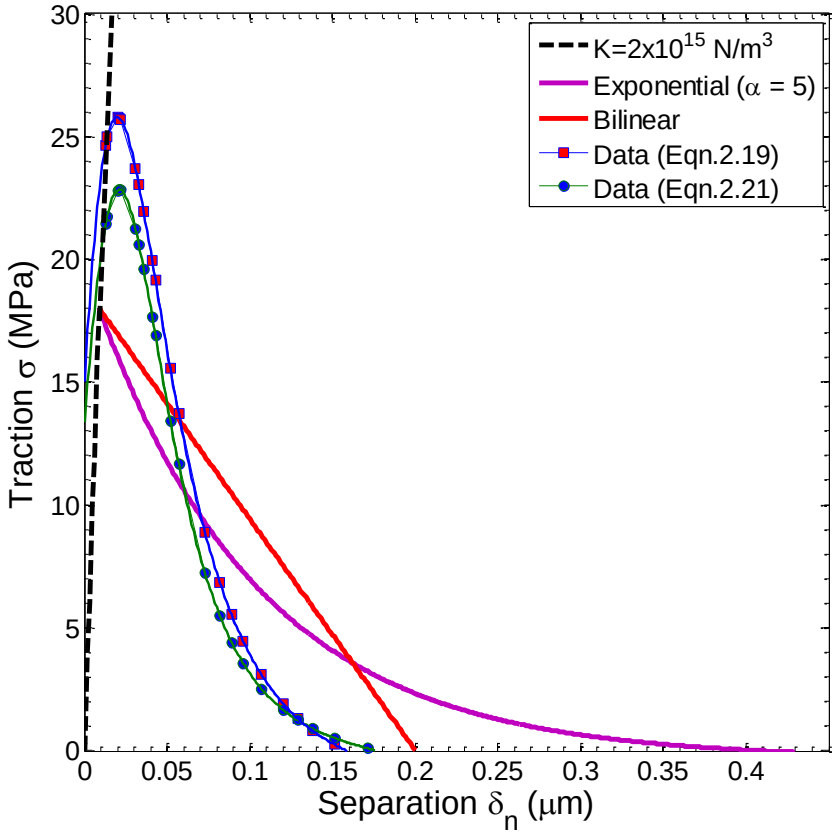

Figure 2.19: Traction-separation relations obtained from the direct method, in comparison with the bilinear and exponential softening models used in the iterative method.

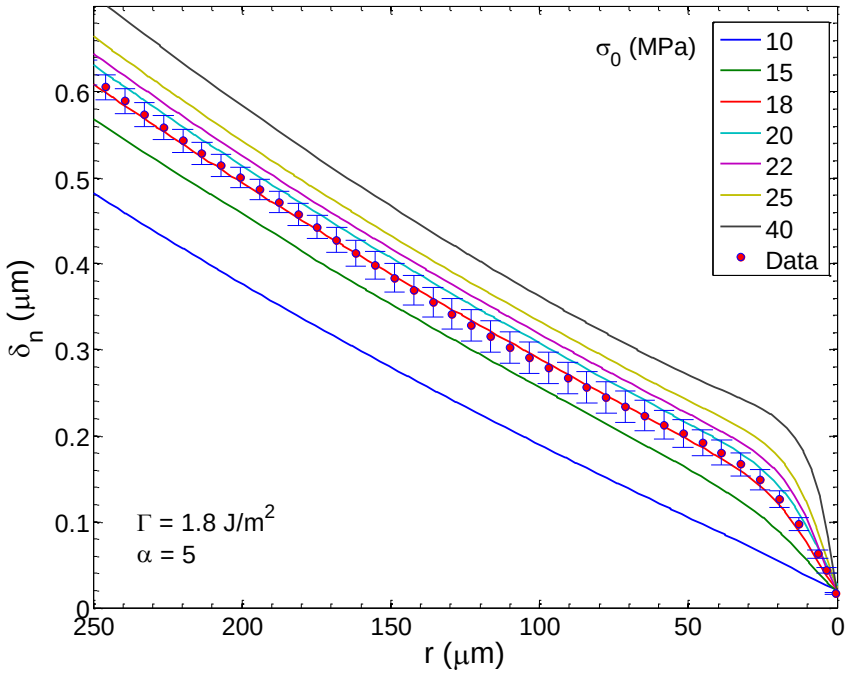

Figure 2.20: Effect of interfacial strength on steady state NCOD, in comparison with the experimental data. The value of σ_0 that provided best fit to the data was 18 MPa.

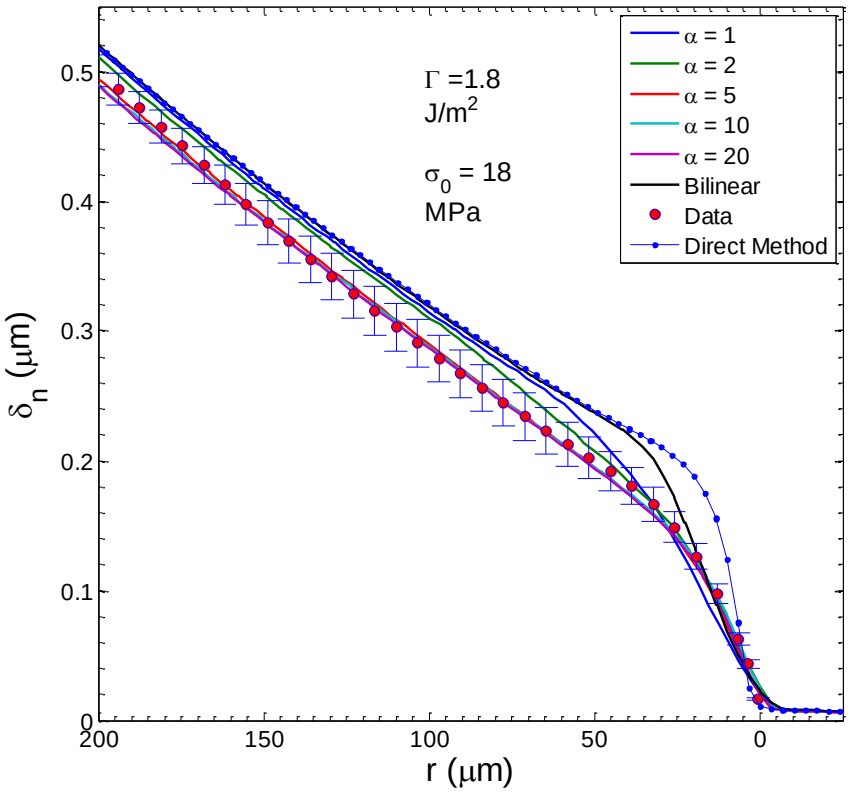

Figure 2.21: Comparison of solutions from the exponential, bilinear and directly obtained traction-separation relations. The exponential traction-separation relation with values of $\alpha \geq 5$ provided the best fit.

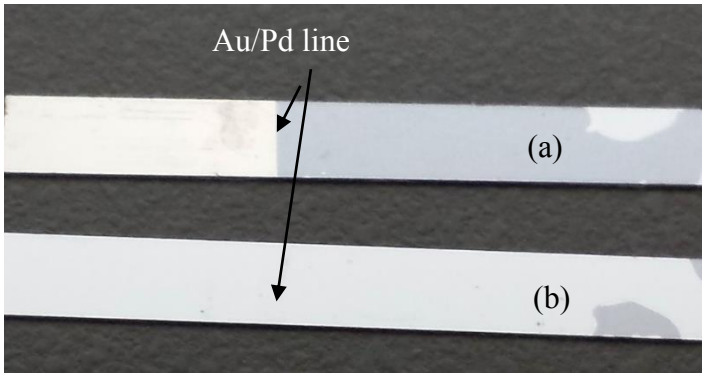

Figure 2.22: Fracture surfaces (a) lower adherend (b) upper adherend

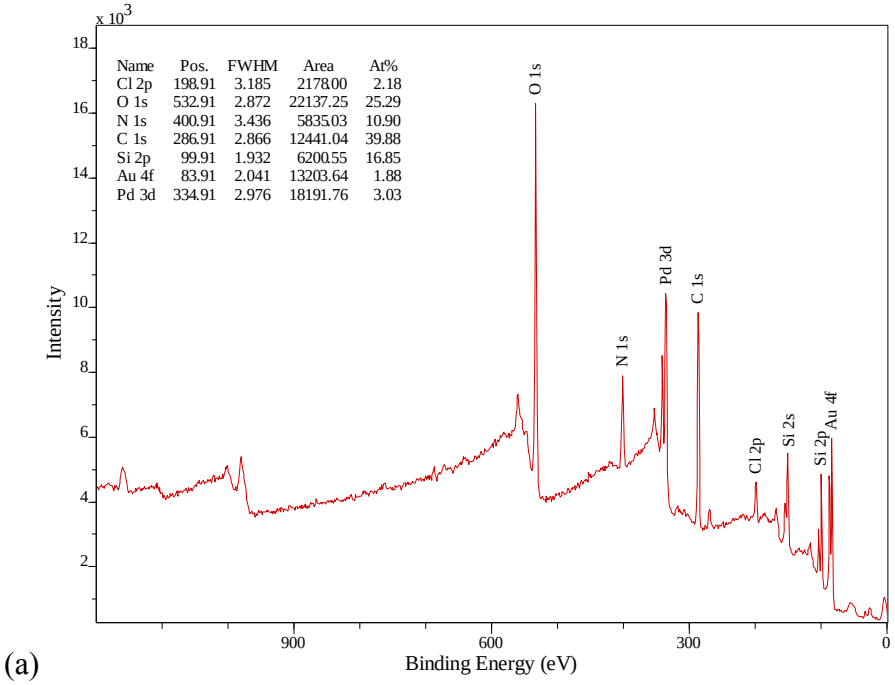

(a)

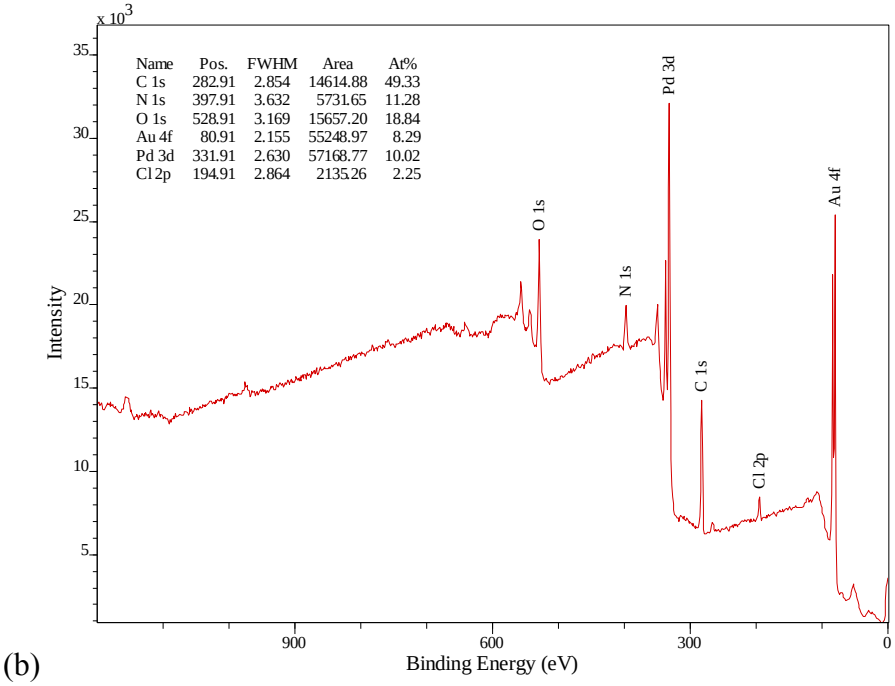

(b)

Figure 2.23: XPS survey of the Au/Pd epoxy interface; (a) upper adherend (b) lower adherend

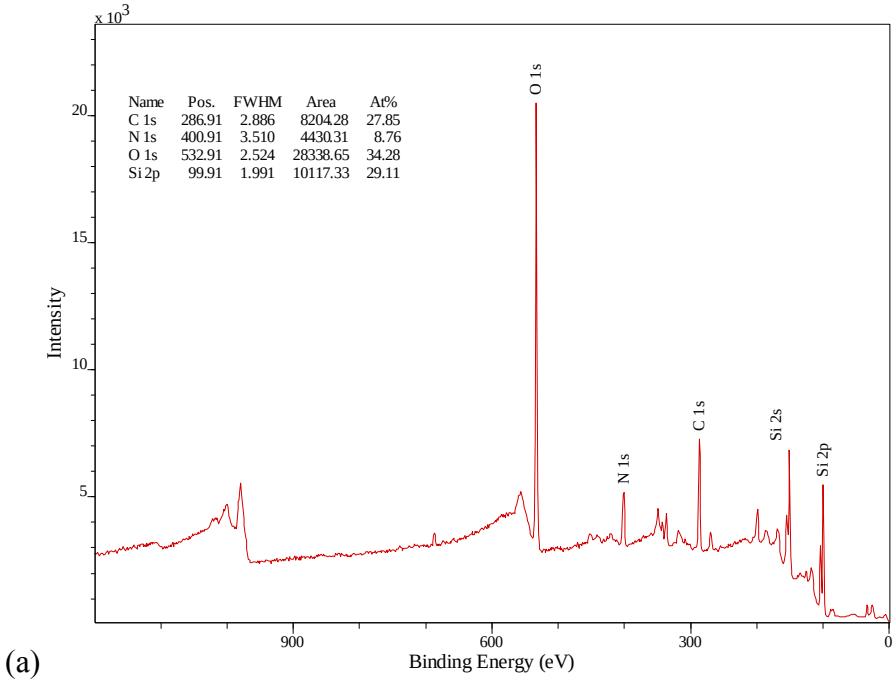

(a)

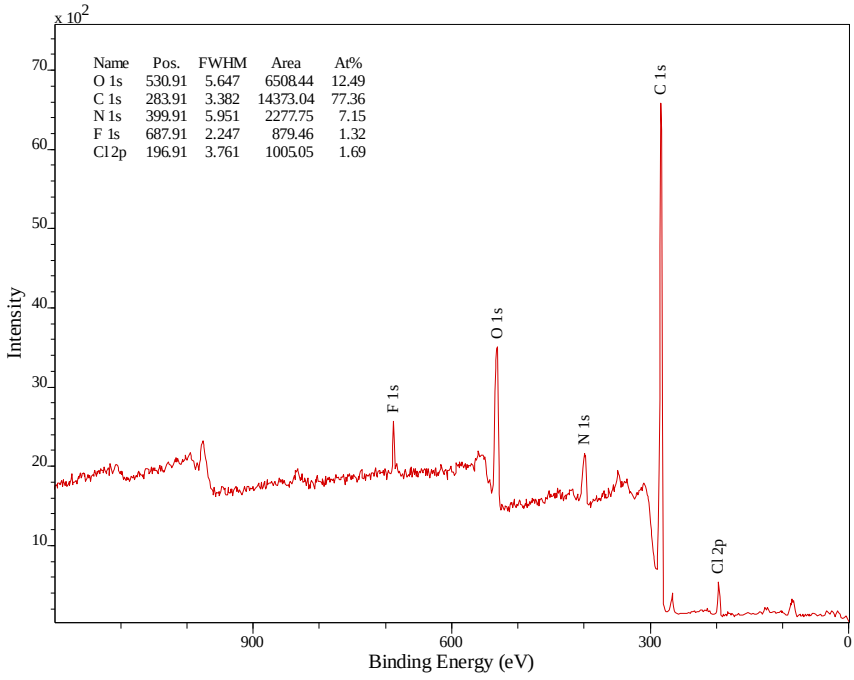

(b)

Figure 2.24: XPS survey of the silicon/epoxy interface region; (a) upper adherend (b) lower adherend

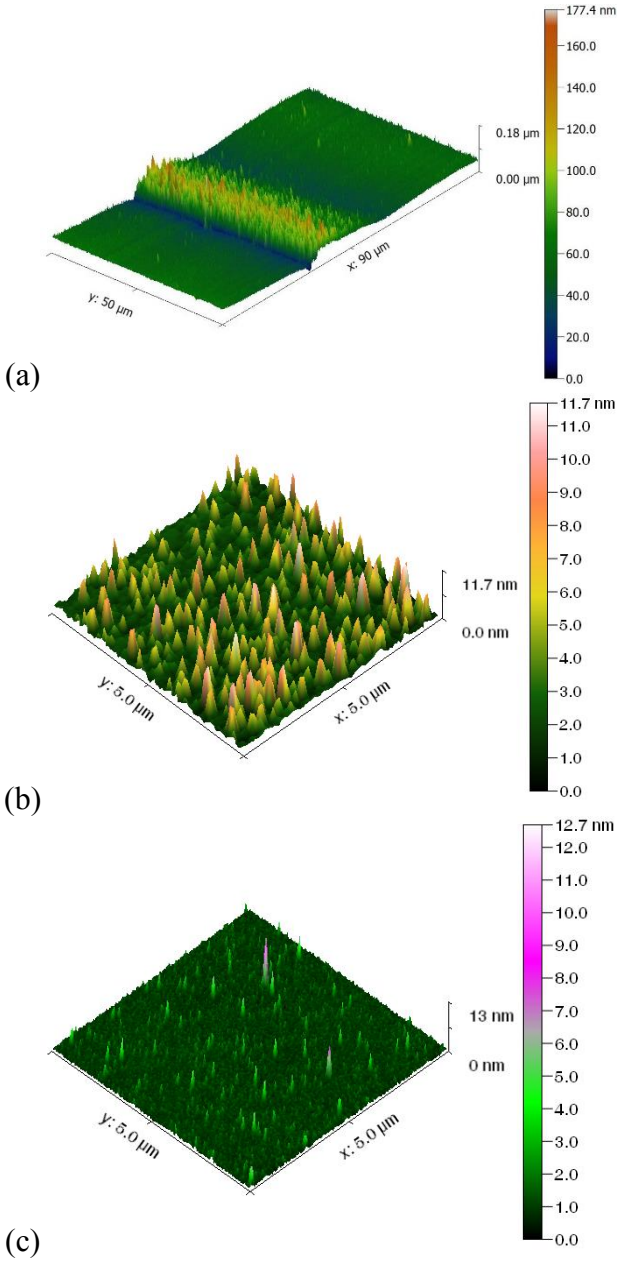

Figure 2.25 AFM images of fracture surfaces: (a) bottom adherend (Au/Pd to Si/epoxy interface transition) (b) bottom adherend (Si/epoxy interface) (RMS roughness: 1.36 nm) and (c) top adherend (Si/epoxy interface) (RMS roughness: 0.85 nm).

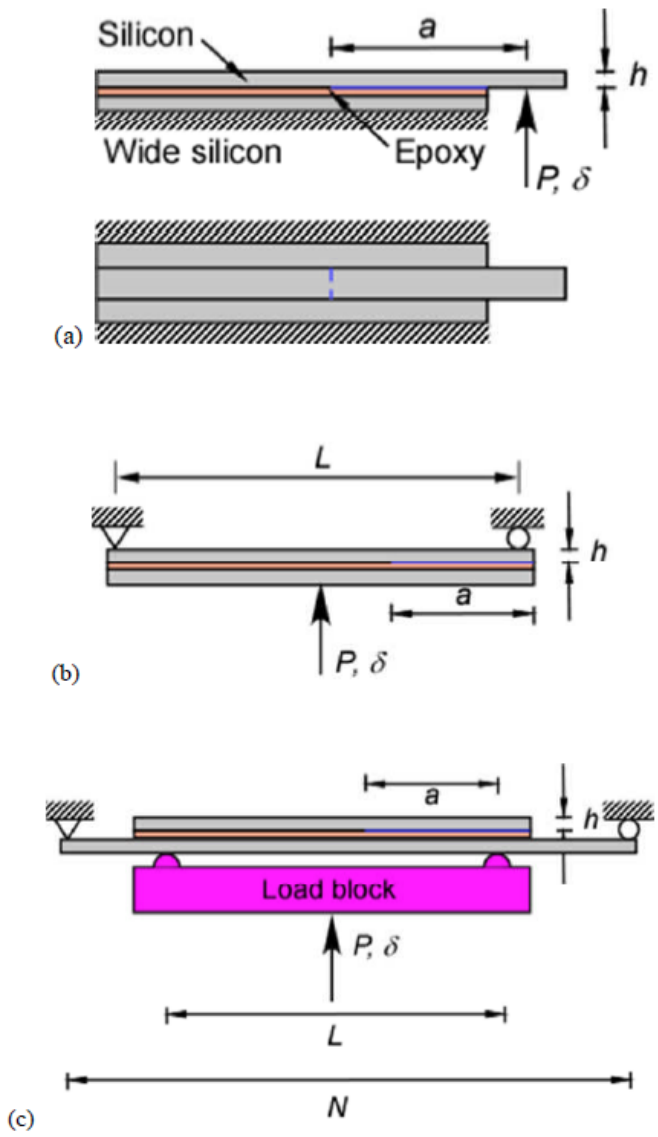

Figure 3.1: Specimen schematics- (a) ELS (b) ENF and (c) MMF specimens.

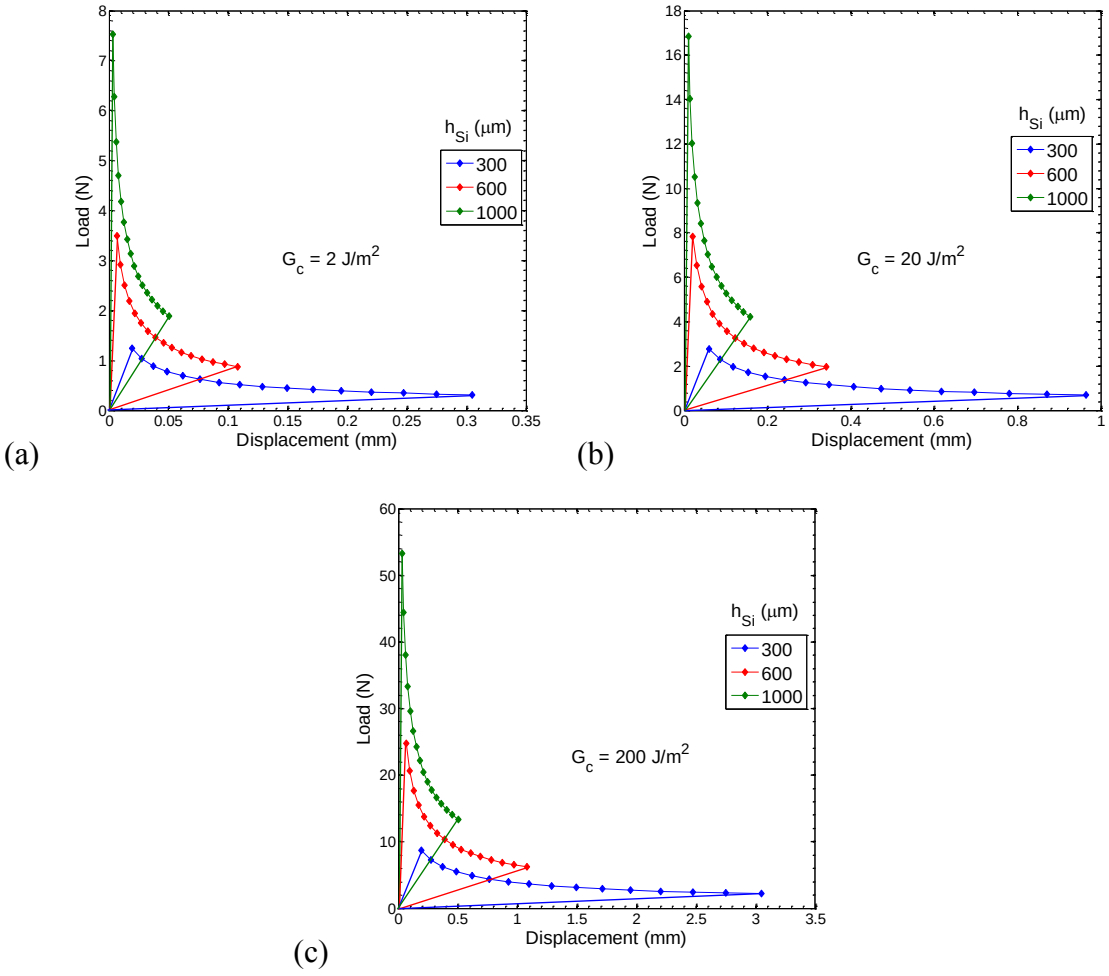

Figure 3.2: Predicted load-displacement responses for a ELS specimen for a range of interfacial toughness values and silicon thicknesses for cracks ranging from 5-20 mm in length.

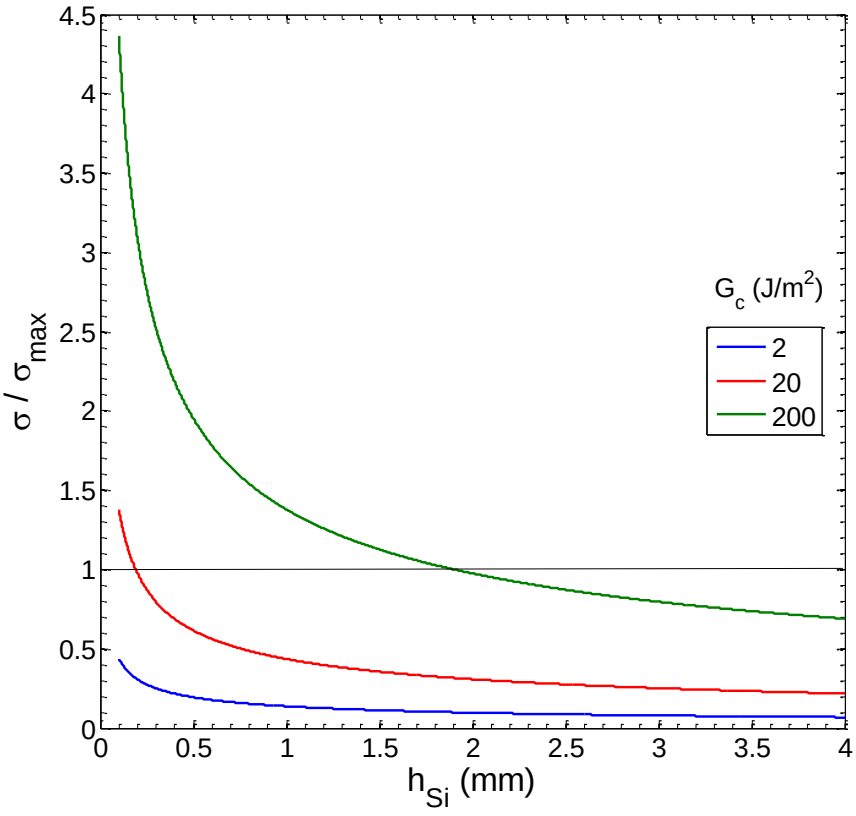

Figure 3.3: The maximum stress level in the silicon strip of the ELS specimen normalized by 230 MPa allowable stress as a function of strip thickness and interfacial toughness.

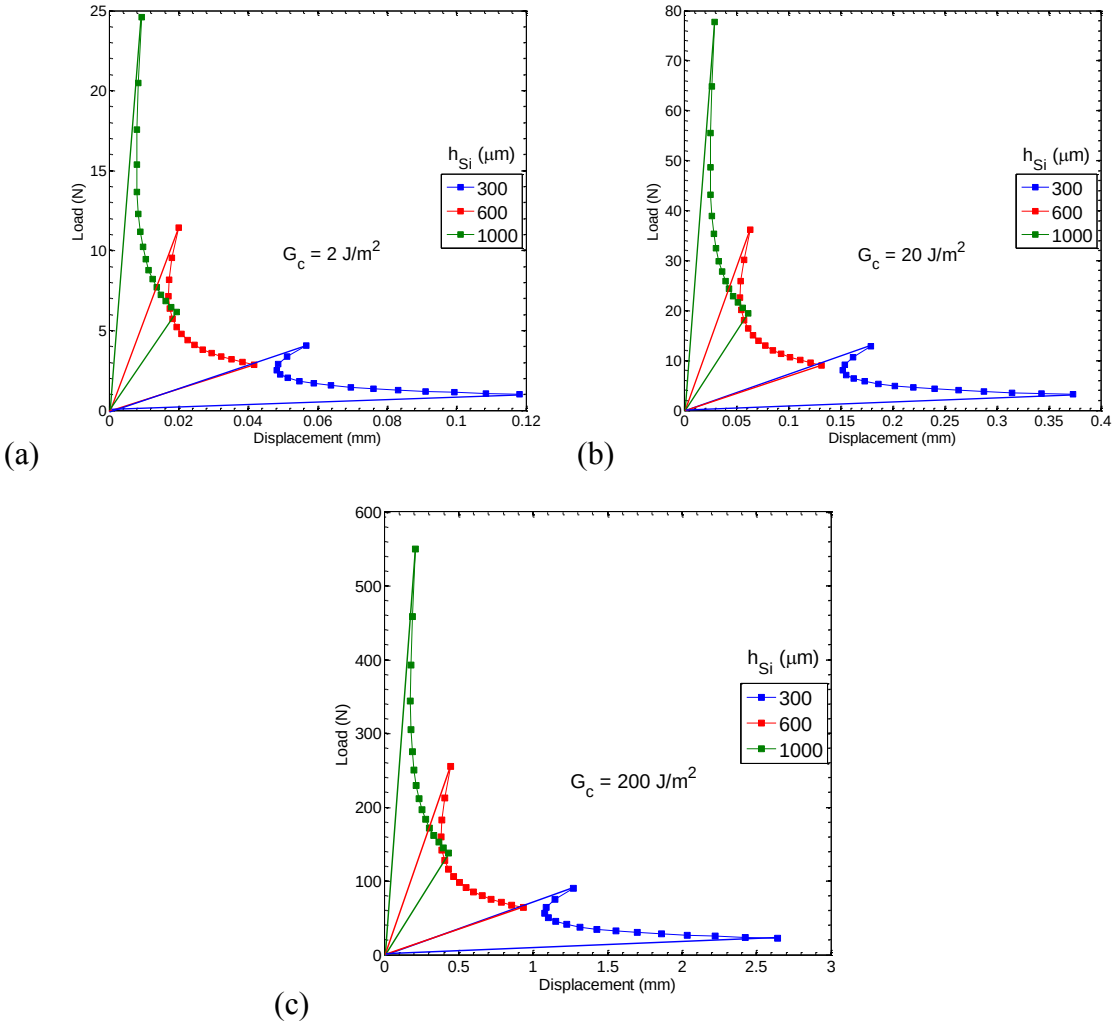

Figure 3.4: Predicted load-displacement responses for a ENF specimen for a range of interfacial toughness values and silicon thicknesses for cracks ranging from 5-20 mm in length.

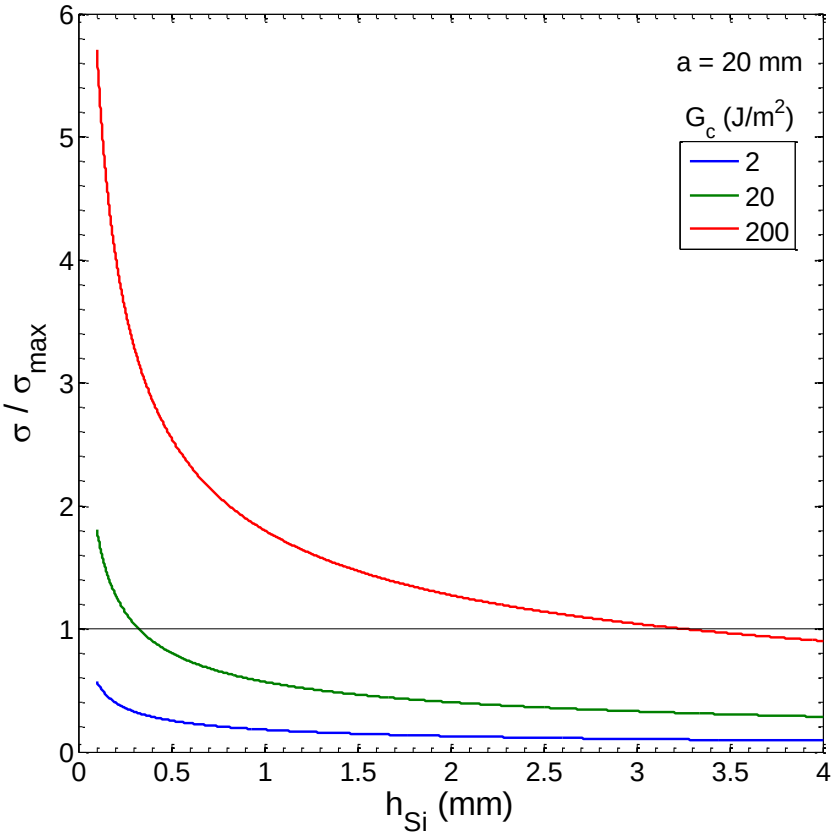

Figure 3.5: The maximum stress level in the silicon strip of the ENF specimen normalized by 230 MPa allowable stress as a function of strip thickness and interfacial toughness.

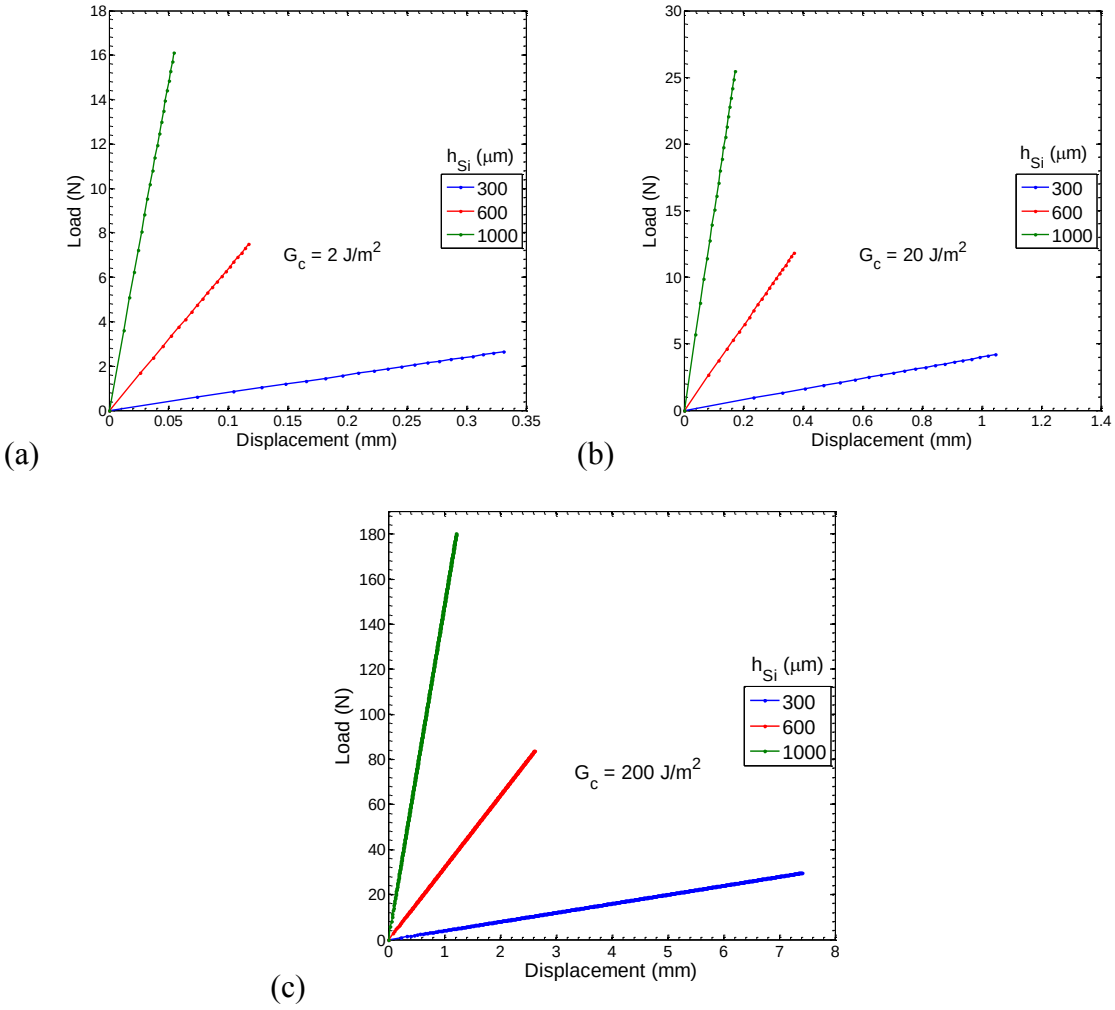

Figure 3.6: Predicted load-displacement responses for a MMF specimen for a range of interfacial toughness values and silicon thicknesses for cracks ranging from 5-20 mm in length.

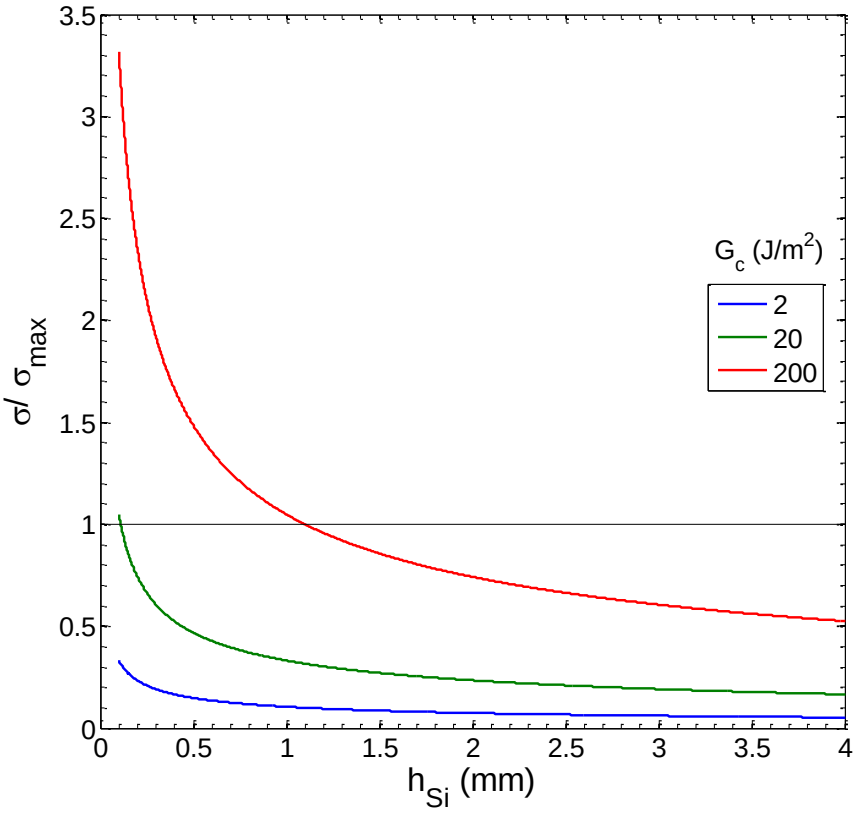

Figure 3.7: The maximum stress level in the silicon strip of the MMF specimen normalized by 230 MPa allowable stress as a function of strip thickness and interfacial toughness.

(a)

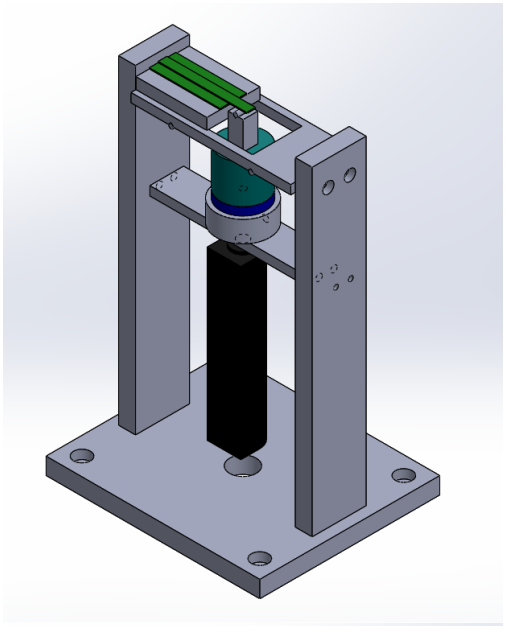

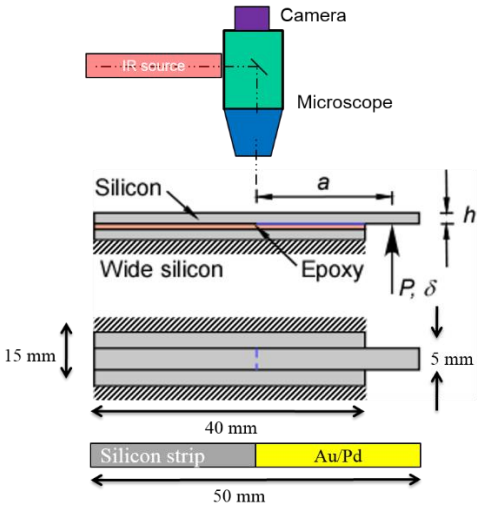

(b)

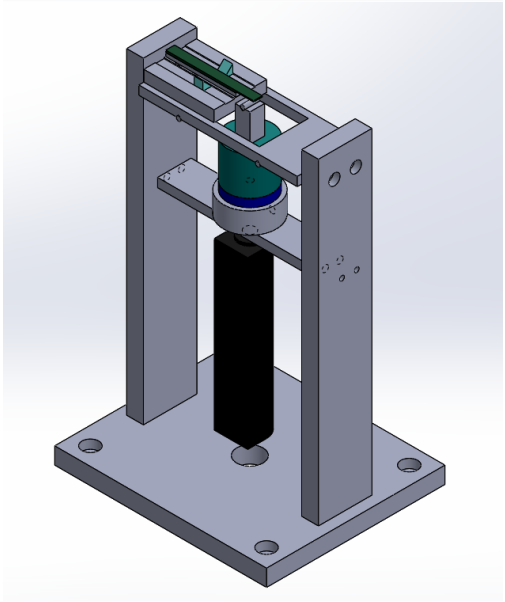

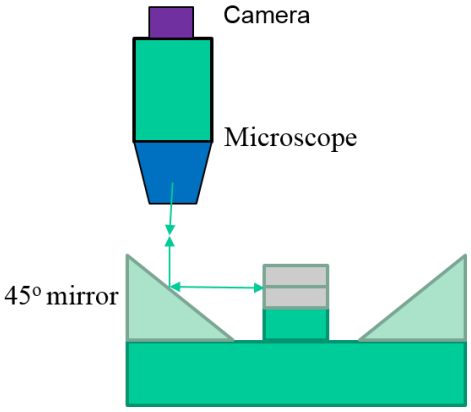

Figure 3.8: Loading device for (a) IR-COI configuration (b) DIC configuration

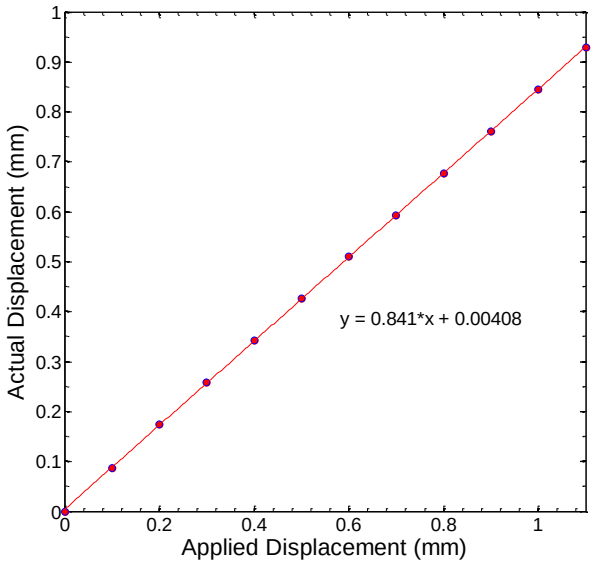

(a)

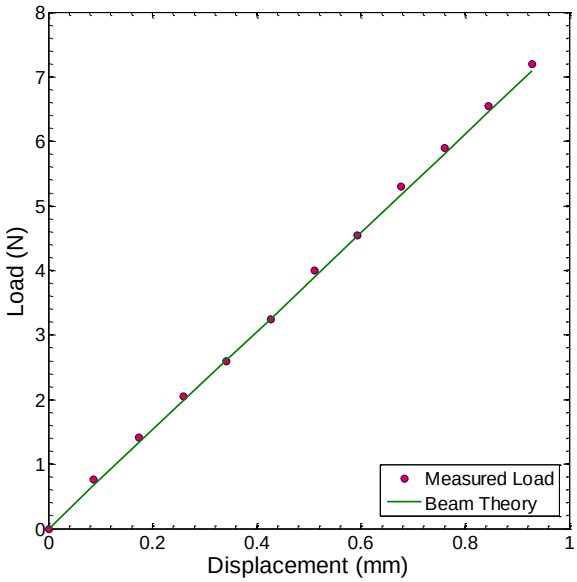

(b)

Figure 3.9: Calibration- (a) actuator calibration using a DVRT (b) load response with respect to calibrated displacement for a cantilever beam

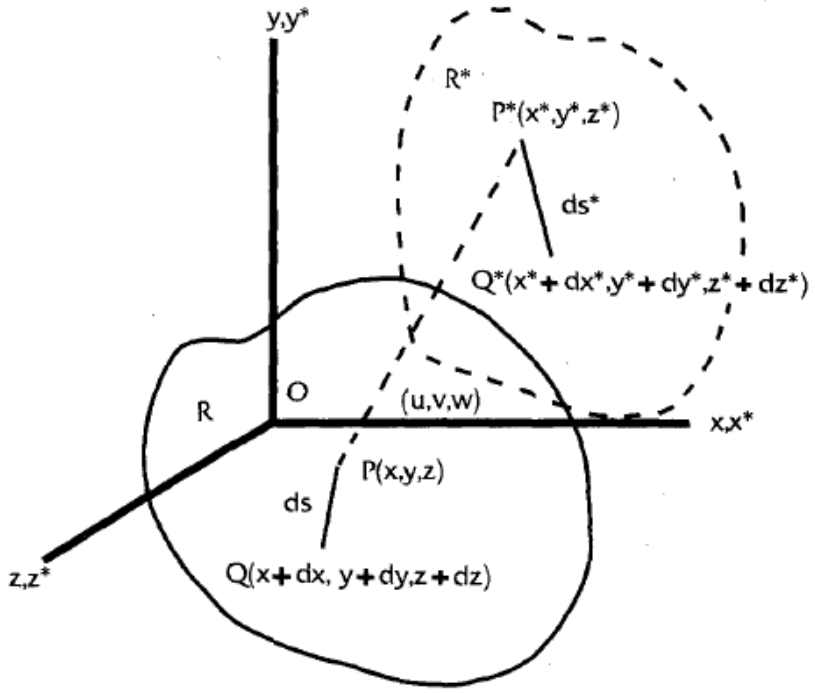

Figure 3.10: Line segments in undeformed and deformed bodies (Chu et al. 1985)

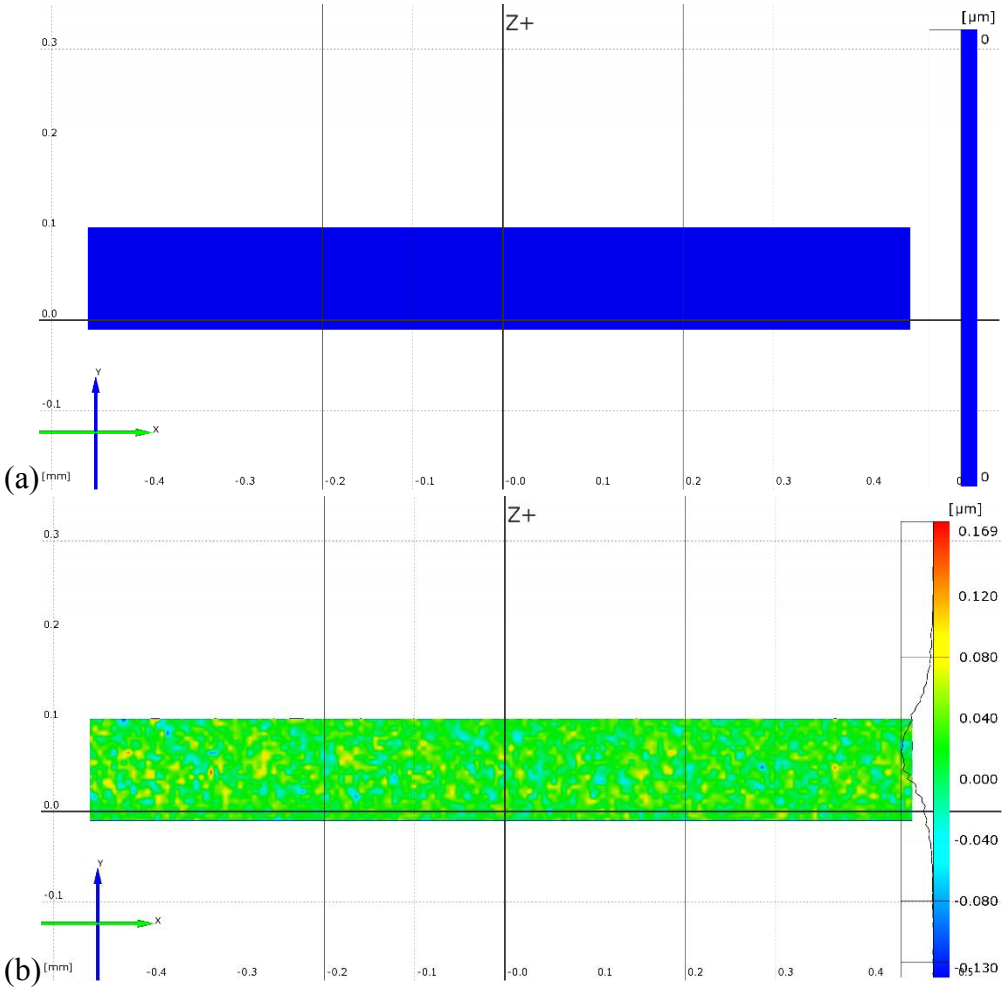

Figure 3.11: Determination of the resolution of the DIC technique (a) reference image (b) subsequent image (no deformation applied). Only the project parameter is displayed here.

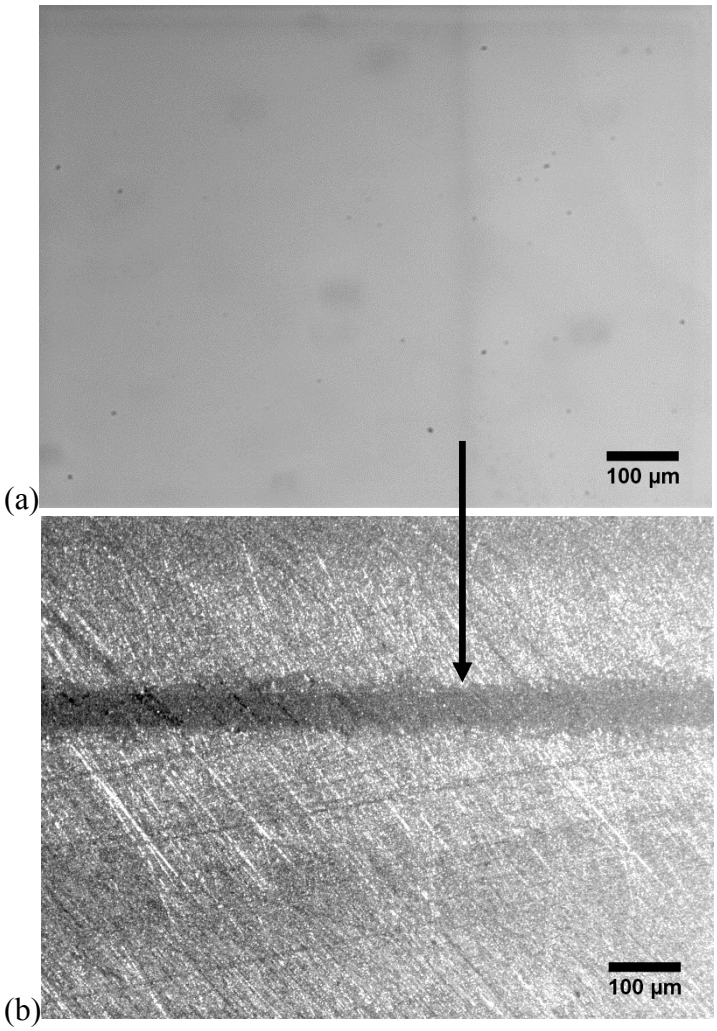

Figure 3.12: Locating crack tip in the DIC experiment (a) interferogram displaying gold line (b) side-view image. The intersection of the gold line axis and the silicon epoxy interface determines the crack tip

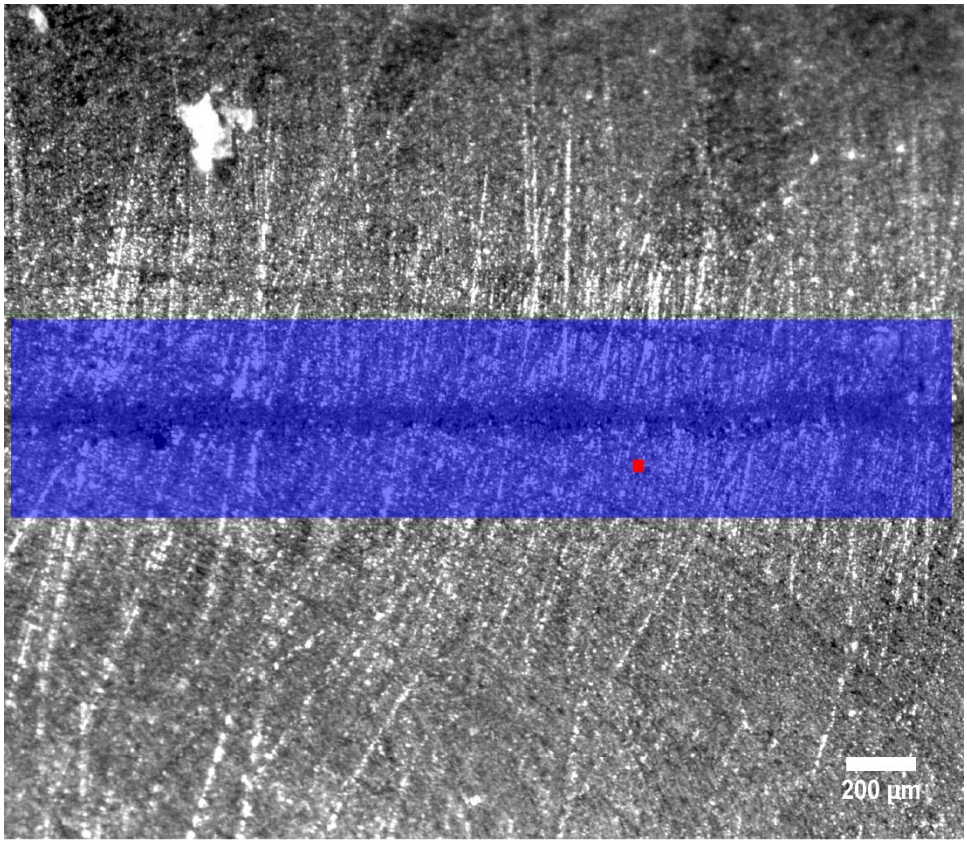

Figure 3.13: A typical DIC experiment image being processed in ARAMIS®. The blue rectangle is the project parameter and the red spot indicates the start point.

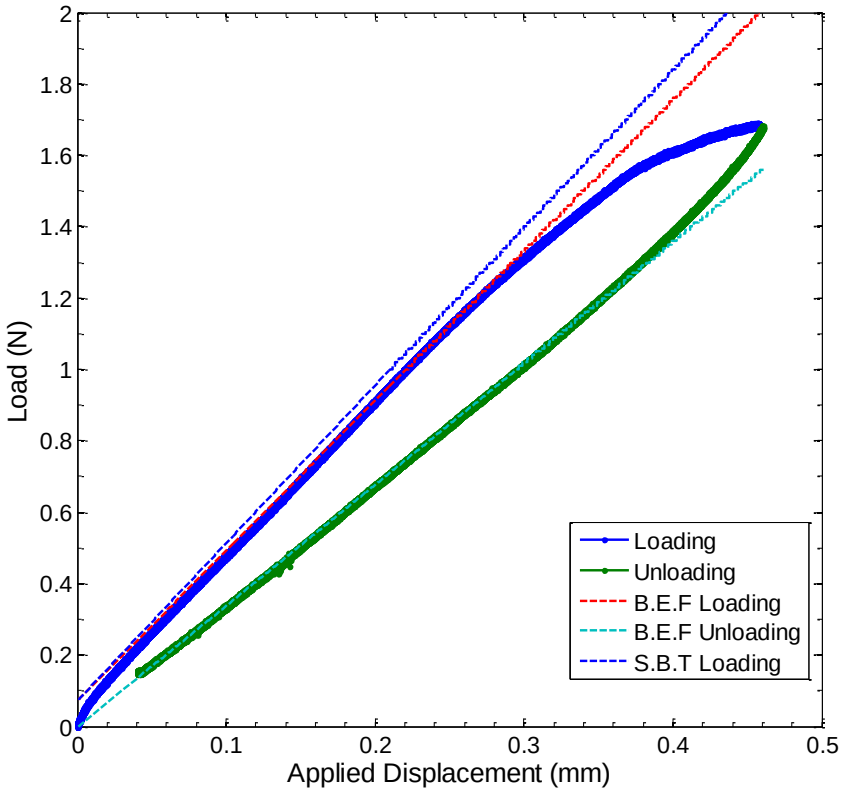

Figure 3.14: A typical load-displacement response from a mixed-mode experiment ($h_{Si} = 584\,\mu\text{m}, h_e = 8\,\mu\text{m}$). The dashed lines indicate the different models considered.

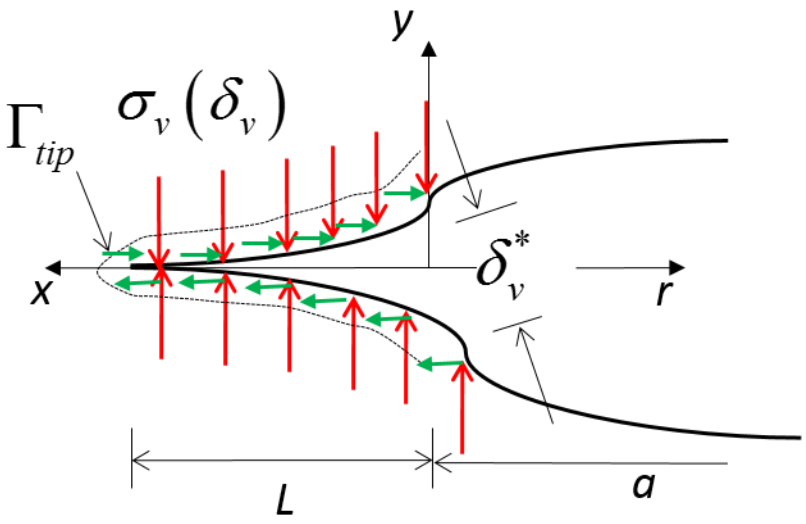

Figure 3.15: A schematic of the crack front geometry and the cohesive zone describing the coordinate system used in the mixed-mode experiment

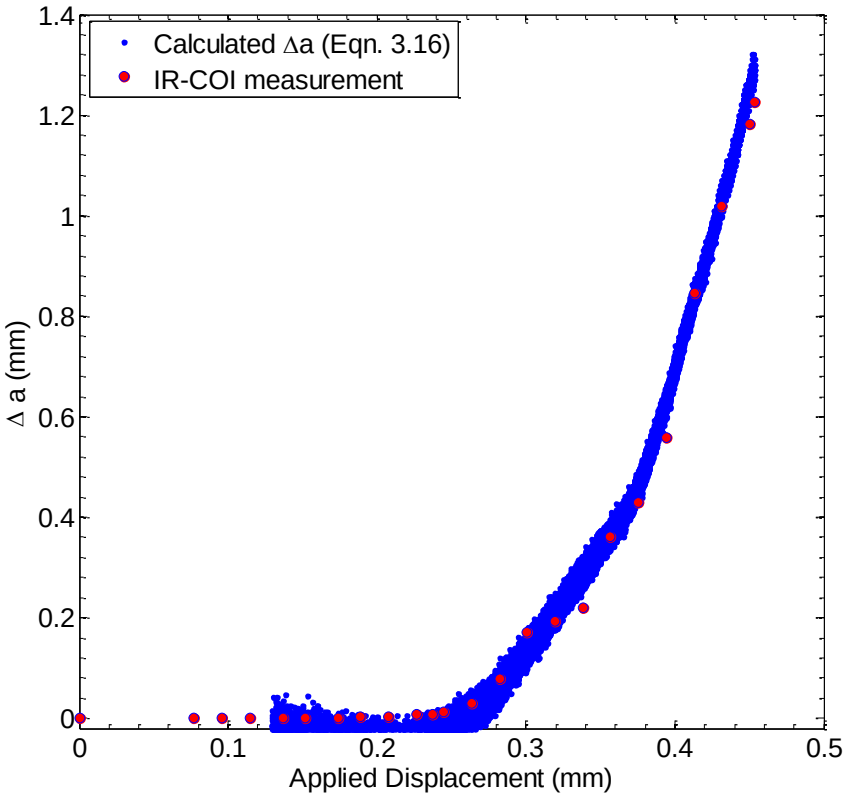

Figure 3.16: Crack length measured by IR-COI as a function of the applied displacement. The a_{eff} value is computed using Eqn. (3.16)and a_0 is the initial crack length measured by IR-COI.

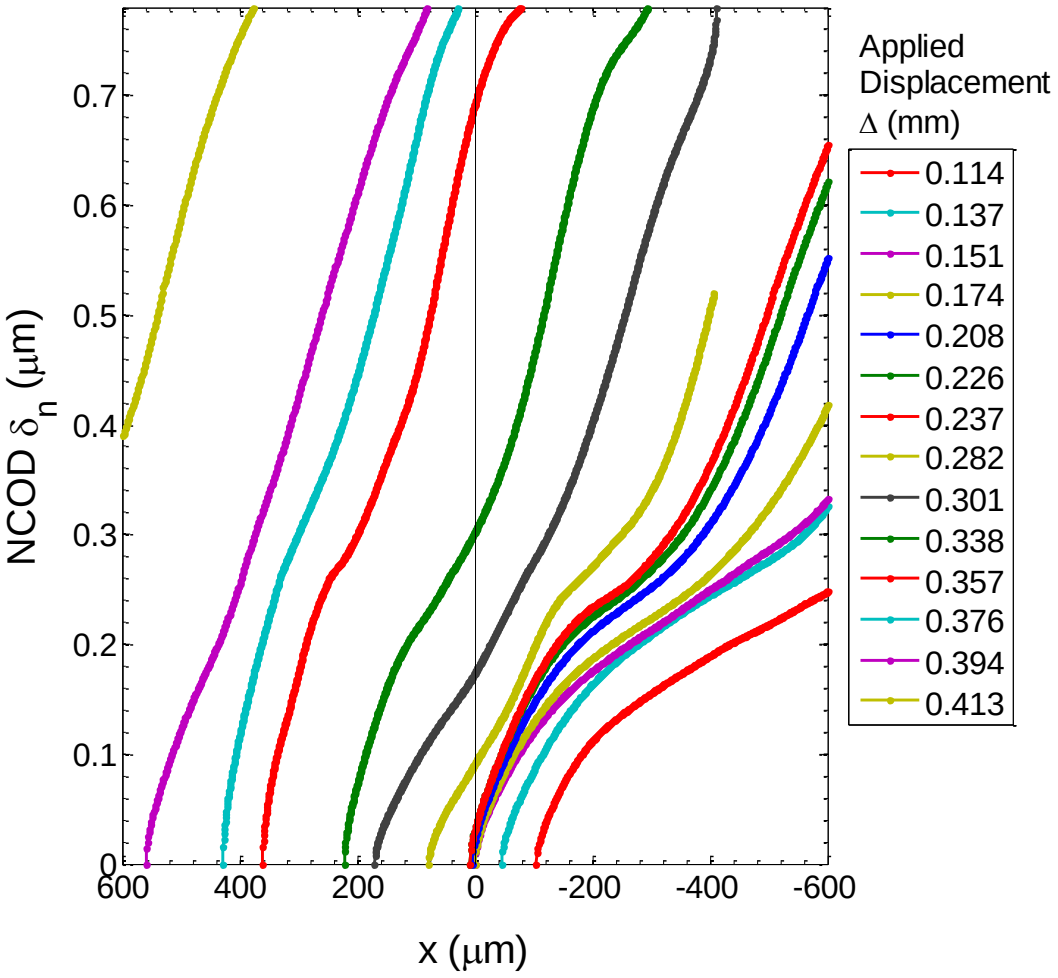

Figure 3.17: A typical set of NCOD profiles plotted as a function of the distance from the initial crack front for the mixed-mode experiment conducted in the IR-COI configuration.

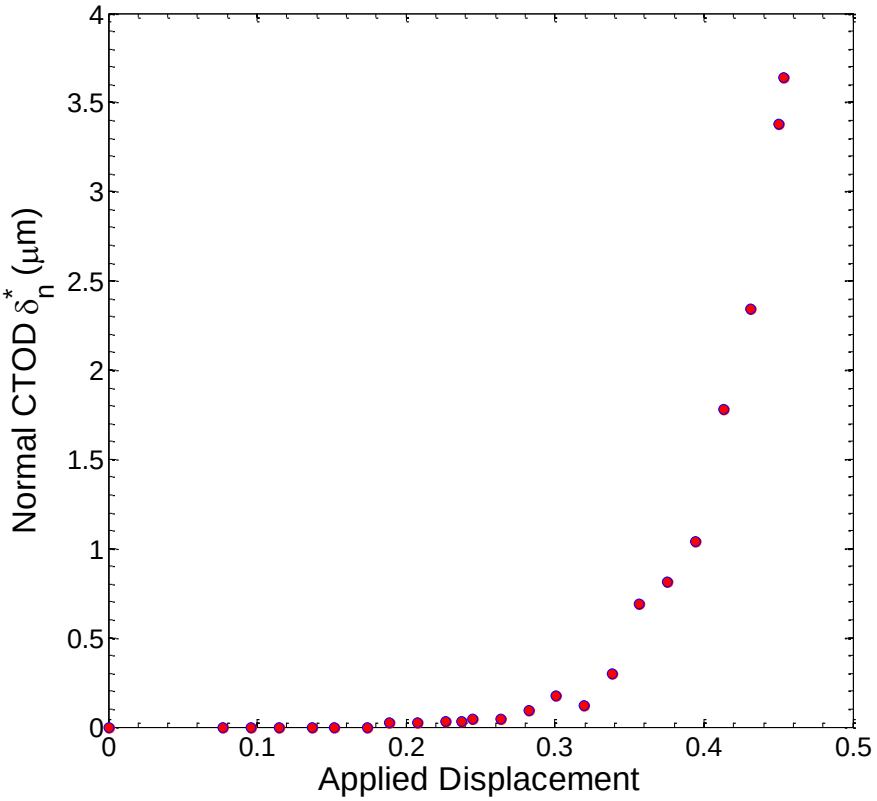

Figure 3.18: Normal CTOD values of obtained by measuring the NCOD at $x = 0$ utilizing the IR-COI technique.

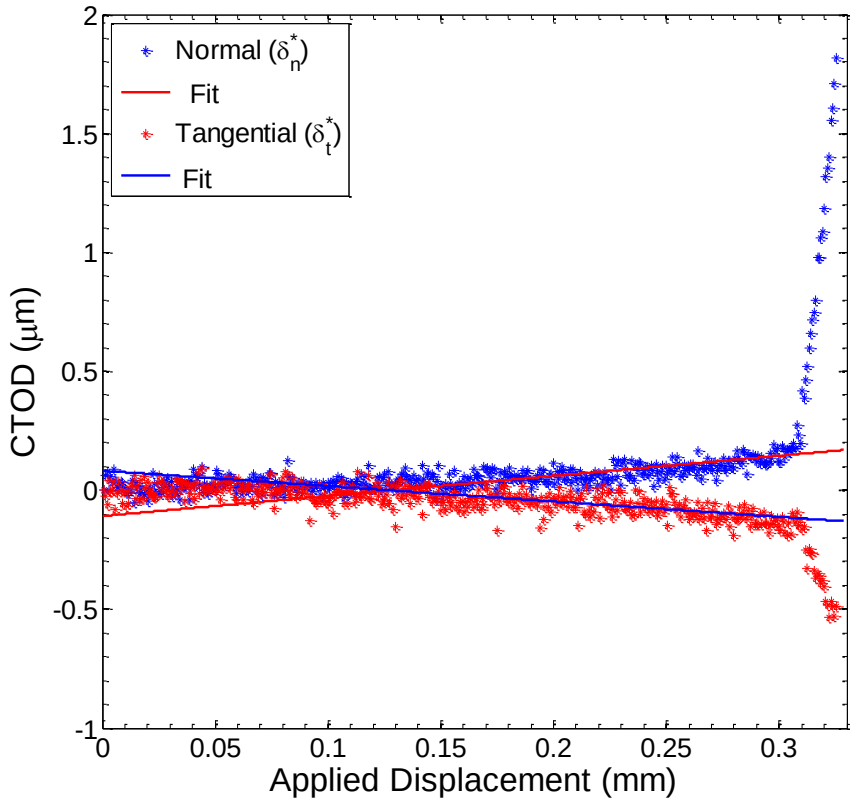

Figure 3.19: Normal and tangential CTOD values as a function of the applied displacement measured by the DIC technique

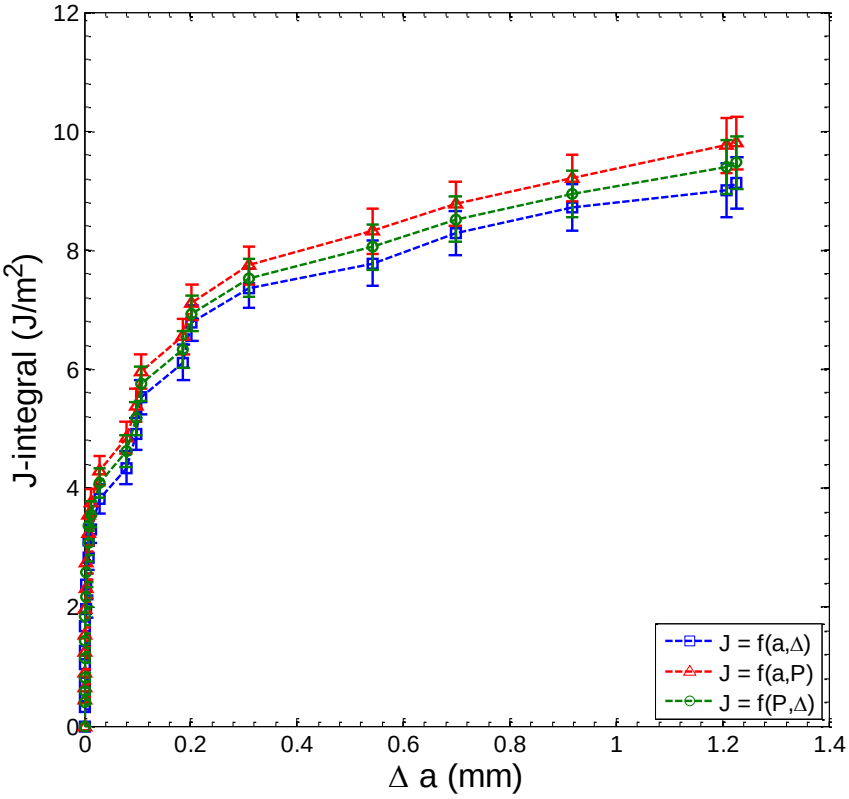

Figure 3.20: Comparison of J-integral formulations with respect to crack growth

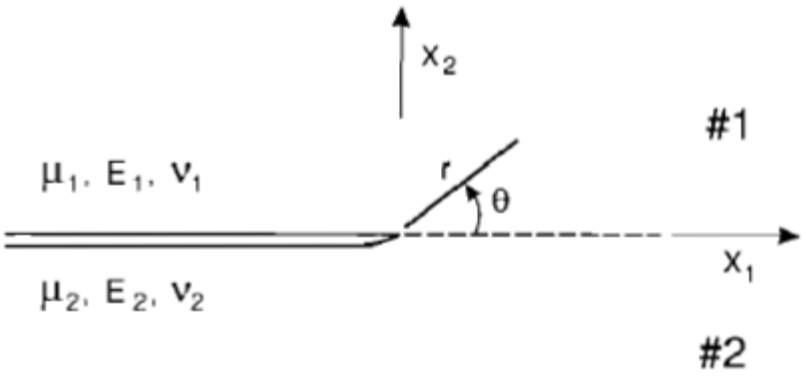

Figure 3.21 Geometry and sign convention for an interface crack (Hutchinson and Suo 1992)

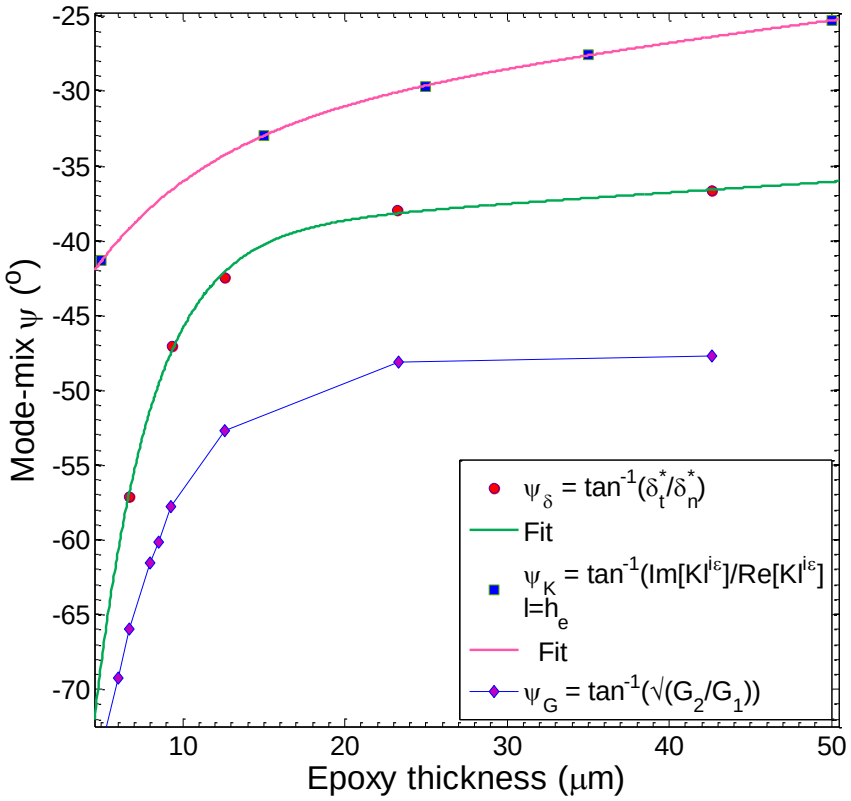

Figure 3.22: Dependence of mode-mix on epoxy thickness.

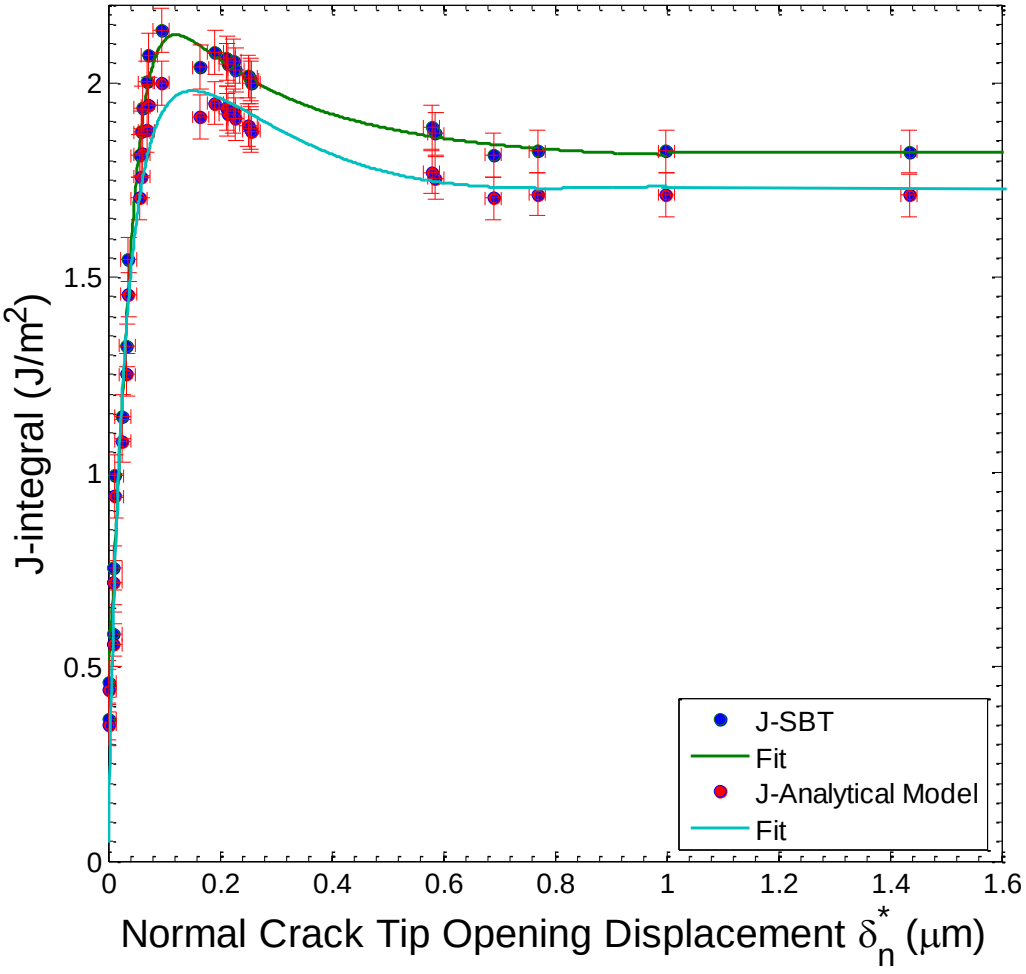

Figure 3.23: Mode-I experiment with the Huntsman epoxy. J-integral vs. normal crack tip opening displacement

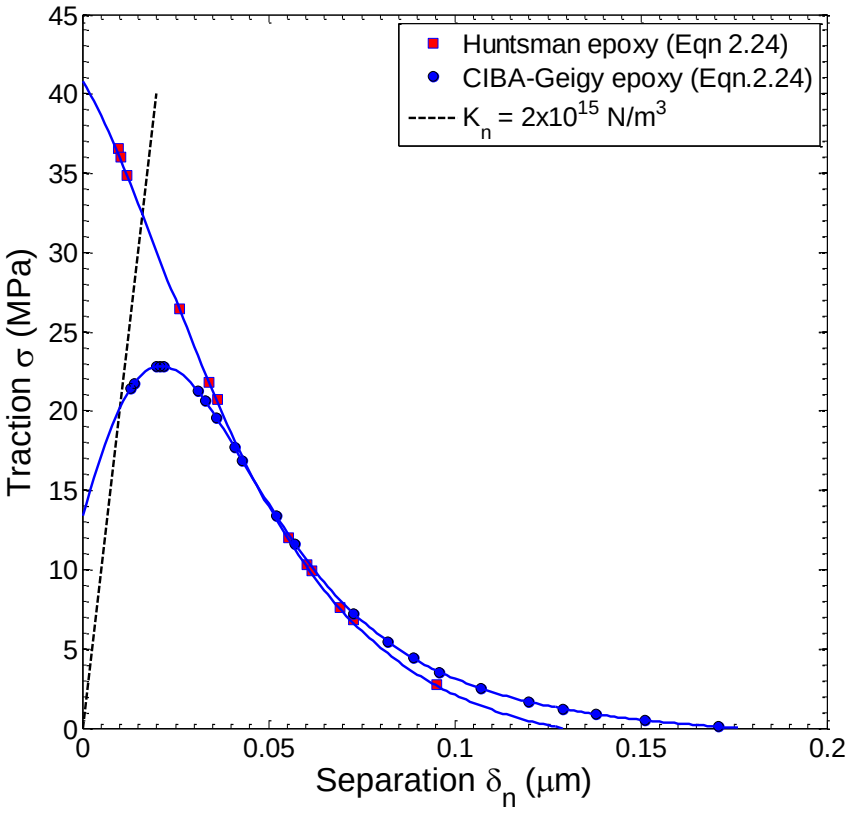

Figure 3.24: Mode-I traction-separation relation for the Huntsman epoxy specimen compared with the traction-separation relation for the CIBA-Geigy specimen.

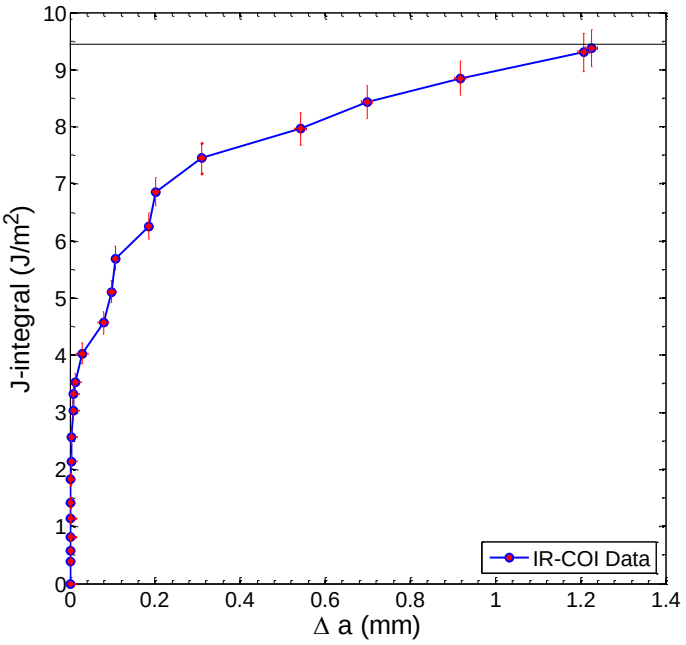

(a)

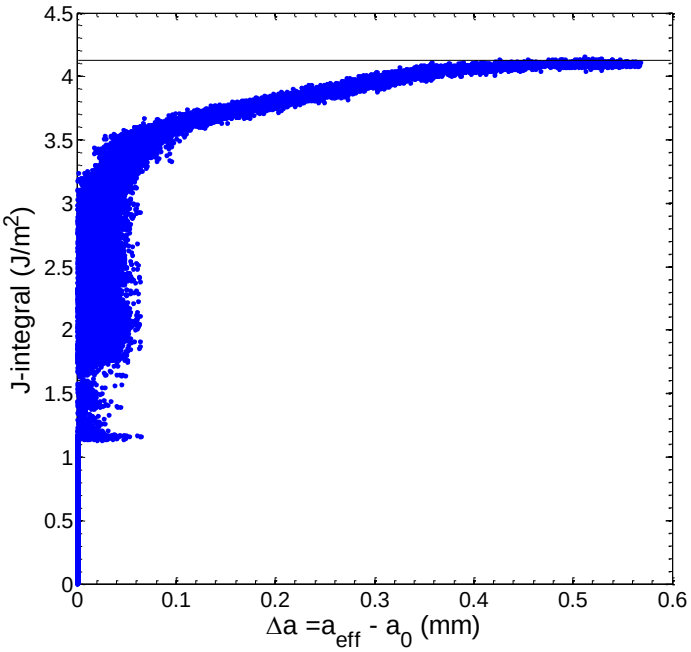

(b)

Figure 3.25: Fracture resistance curves (a) IR-COI data (b) DIC data

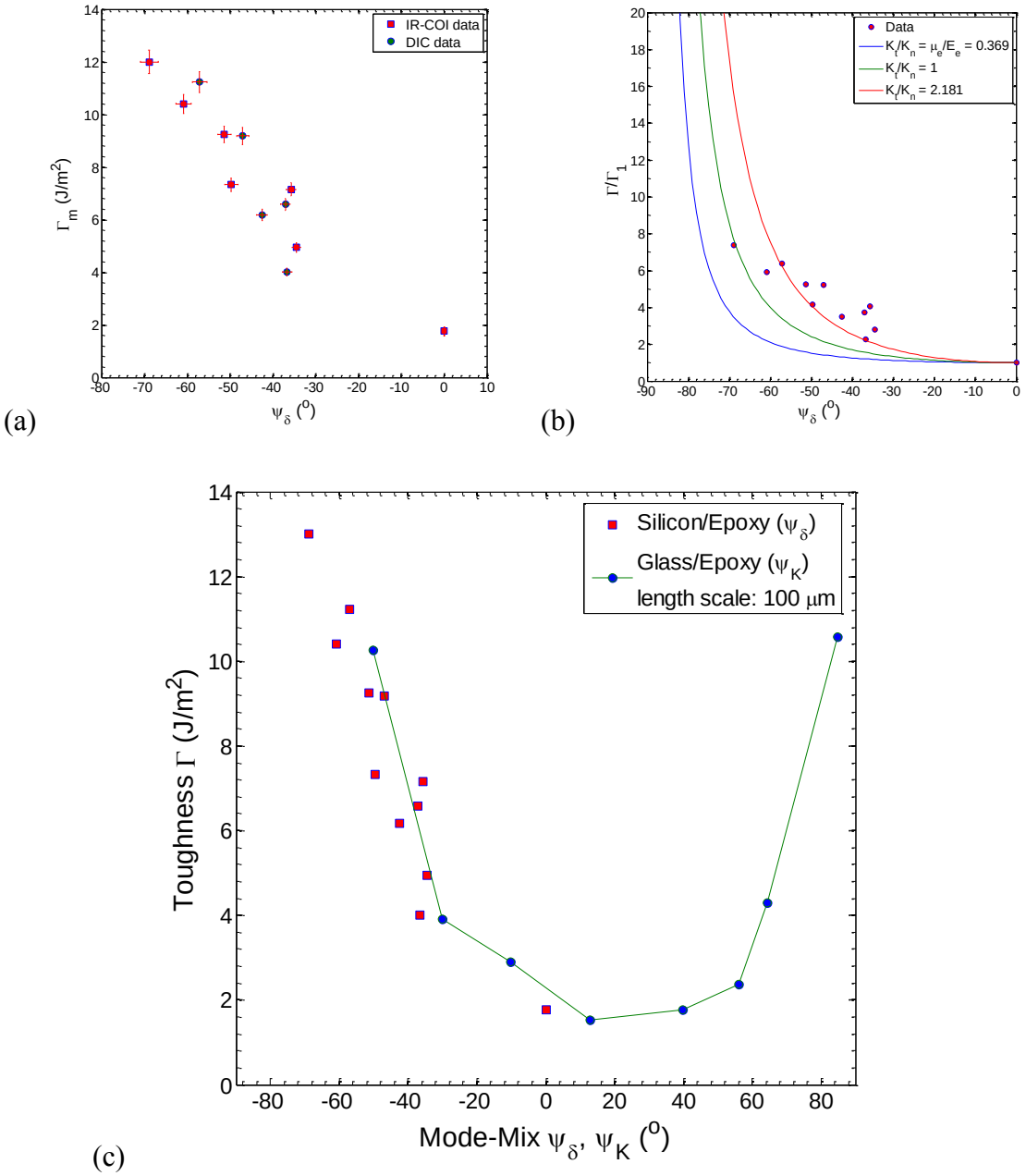

Figure 3.26: Toughness envelope (a) data (b) analytical model fit to normalized data (c) comparison with glass/epoxy interface (Swadener and Liechti 1998).

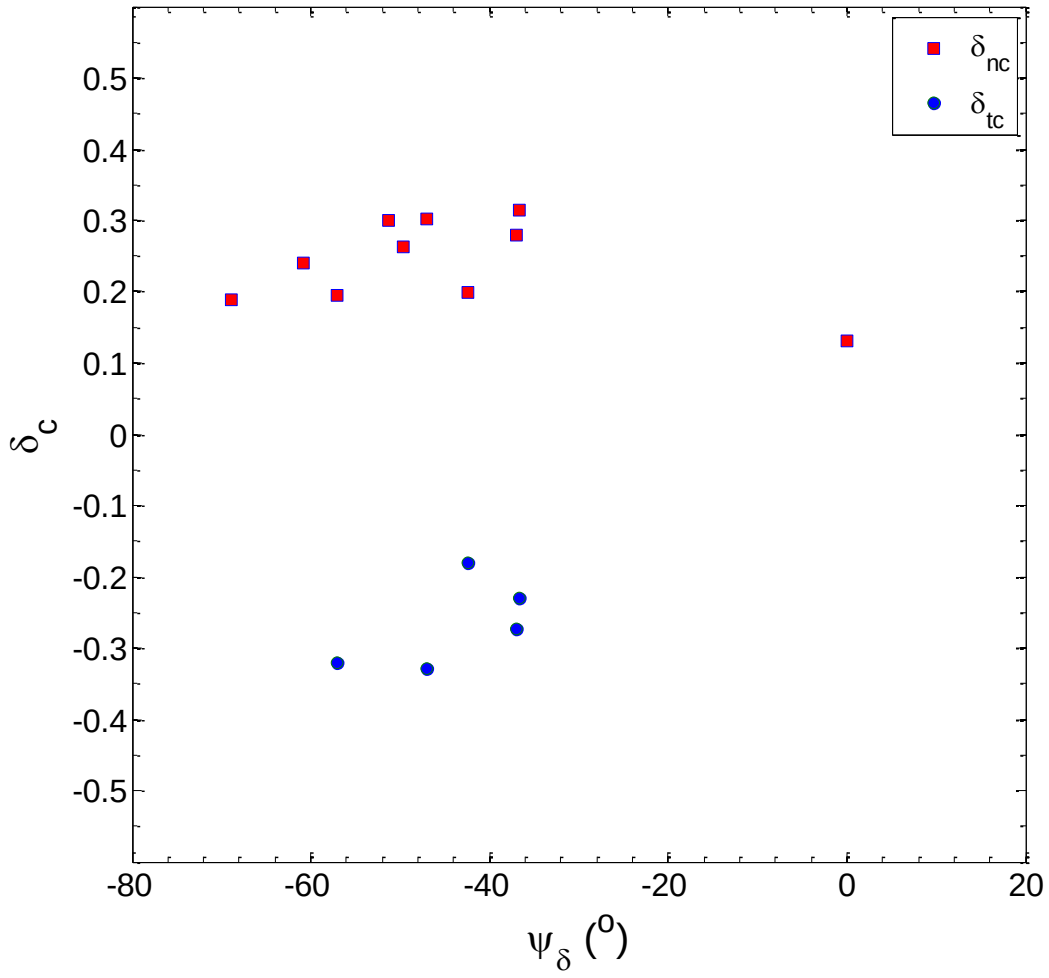

Figure 3.27: Critical CTOD values with respect to mode-mix.

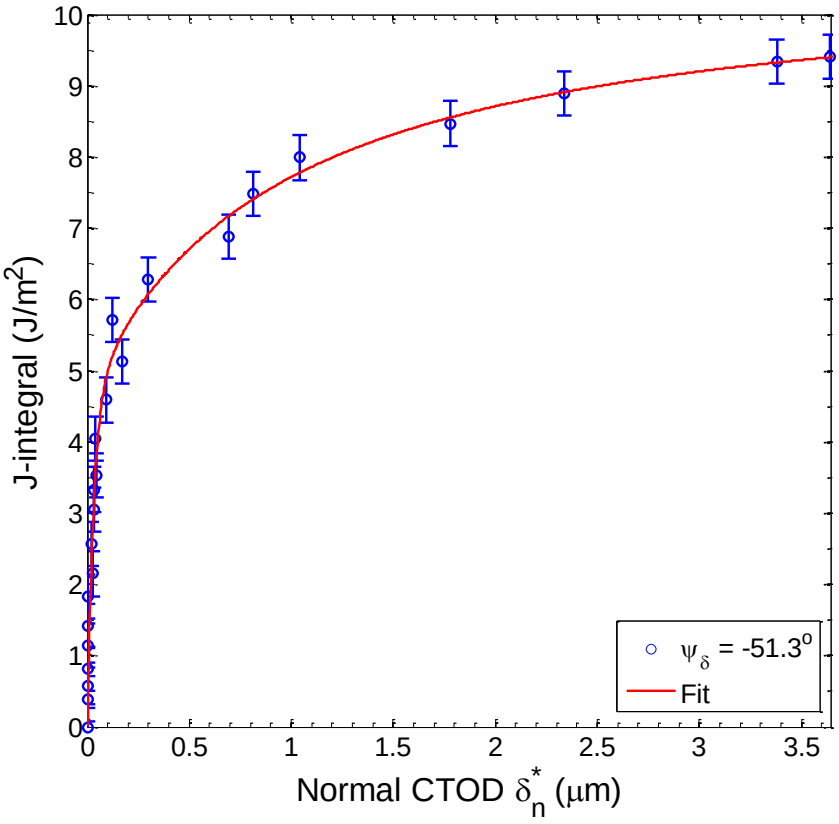

Figure 3.28: J-integral as a function of the normal crack tip opening displacements measured using the IR-COI technique.

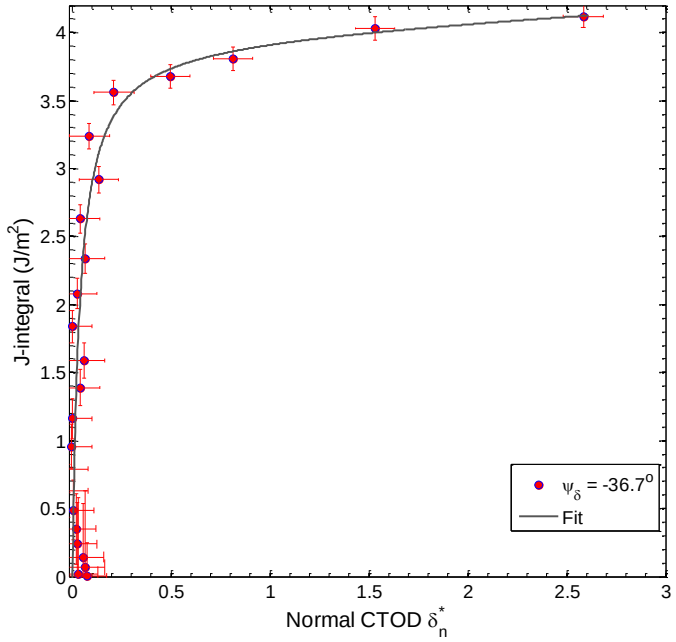

(a)

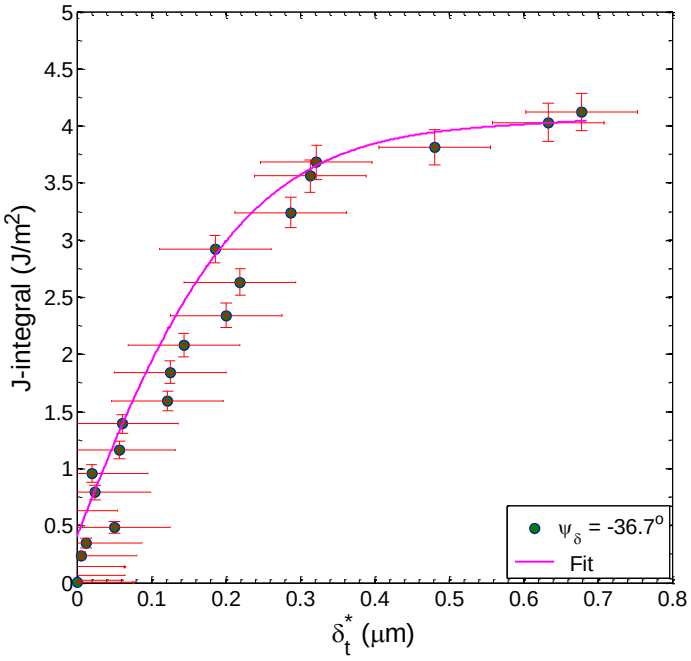

(b)

Figure 3.29: J-integral as a function of (a) the normal crack tip opening displacements and (b) the tangential crack tip opening measured using DIC

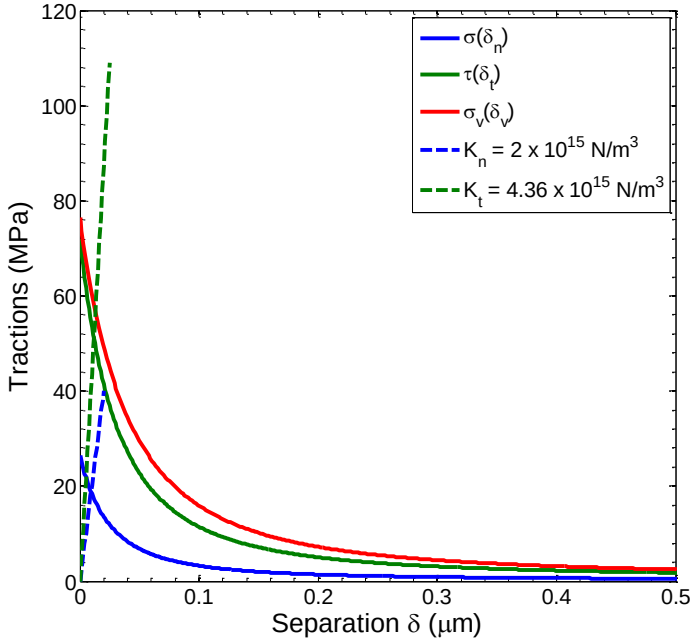

(a)

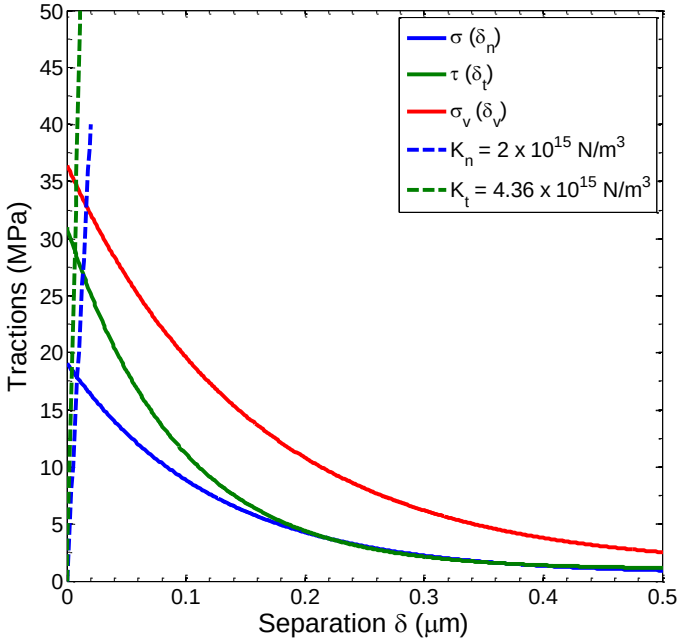

(b)

Figure 3.30: Traction separation relations (a) IR-COI $\psi_\delta = -51.3^\circ$ (b) DIC $\psi_\delta = -36.7^\circ$

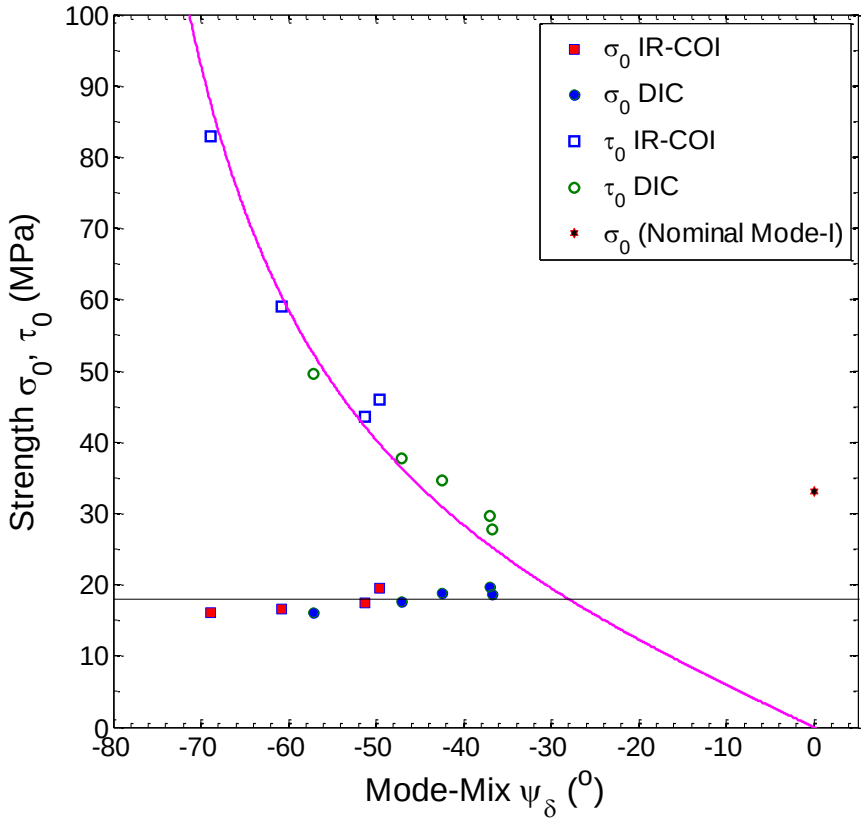

Figure 3.31: Mode dependence of normal and shear strengths

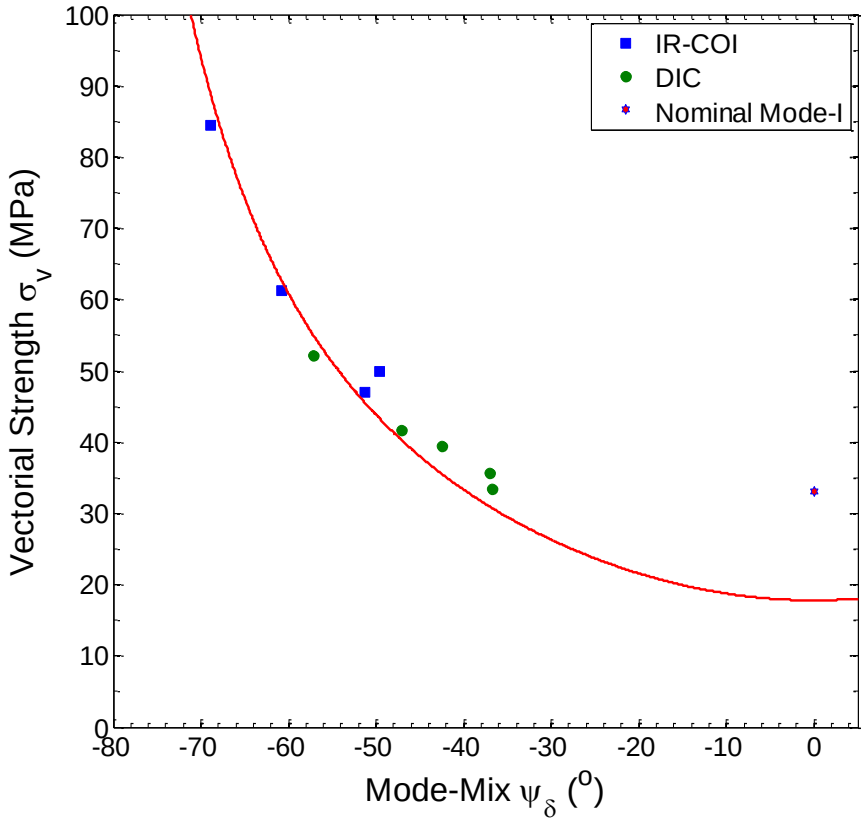

Figure 3.32: Mode dependence of the vectorial strength

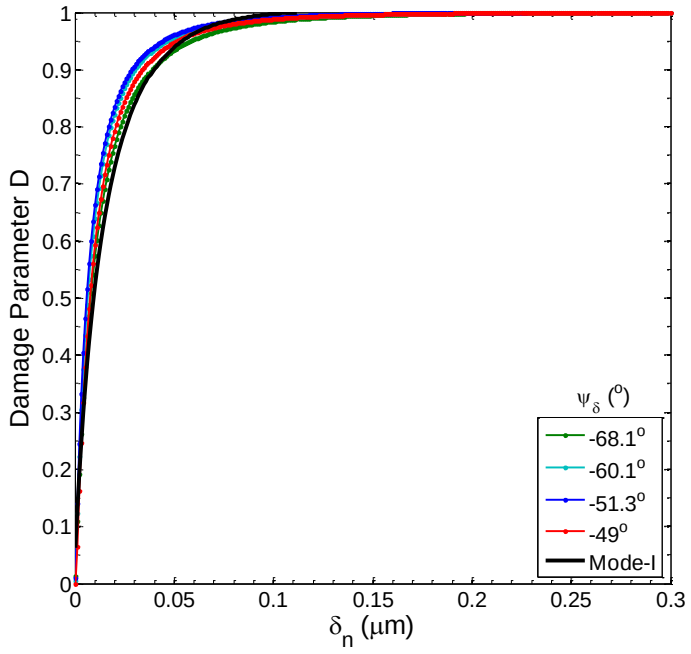

(a)

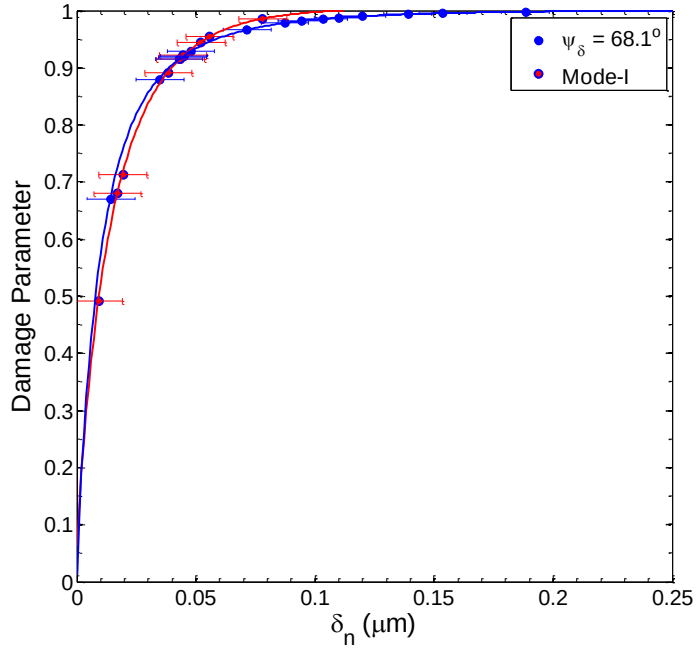

(b)

Figure 3.33: (a)Damage parameter of mixed-mode experiments with the mode-I experiment. (b) Error bars displaying resolution of IR-COI

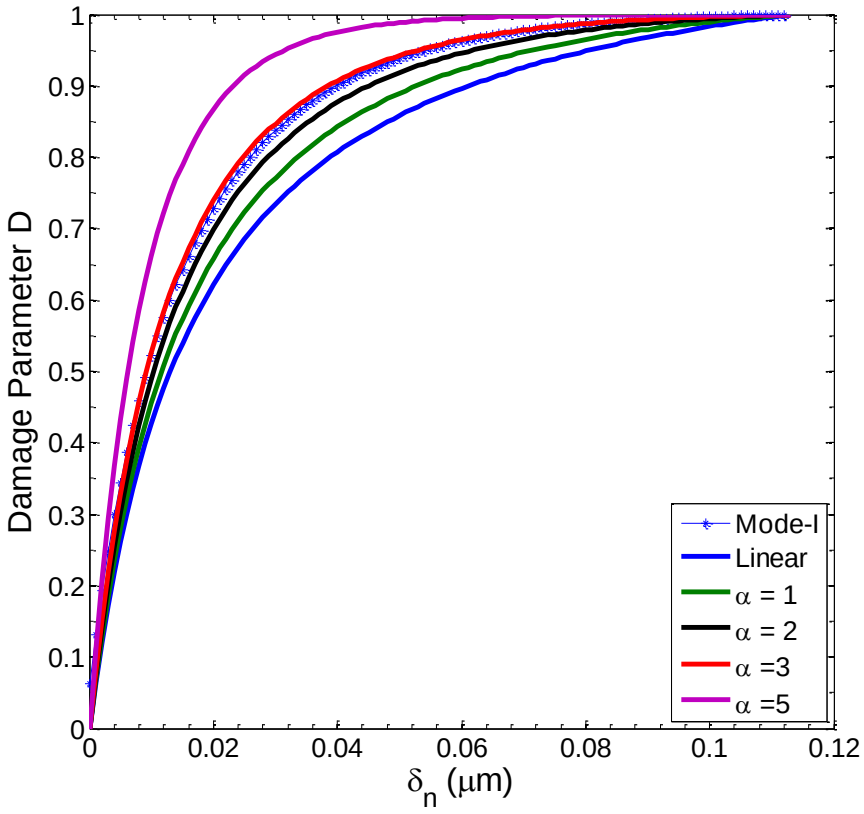

Figure 3.34: Comparison of damage evolution functions with the mode-I damage evolution

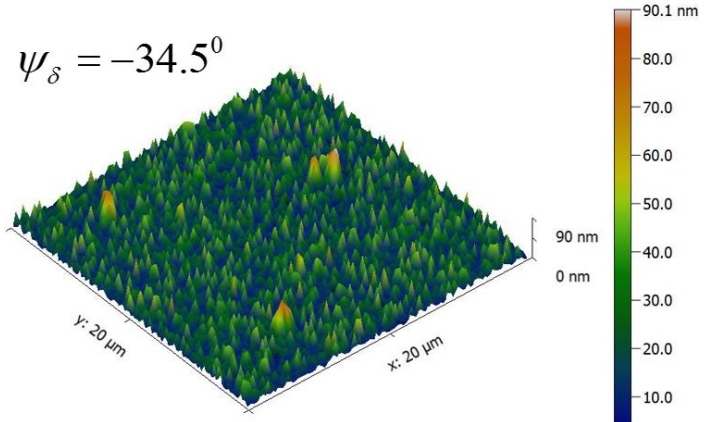

(a)

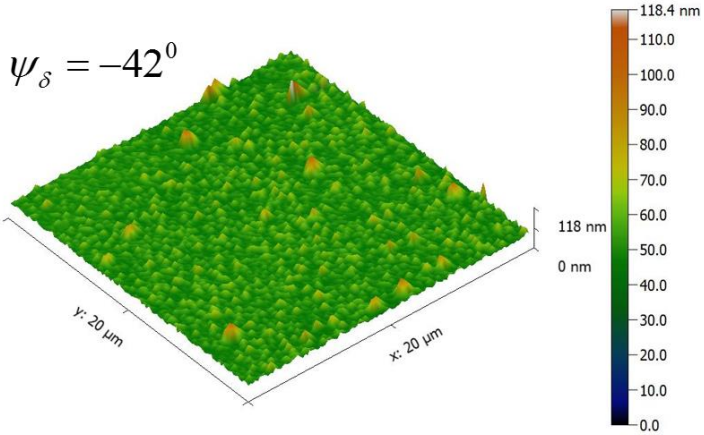

(b)

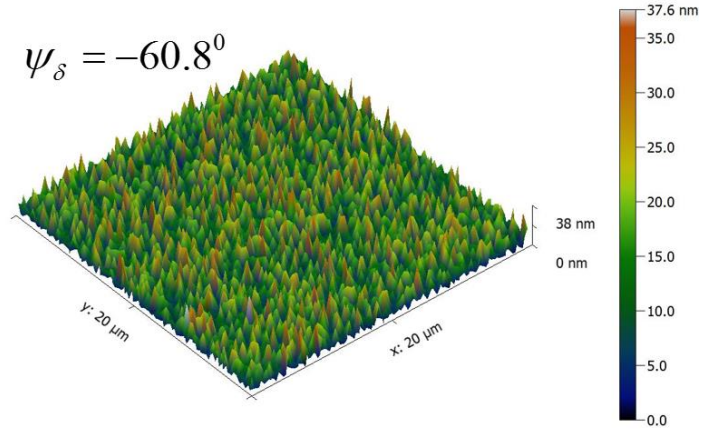

(c)

Figure 3.35 AFM images of the silicon surface (top adherend) for different mode-mix values

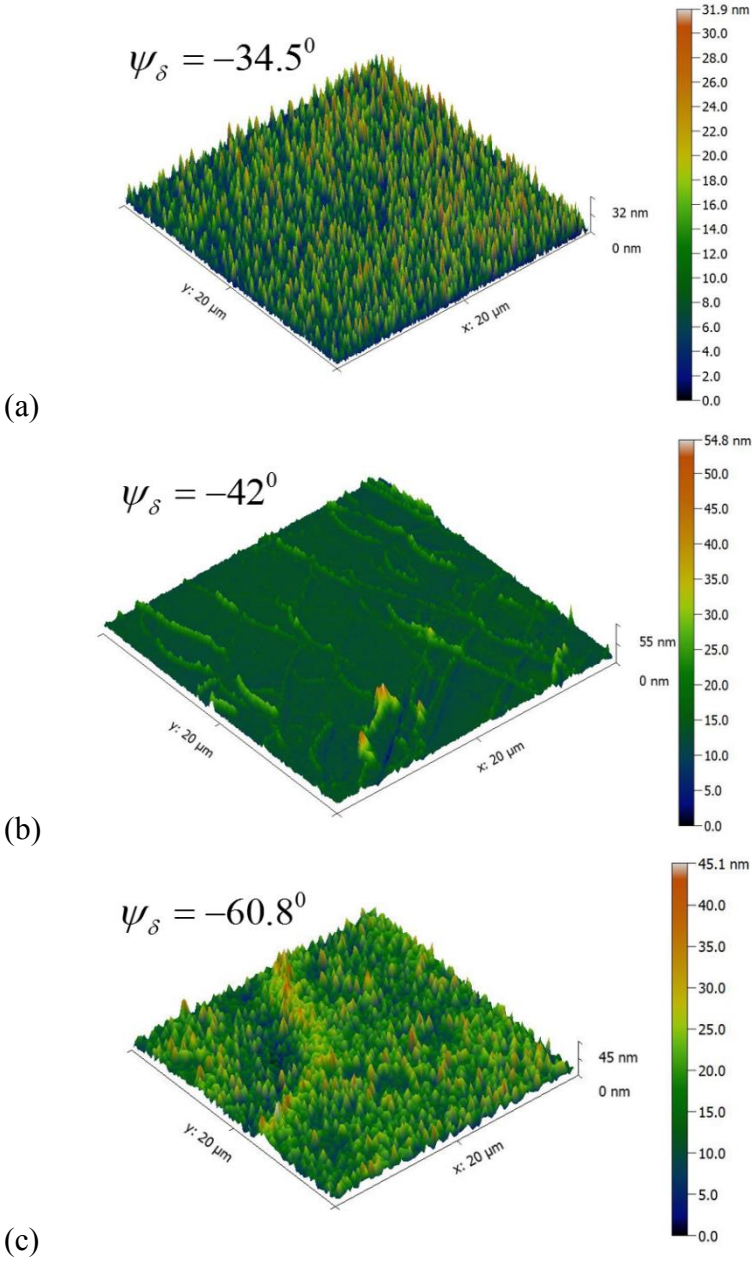

Figure 3.36 AFM images of the epoxy fracture surface (bottom adherends) for different mode-mix values.

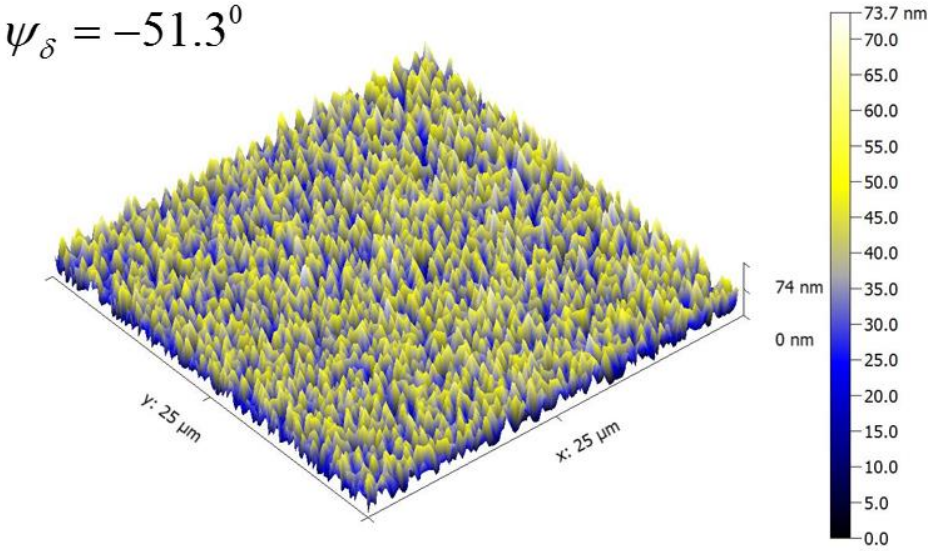

(a)

RMS roughness: 14.78 nm

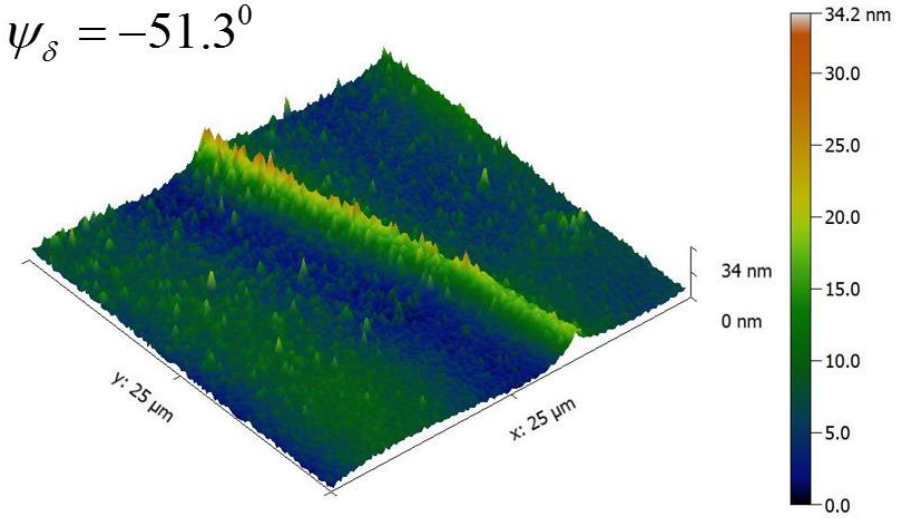

(c)

RMS roughness: 3.49 nm

Figure 3.37: AFM images of crack path (a) Au/Pd region (b) steady state propagation

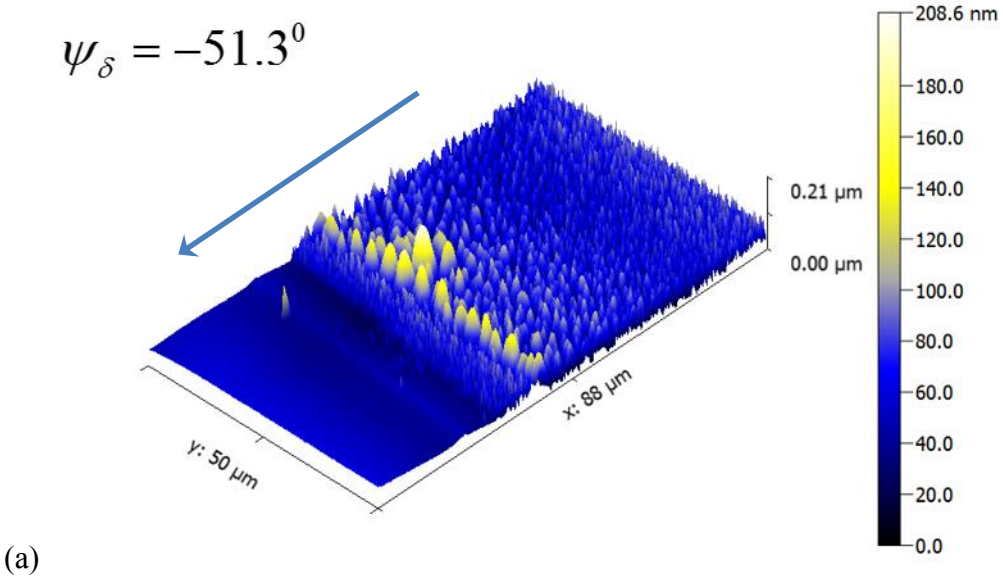

(a)

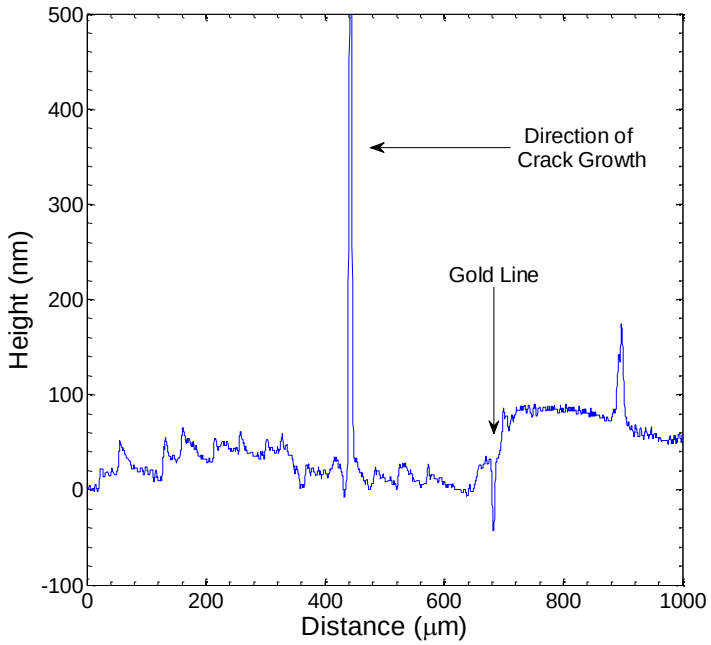

(b)

Figure 3.38: Fracture surface characterization of the initial crack front location in the bottom adherend by (a) AFM (b) stylus profilometer

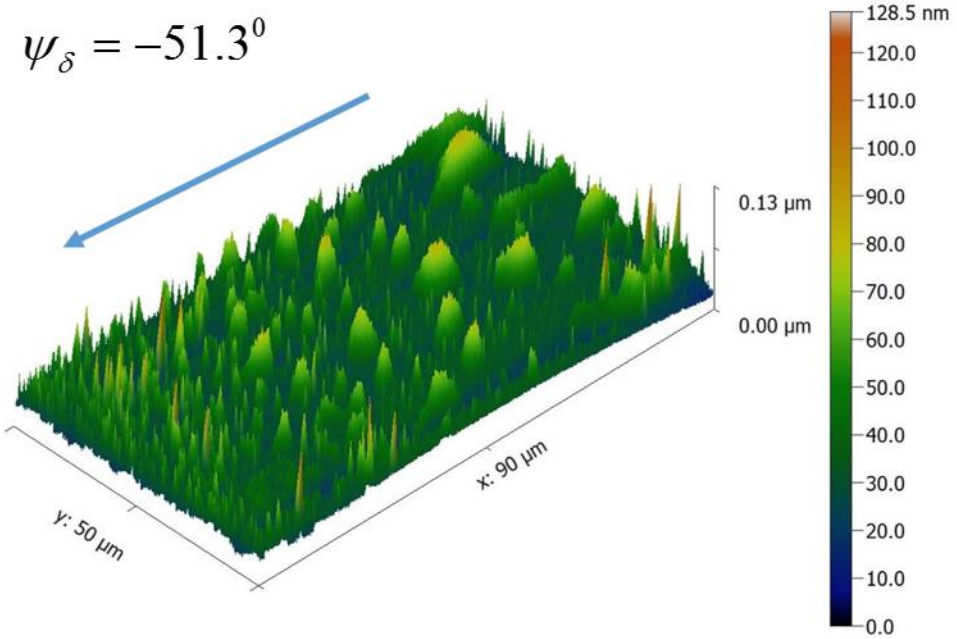

(a)

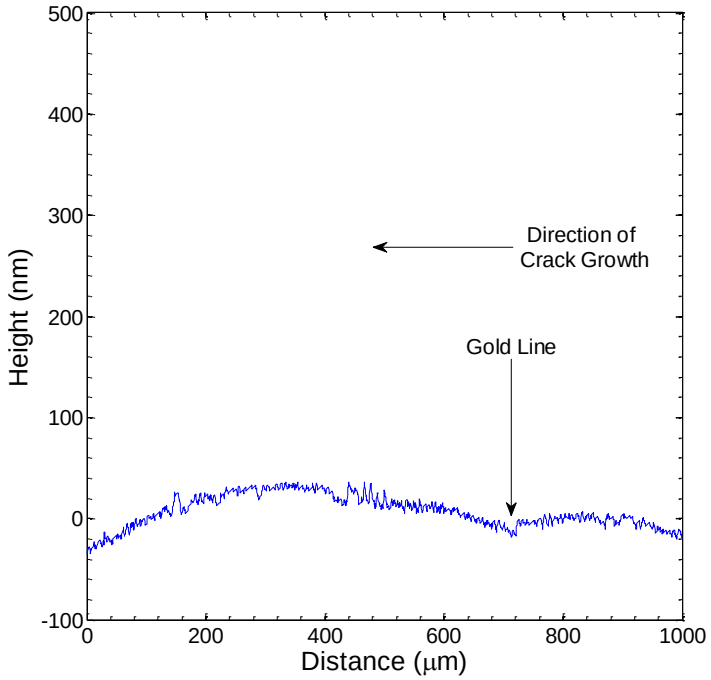

(b)

Figure 3.39: Fracture surface characterization of the initial crack front location in the top adherend by (a)AFM (b) stylus profilometer

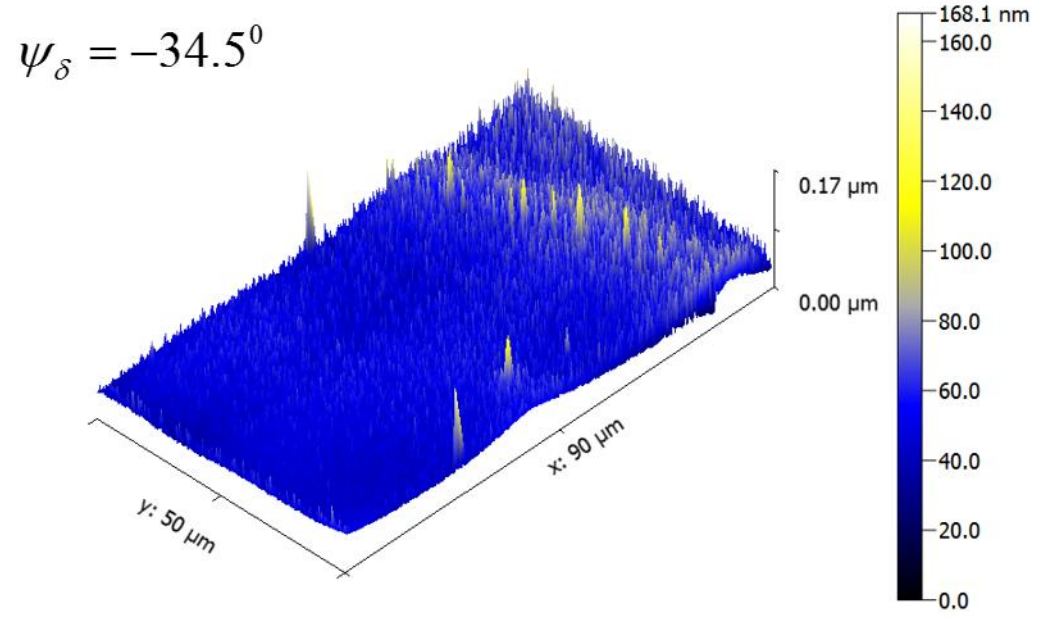

(a)

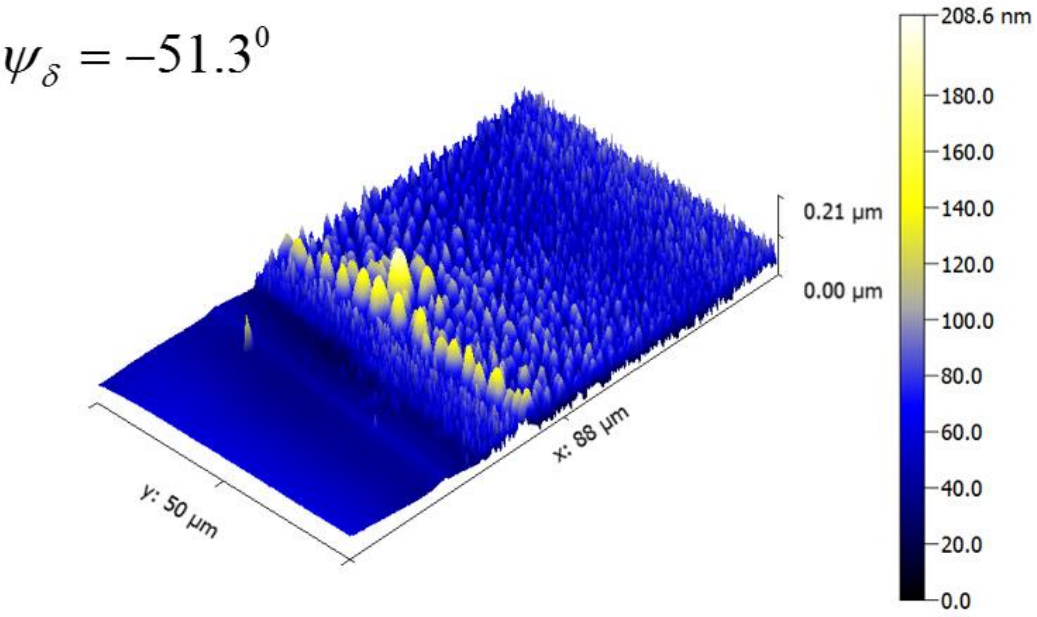

(b)

Figure 3.40: Comparison of the transition region in the bottom fracture surfaces of specimens with mode-mix values of (a) -34.5^o (b)-51.3^o.

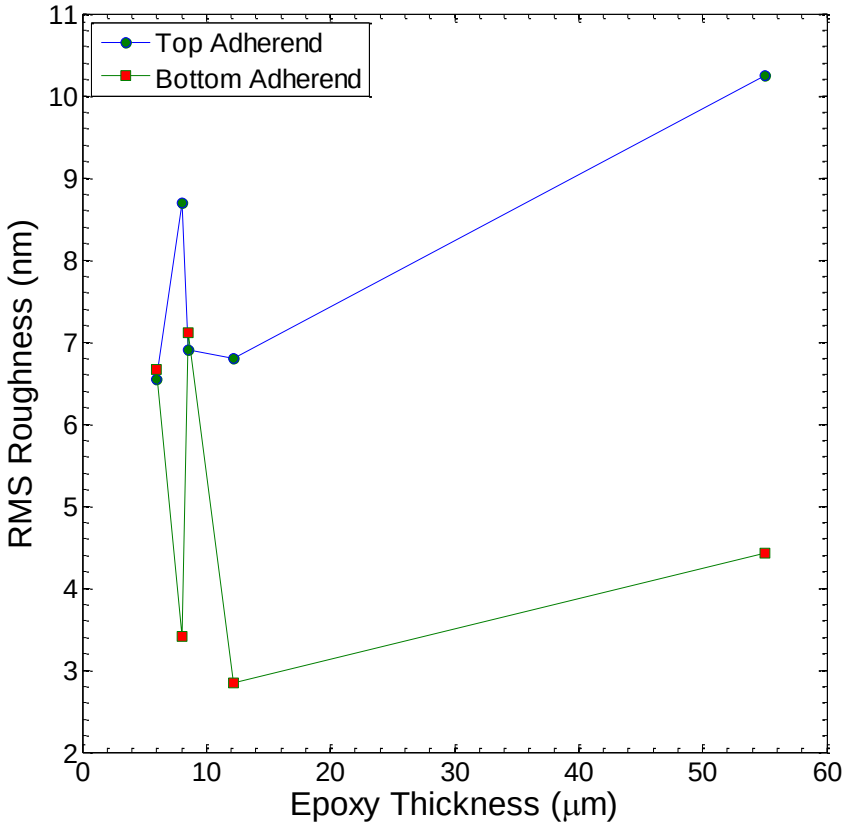

Figure 3.41: RMS roughness as a function of the epoxy thickness

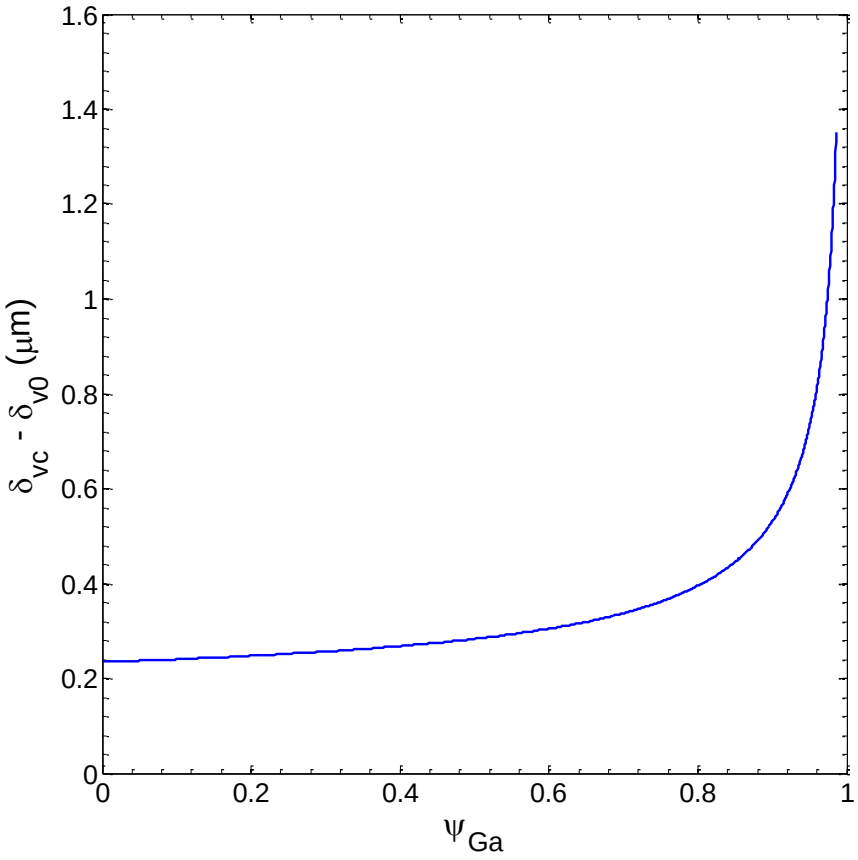

Figure 3.42: Critical effective displacement as a function of the ABAQUS mode-mix.

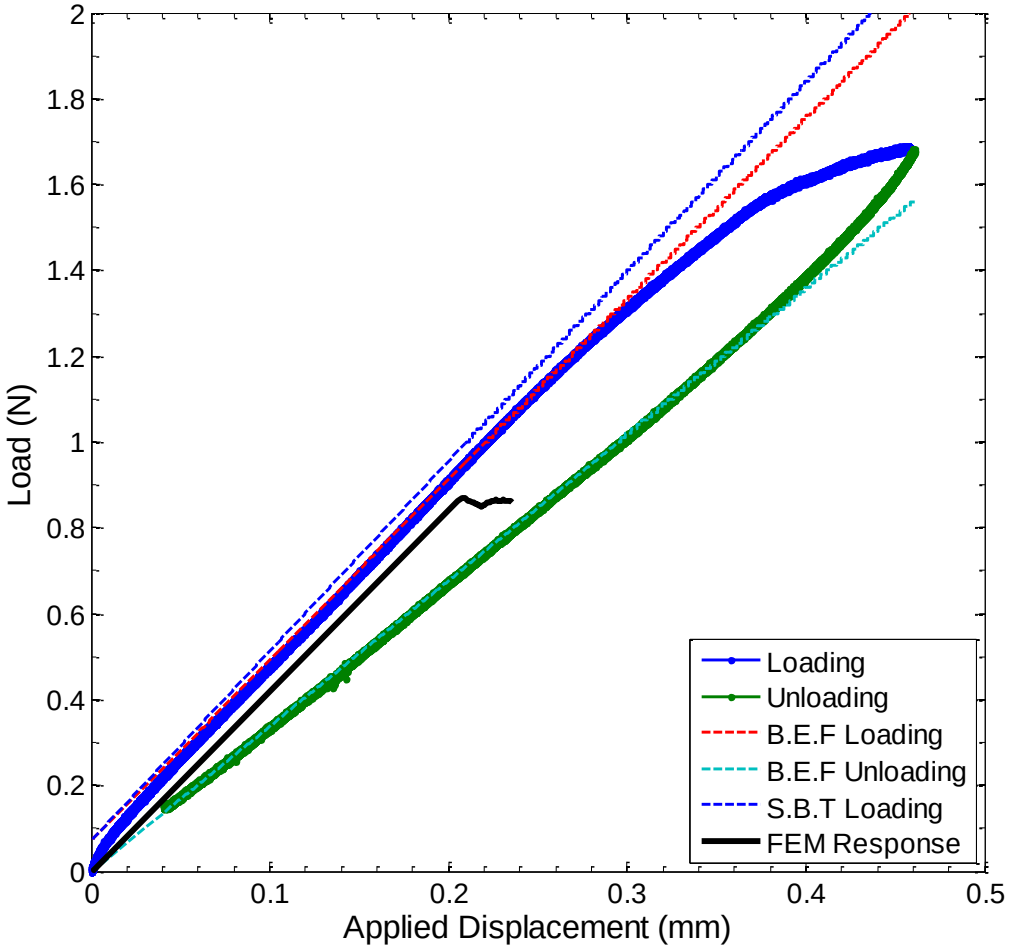

Figure 3.43: Comparison of load-displacement responses between the experiment and the FEM model. The specimen considered had an epoxy thickness of 8 μm and an initial crack length of 21.4 mm.

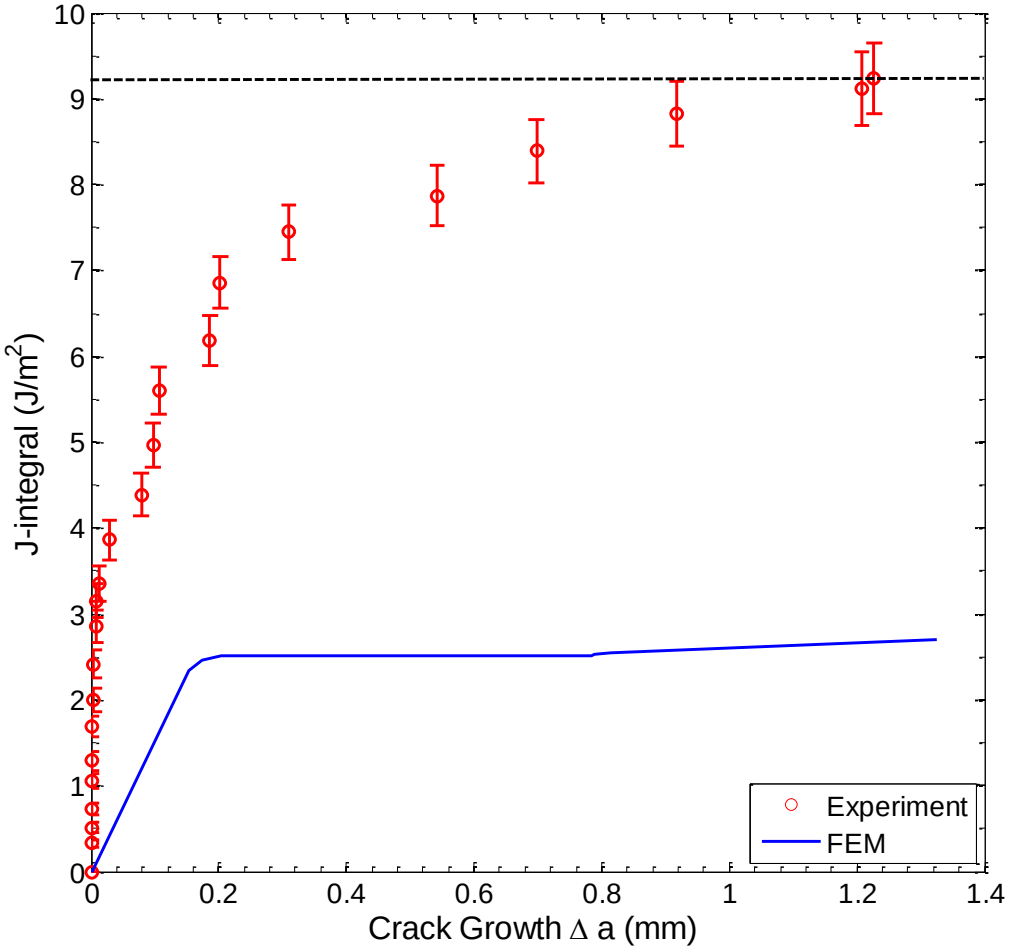

Figure 3.44: Fracture resistance curve comparison for a specimen with 8 μm thick epoxy layer

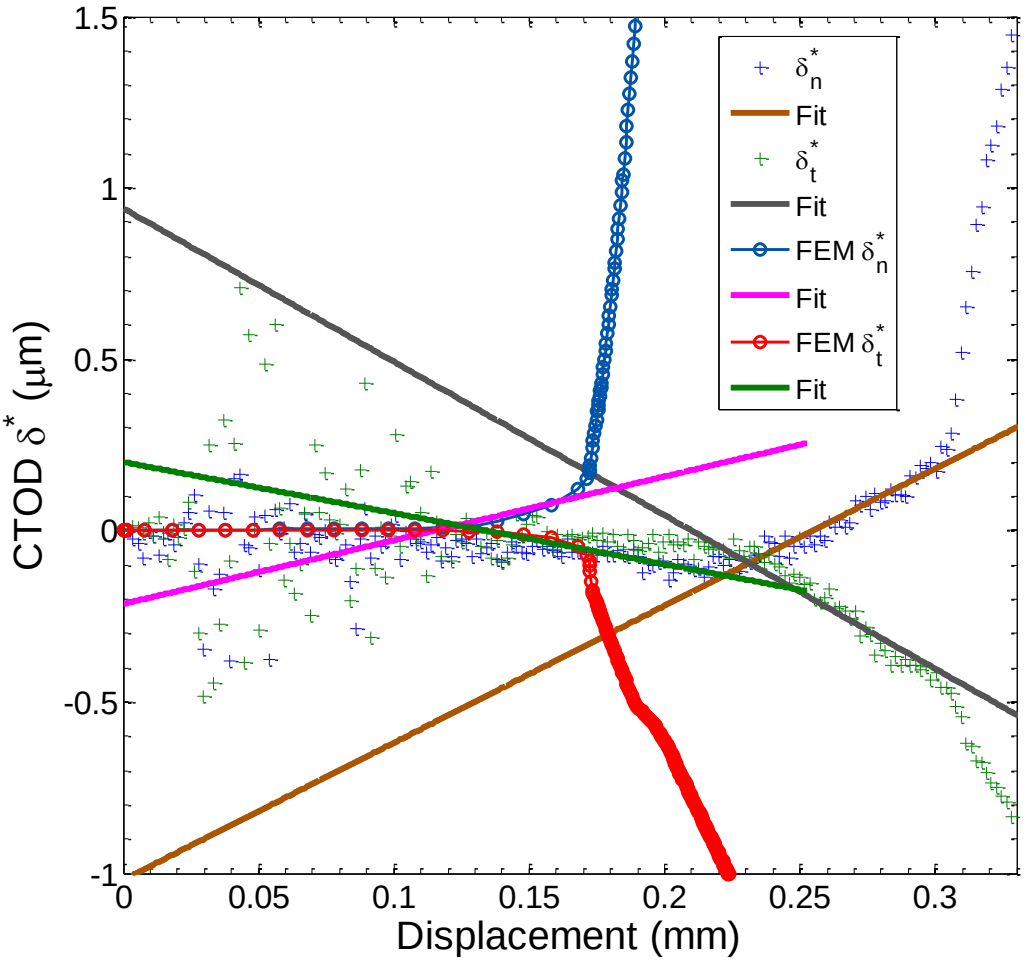

Figure 3.45 Crack tip opening displacements as a function of the applied displacement compared with DIC measurements.

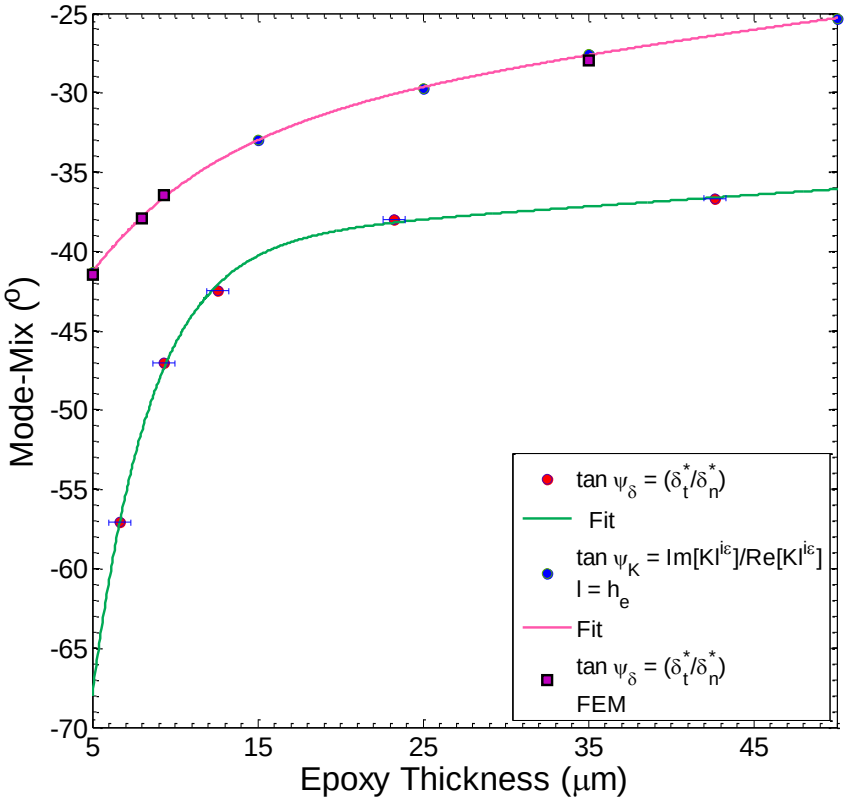

Figure 3.46: Comparison of mode-mix dependence on thickness

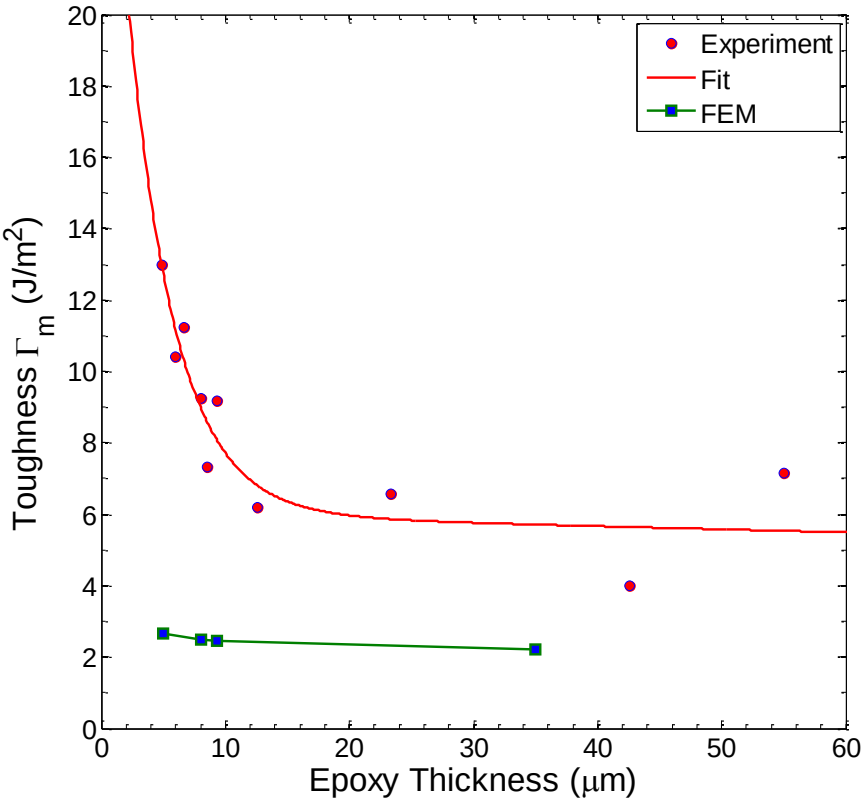

Figure 3.47 Toughness as a function of the epoxy thickness

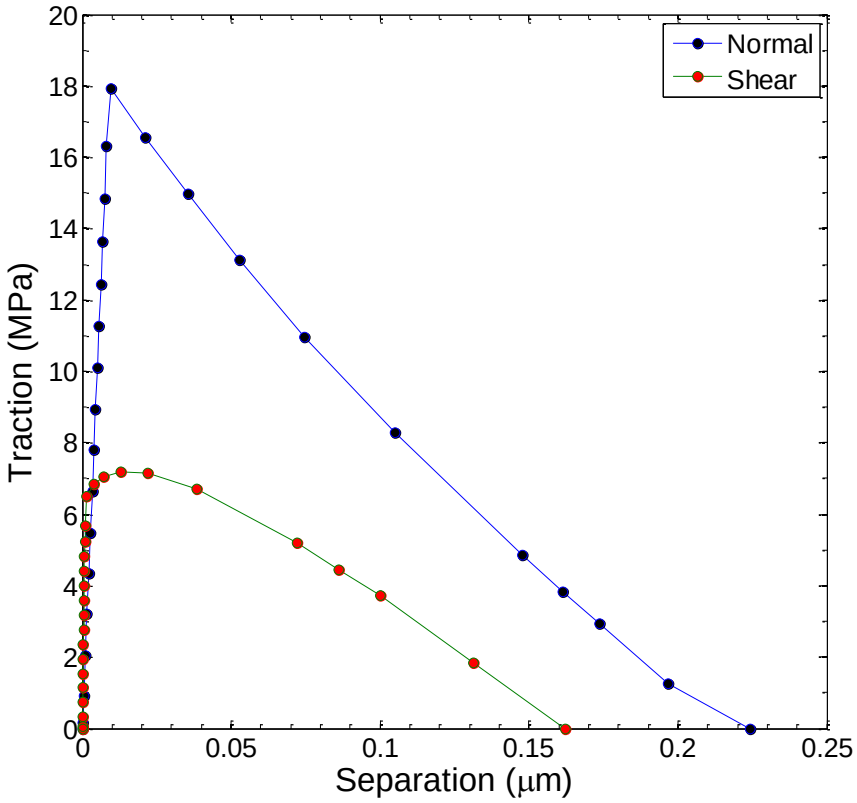

Figure 3.48: Traction separation relation from ABAQUS

TABLES

Table 2.1: Constitutive properties of silicon and epoxies.

Material	Provider	Mixing Ratio (Resin: Hardener)	Young's Modulus (GPa)	Poisson's Ratio
Silicon (111)	WRS materials	N/A	165.5	0.22
Epoxy-I	CIBA-Geigy	100:45	2.03	0.36
Epoxy-II	Huntsman	100:35	1.85	0.355

Table 2.2: Key parameters for the traction-separation relation of a silicon/epoxy interface extracted from the direct and iterative methods.

Method	Γ (J/m^2)	σ_0 (MPa)	δ_c (nm)
Direct	1.88	22.0	176
Iterative (bilinear)	1.8	18.0	200
Iterative (exponential)	1.8	18.0	450

Table 3.1: RMS roughness values of the silicon/epoxy fracture surfaces for different mode-mix values

Mode-Mix	Top (nm)	Bottom (nm)
0	0.85	1.36
-34.5	10.25	4.43
-42	6.8	2.84
-49.5	6.9	7.11
-51.3	8.7	3.41
-60.8	6.54	6.66

Table 3.2: ABAQUS input parameters for mixed-mode traction-separation relation

Region	Form	Values
Elastic	Linear	$K_n = 2 \text{ x } 10^{15}$ N/m^3 $K_t = 4.36 \text{ x } 10^{15}$ N/m^3
Damage Initiation	Quadratic Stress Criterion	$\sigma_0 = 18$MPa $\tau_0 = 1$GPa
Damage Evolution: Driving Parameter	Displacement	
Damage Evolution: Softening	Exponential	$\alpha = 1$
Damage Evolution: Mixed-Mode Behavior	Tabular	Figure 3.42

References

Alfano, G. (2006). *"On the influence of the shape of the interface law on the application of cohesive-zone models"*, Composites Science and Technology **66**(6): 723-730.

Allen, K. W. (1993). *"Some reflections on contemporary views of theories of adhesion"*, International Journal of Adhesion and Adhesives **13**(2): 67-72.

Andersson, T. and U. Stigh (2004). *"The stress–elongation relation for an adhesive layer loaded in peel using equilibrium of energetic forces"*, International Journal of Solids and Structures **41**(2): 413-434.

Auersperg, J., et al. (2010). *"VCCT and integral concepts of bi-material interface fracture in low-k structures- Going to understand relation"*. Electronics Packaging Technology Conference 12th, Singapore.

Bao, G. and Z. Suo (1992). *"Remarks on crack-bridging concepts"*, Applied Mechanics Reviews **45**(8): 355-366.

Barenblatt, G. I. (1962). *"The mathematical theory of equilibrium cracks in brittle fracture"*, Advances in Applied Mechanics **7**: 55-129.

Barrett, J. D. and R. O. Foschi (1977). *"Mode II stress-intensity factors for cracked wood beams"*, Engineering Fracture Mechanics **9**(2): 371-378.

Bateup, B. O. (1981). *"Surface chemistry and adhesion"*, International Journal of Adhesion and Adhesives **1**(5): 233-239.

Bay, B. K., et al. (1999). *"Digital volume correlation: Three-dimensional strain mapping using X-ray tomography"*, Experimental Mechanics **39**(3): 217-226.

Bing, P., et al. (2009). *"Measurement of coefficient of thermal expansion of films using digital image correlation method"*, Polymer Testing **28**(1): 75-83.

Bing, Q. and B. D. Davidson (2010). *"An improved methodology for measuring the interfacial toughness of sandwich beams"*. Major accomplishments in composite materials and sandwich structures: An anthology of ONR sponsored research. I. M. Daniels , E. E. Gdoutos and Y. D. S. Rajapakse, Springer**:** 365-380.

Birringer, R. P., et al. (2011). *"High yield four-point bend thin film adhesion testing techniques"*, Engineering Fracture Mechanics **78**(12): 2390-2398.

Brantley, W. A. (1973). *"Calculated elastic constants for stress problems associated with semiconductor devices"*, Journal of Applied Physics **44**(1): 534-535.

Cao, H. C., and Evans, A.G. (1989). *"An experimental study of the fracture resistance of bimaterial interfaces"*, Mechanics of Materials **7**: 295-304.

Chai, H. (1992). *"Experimental evaluation of mixed-mode fracture in adhesive bonds"*, Experimental Mechanics(December): 296-303.

Chai, H. and S. Mall (1988). *"Design aspects of the end-notched adhesive joint specimen"*, International Journal of Fracture **8**: 3-8.

Chai, Y. S. and K. M. Liechti (1991). *"Biaxial loading experiments for determining interfacial fracture toughness"*, Journal of Applied Mechanics **58**: 680-687.

Chai, Y. S. and K. M. Liechti (1992). *"Asymmetric shielding in interfacial fracture under in-plane shear"*, Journal of Applied Mechanics **59**(2): 295-304.

Charalambides, P. G., Cao, H.C., Lund, J., Evans, A.G. (1990). *"Development of a test specimen for measuring the mixed mode fracture resistance of bimaterial interfaces"*, Mech. of Materials(8): 269-283.

Charalambides, P. G., et al. (1989). *"A test specimen for determining the fracture resistance of bimaterial interfaces"*, Journal of Applied Mechanics **56**: 77-82.

Chasiotis, I. and W. Knauss (2002). *"A new microtensile tester for the study of MEMS materials with the aid of atomic force microscopy"*, Experimental Mechanics **42**(1): 51-57.

Choi, S. H., et al. (2001). *"Fracture of a ductile layer constrained by stiff substrates"*, Fatigue and Fracture of Engineering Materials and Structures **23**: 1-13.

Chow, C. L., et al. (1979). *"On the determination and application of COD to epoxy-bonded aluminum joints"*, Journal of Strain Analysis for Engineering Design **14**(2): 37-42.

Chu, T. C., et al. (1985). *"Applications of digital-image-correlation techniques to experimental mechanics"*, Experimental Mechanics **25**(3): 232-244.

Comer, A. J., et al. (2013). *"Characterising the behaviour of composite single lap bonded joints using digital image correlation"*, International Journal of Adhesion and Adhesives **40**: 215-223.

Comninou, M. (1977). *"The interface crack"*, Journal of Applied Mechanics **44**(4): 631-636.

Comninou, M., and Schmueser, D. (1979). *"The interface crack in a combined tension-compression and shear field"*, Journal of Applied Mechanics **46**: 345-348.

Cox, B. N. and D. B. Marshall (1991). *"The determination of crack bridging forces"*, International Journal of Fracture **49**(3): 159-176.

Dauskardt, R. H., et al. (1998). *"Adhesion and debonding of multi-layer thin film structures"*, Engineering Fracture Mechanics **61**(1): 141-162.

Davidson, B. D. and V. Sundararaman (1996). *"A single leg bending test for interfacial fracture toughness determination"*, International Journal of Fracture **78**(2): 193-210.

Dolbow, J. and M. Gosz (1996). *"Effect of out-of-plane properties of a polyimide film on the stress fields in microelectronic structures"*, Mechanics of Materials **23**(4): 311-321.

Downing, T. D., et al. (2000). *"Determining the interphase thickness and properties in polymer matrix composites using phase imaging atomic force microscopy and nanoindentation"*, Journal of Adhesion Science & Technology **14**(14): 1801-1812.

Drzal, L. T. (1986). *"The interphase in epoxy composites"*. Epoxy Resins and Composites II : Advances in Polymer Science. K. Dusek, Springer Berlin Heidelberg. **75:** 1-32.

Dugdale, D. S. (1960). *"Yielding of steel sheets containing slits"*, Journal of the Mechanics and Physics of Solids **8**(2): 100-104.

Dundurs, J. (1969). *"Edge-bonded dissimilar orthogonal elastic wedges"*, Journal of Applied Mechanics: 36, 650-652.

Dundurs, J. (1978). *"The interface crack"*, Journal of Applied Mechanics-Transactions of the Asme **45**(3): 700-700.

Elices, M., et al. (2002). *"The cohesive zone model: advantages, limitations and challenges"*, Engineering Fracture Mechanics **69**(2): 137-163.

Evans, A. G., et al. (1989). *"On crack path selection and the interface fracture energy in bimaterial systems"*, Acta Metallurgica **37**(12): 3249-3254.

Fan, L., et al. (2002). *"Adhesion of underfill and components in flip chip encapsulation"*, Journal of Adhesion Science & Technology **16**(2): 213-223.

Feraren, P. and H. M. Jensen (2004). *"Cohesive zone modeling of interface fracture near flaws in adhesive joints"*, Engineering Fracture Mechanics **71**(15): 2125-2142.

Ferguson, T. and J. Qu (2003). *"Moisture absorption analysis of interfacial fracture test specimens composed of no-flow underfill materials"*, Journal of Electronic Packaging **125**(1): 24-30.

Ferguson, T. P. and J. Qu (2004). *"Moisture and temperature effects on the reliability of interfacial adhesion of a polymer/metal interface"*. Electronic Components and Technology Conference, 2004. Proceedings. 54th.

Fichter, W. B. (1983). *"The stress intensity factor for the double cantilever beam"*, International Journal of Fracture **22**: 133-143.

Fleck, N. A., et al. (1991). *"Crack path selection in a brittle adhesive layer"*, International Journal of Solids and Structures **27**(13): 1683-1703.

Fung, Y. C. (1965)."*Foundations of solid mechanics"*. Englewood Cliffs, New Jersey, Prentice Hall Inc.

Gain, A. L., et al. (2011). *"A hybrid experimental/numerical technique to extract cohesive fracture properties for mode-I fracture of quasi-brittle materials"*, International Journal of Fracture **169**(2): 113-131.

Gent, A. N. (1981). *"The role of chemical bonding in the adhesion of elastomers"*, International Journal of Adhesion and Adhesives **1**(4): 175-180.

Gent, A. N., et al. (1997). *"Autohesion of crosslinked polyethylene"*, Journal of Polymer Science Part B: Polymer Physics **35**(4): 615-622.

Gillis, P. P. and J. J. Gilman (1964). *"Double-cantilever cleavage mode of crack propagation"*, Journal of Applied Physics **35**(3): 647-658.

Gledhill, R. A., et al. (1990). *"Durability of adhesive-bonded joints employing organosilane coupling agents"*, International Journal of Adhesion and Adhesives **10**(3): 192-198.

González-Benito, J. (2003). *"The nature of the structural gradient in epoxy curing at a glass fiber/epoxy matrix interface using FTIR imaging"*, Journal of Colloid and Interface Science **267**(2): 326-332.

Gowrishankar, S., et al. (2012). *"A comparison of direct and iterative methods for determining traction-separation relations"*, International Journal of Fracture **177**(2): 109-128.

Hall, J. J. (1967). *"Electronic effects in the elastic constants of n-type silicon"*, Physical Review **161**(3): 756-761.

He, M.-Y. and J. W. Hutchinson (1989). *"Crack deflection at an interface between dissimilar elastic materials"*, International Journal of Solids and Structures **25**(9): 1053-1067.

Ho, P. S., et al. (2004). *"Reliability issues for flip-chip packages"*, Microelectronics Reliability **44**(5): 719-737.

Högberg, J. L., et al. (2007). *"Constitutive behaviour of mixed mode loaded adhesive layer"*, International Journal of Solids and Structures **44**(25-26): 8335-8354.

Hölck, O., et al. (2012). *"Comparative characterization of chip to epoxy interfaces by molecular modeling and contact angle determination"*, Microelectronics Reliability **52**(7): 1285-1290.

Hutchinson, J. W. and A. G. Evans (2000). *"Mechanics of materials: Top-down approaches to fracture"*, Acta Materialia **48**(1): 125-135.

Hutchinson, J. W., et al. (1987). *"Crack paralleling an interface between dissimilar elastic materials"*, Journal of Applied Mechanics **54**: 828-832.

Hutchinson, J. W. and Z. Suo (1992). *"Mixed Mode Cracking in Layered Materials"*, Advances in Applied Mechanics **29**: 64-191.

Kamer, A., et al. (2011). *"Adhesion and degradation of hard coatings on poly (methyl methacrylate) substrates"*, Thin Solid Films **519**(6): 1907-1913.

Kandula, S. S., et al. (2005). *"Cohesive modeling of quasi-static fracture in functionally graded materials"*, Journal of Applied Mechanics **73**(5): 783-791.

Kanninen, M. F. (1973). *"An augmented double cantilever beam model for studying crack propagation and arrest"*, International Journal of Fracture **9**(1): 83-92.

Kehoe, L., et al. (2006). *"Measurement of deformation and strain in first level C4 interconnect and stacked die using optical digital image correlation"*. Electronic Components and Technology Conference, 2006. Proceedings. 56th.

Kinloch, A. J. (1980). *"The science of adhesion. Part I: Surface and interfacial aspects"*, Journal of Materials Science **15**(9): 2141-2166.

Kolluri, M., et al. (2009). *"In-situ characterization of interface delamination by a new miniature mixed mode bending setup"*, International Journal of Fracture **158**(2): 183-195.

Kysar, J. W. (2001). *"Crack-opening interferometry at interfaces of transparent materials and metals"*, Experimental Mechanics **41**(1): 52-57.

Lecompte, D., et al. (2007). *"Study and generation of optimal speckle patterns for DIC"*. SEM Annual Conference & Exposition on Experimental and Applied Mechanics, Springfield, MA.

Li, S., et al. (2005). *"Use of mode-I cohesive-zone models to describe the fracture of an adhesively-bonded polymer-matrix composite"*, Composites Science and Technology **65**(2): 281-293.

Li, S., et al. (2006). *"Mixed-mode cohesive-zone models for fracture of an adhesively bonded polymer–matrix composite"*, Engineering Fracture Mechanics **73**(1): 64-78.

Li, S., et al. (2004). *"The effects of shear on delamination in layered materials"*, Journal of the Mechanics and Physics of Solids **52**(1): 193-214.

Liang, Y. M. and K. M. Liechti (1995). *"Toughening mechanisms in mixed-mode interfacial fracture"*, International Journal of Solids and Structures: 32, 957-978.

Liang, Y. M. and K. M. Liechti (1996). *"On the large deformation and localization behavior of an epoxy resin under multiaxial stress states"*, International Journal of Solids and Structures **33**(10): 1479-1500.

Liechti, K. M. (1993). *"On the use of classical interferometry techniques in fracture mechanics"*. Experimental Techniques in Fracture, III. J. S. Epstein. New York, VCH Publishers**:** 95-124.

Liechti, K. M. (1993). *"On the use of classical interferometry techniques in fracture mechanics"*. Experimental techniques in fracture. J. S. Epstein. New York, VCH Publishers**:** 95-124.

Liechti, K. M. and T. Freda (1989). *"On the use of laminated beams for the determination of pure and mixed-mode fracture properties of structural adhesives"*, Journal of Adhesion **28**: 145-169.

Liechti, K. M. and E. C. Hanson (1988)."*An examination of mixed-mode debonding in the blister test"*. Philadelphia, American Society for Testing and Materials

Liechti, K. M. and W. G. Knauss (1982). *"Crack propagation at material interfaces II: experiments on mode interaction"*, Experimental Mechanics(October): 383-391.

Liechti, K. M. and Y. M. Liang (1992). *"The interfacial fracture characteristics of bimaterial and sandwich blister specimens"*, International Journal of Fracture **55**(2): 95-114.

Liechti, K. M. and B. Marton (2002). *"Delamination of a high-temperature sandwich plate"*, Experimental mechanics **42**(2): 206-213.

Luo, P. F., et al. (1993). *"Accurate measurement of three-dimensional deformations in deformable and rigid bodies using computer vision"*, Experimental Mechanics **33**(2): 123-132.

Mai, K., et al. (1998). *"Interphase characterization in composites with new non-destructive methods"*, Composites Part A: Applied Science and Manufacturing **29**(9–10): 1111-1119.

Mangalgiri, P. D., et al. (1986). *"Effect of adherend thickness and mixed-mode loading on debond growth in adhesively bonded composite joints"*, NASA Technical Memorandum 88992: 1-46.

Marsavina, L. and T. Piski (2010). *"Bimaterial four point bend specimen with sub-interface crack"*, International Journal of Fracture **164**(2): 325-332.

Mei, H. (2011)."*Fracture and delamination of elastic thin films on compliant substrates: modeling and simulations"*. Ph.D., The University of Texas at Austin.

Mei, H., et al. (2010). *"Initiation and propagation of interfacial delamination in integrated thin-film structures"*. Thermal and Thermomechanical Phenomena in Electronic Systems- 12th IEEE Intersociety conference (ITHERM 2010), IEEE.

Mello, A. W. (2003)."*Mixed-Mode Fracture Experiments on Quartz/Epoxy and Sapphire/Epoxy Interfaces*".

Mello, A. W. and K. M. Liechti (2004). *"A piezoelectric biaxial loading device for interfacial fracture experiments"*, Experimental Mechanics **44**(5): 495-501.

Mello, A. W. and K. M. Liechti (2006). *"The Effect of Self-Assembled Monolayers on Interfacial Fracture"*, Journal of Applied Mechanics **73**(5): 860-870.

Miller, L. F. (1969). *"Controlled collapse reflow chip joining"*, IBM Journal of Research and Development(May): 239-250.

Mohammed, I. and K. M. Liechti (2000). *"Cohesive zone modeling of crack nucleation at bimaterial corners"*, Journal of the Mechanics and Physics of Solids **48**: 735-764.

Moroni, F. and A. Pirondi (2011). *"Cohesive zone model simulation of fatigue debonding along interfaces"*, Procedia Engineering **10**: 1829-1834.

Munz, M., et al. (1998). *"The scanning force microscope as a tool for the detection of local mechanical properties within the interphase of fibre reinforced polymers"*, Composites Part A: Applied Science and Manufacturing **29**(9–10): 1251-1259.

Na, S. R., et al. (2011). *"Delamination between functionalized silicon surfaces"*. Experimental and Applied Mechanics, Volume 6. T. Proulx, Springer New York**:** 89-89.

Needleman, A. (1987). *"A continuum model for void nucleation by inclusion debonding"*, Journal of Applied Mechanics **54**: 525-531.

Needleman, A. (1990). *"An analysis of tensile decohesion along an interface"*, Journal of the Mechanics and Physics of Solids **38**: 289-324.

Needleman, A., et al. (2010). *"Effect of an interphase region on debonding of a CNT reinforced polymer composite"*, Composites Science and Technology **70**(15): 2207-2215.

Ohring, M. (2001)."*Materials Science of Thin Films"*. San Diego, CA, Academic Press.

Packham, D. E., et al. (1974). *"Mechanical factors in the adhesion of polyethylene to aluminium"*, Journal of Applied Polymer Science **18**(11): 3237-3247.

Pan, B., et al. (2009). *"Two-dimensional digital image correlation for in-plane displacement and strain measurement: a review"*, Measurement Science and Technology **20**(6): 1-17.

Park, K. and G. H. Paulino (2011). *"Cohesive zone models: A critical review of traction-separation relationships across fracture surfaces"*, Applied Mechanics Reviews **64**: 1-20.

Park, K., et al. (2009). *"A unified potential-based cohesive model of mixed-mode fracture"*, Journal of the Mechanics and Physics of Solids **57**(6): 891-908.

Parmigiani, J. P. and M. D. Thouless (2007). *"The effects of cohesive strength and toughness on mixed-mode delamination of beam-like geometries"*, Engineering Fracture Mechanics **74**: 2675-2699.

Planas, J., et al. (2003). *"Generalizations and specializations of cohesive crack models"*, Engineering Fracture Mechanics **70**(14): 1759-1776.

Pronin, A. N. and V. Gupta (1998). *"Measurement of thin film interface toughness by using laser-generated stress pulses"*, Journal of the Mechanics and Physics of Solids **46**(3): 389-410.

Reeder, J. R. and J. R. Crews Jr. (1990). *"Mixed-mode bending method for delamination testing"*, AIAA Journal **28**(7): 1270-1276.

Rice, J. R. (1968). *"A path independent integral and the approximate analysis of strain concentrations by notches and cracks"*, Journal of Applied Mechanics: 35, 379-386.

Rice, J. R. (1988). *"Elastic fracture mechanics concepts for interfacial cracks"*, Journal of Applied Mechanics: 55, 98-103.

Rice, J. R. and G. C. Shih (1965). *"Plane problems of cracks in dissimilar media"*, Journal of Applied Mechanics **32**: 418-423.

Riney, T. D. (1961). *"Residual thermoelastic stresses in bonded silicon wafers"*, Journal of Applied Physics **32**(3): 454-454.

Sancaktar, E. (1996). *"Recent approaches in constitutive behavior and testing of structural adhesives"*, Applied Mechanics Reviews **49**(10S): S128-S138.

Schmidt, R. and J. Bell (1986). *"Epoxy adhesion to metals"*. Epoxy Resins and Composites II. K. Dušek, Springer Berlin Heidelberg. **75:** 33-71.

Scrivens, W. A., et al. (2006). *"Development of Patterns for Digital Image Correlation Measurements at Reduced Length Scales"*, Experimental Mechanics **47**(1): 63-77.

Sham, M.-L. and J.-K. Kim (2003). *"Adhesion characteristics of underfill resins with flip chip package components"*, Journal of Adhesion Science & Technology **17**(14): 1923.

Sharpe, L. H. (1972). *"The interphase in adhesion"*, The Journal of Adhesion **4**(1): 51-64.

Sharpe, L. H. and H. Schonhorn (1964). *"Surface Energetics, Adhesion, and Adhesive Joints"*. Contact Angle, Wettability, and Adhesion, AMERICAN CHEMICAL SOCIETY. **43:** 189-201.

Shen, B. and G. Paulino (2011). *"Direct Extraction of Cohesive Fracture Properties from Digital Image Correlation: A Hybrid Inverse Technique"*, Experimental Mechanics **51**(2): 143-163.

Shi, X. Q., et al. (2007). *"Determination of fracture toughness of underfill/chip interface with digital image speckle correlation technique"*, IEEE Transactions on Components and Packaging Technologies **30**(1): 101-109.

Shijian, L. and C. P. Wong (2000). *"Investigation on effect of coupling agents in epoxy based underfill material for flip chip application"*. Electronic Components & Technology Conference, 2000. 2000 Proceedings. 50th.

Shirani, A. and K. M. Liechti (1998). *"A calibrated frature process zone model for thin film blistering"*, International Journal of Fracture **93**: 281-314.

Smith, T. S., et al. (2002). *"Digital volume correlation including rotational degrees of freedom during minimization"*, Experimental Mechanics **42**(3): 272-278.

Soles, C. L. and A. F. Yee (2000). *"A discussion of the molecular mechanisms of moisture transport in epoxy resins"*, Journal of Polymer Science Part B: Polymer Physics **38**(5): 792-802.

Song, S. H., et al. (2008). *"Influence of the cohesive zone model shape parameter on asphalt concrete fracture behavior"*. AIP Conference 2008, AIP.

Sørensen, B. F. and T. K. Jacobsen (2003). *"Determination of cohesive laws by the J integral approach"*, Engineering Fracture Mechanics **70**(14): 1841-1858.

Sørensen, B. F. and P. Kirkegaard (2006). *"Determination of mixed mode cohesive laws"*, Engineering Fracture Mechanics **73**(17): 2642-2661.

Sorensen, L., et al. (2008). *"Bridging tractions in mode I delamination: Measurements and simulations"*, Composites Science and Technology **68**(12): 2350-2358.

Sperandio, C., et al. (2010). *"Characterization of the interphase in an aluminium/epoxy joint by using controlled pressure scanning electron microscopy coupled with an energy dispersive X-ray spectrometer"*, Micron **41**(2): 105-111.

Stigh, U. and T. Andersson (2000). *"An experimental method to determine the complete stress-elongation relation for a structureal adhesive layer loaded in peel"*, ESIS Publication 27**:** 297-306.

Sun, Y. and J. H. L. Pang (2008). *"Digital image correlation for solder joint fatigue reliability in microelectronics packages"*, Microelectronics Reliability **48**(2): 310-318.

Sun, Z., et al. (1997). *"Measuring microscopic deformations with digital image correlation"*, Optics and Lasers in Engineering **27**: 409-428.

Sundararaman, V. and B. D. Davidson (1997). *"An unsymmetric double cantilever beam test for interfacial fracture toughness determination"*, International Journal of Solids and Structures **34**(7): 799-817.

Suo, Z. and J. W. Hutchinson (1988). *"Sandwich test specimens for measuring interface crack toughness"*. Interfacial phenomena in composites: Processing, characterization and mechanical properties, Newport, R.I., Elsevier Sequoia.

Suryanarayana, D., et al. (1991). *"Enhancement of flip-chip fatigue life by encapsulation"*, IEEE Transactions on Components, Hybrids, and Manufacturing Technology, **14**(1): 218-223.

Swadener, J. G. (1998)."*Primary fracture toughness mechanisms of a glass / epoxy interface"*.

Swadener, J. G. and K. M. Liechti (1998). *"Asymmetric shielding mechanisms in the mixed-mode fracture of a glass/epoxy interface"*, Journal of Applied Mechanics **65**(1): 25-29.

Swadener, J. G., et al. (1999). *"The intrinsic toughness and adhesion mechanisms of a glass/epoxy interface"*, Journal of the Mechanics and Physics of Solids **47**(2): 223-258.

Taliercio, A. (2007). *"Macroscopic strength estimates for metal matrix composites embedding a ductile interphase"*, International Journal of Solids and Structures **44**(22–23): 7213-7238.

Thouless, M. D. (1994). *"Fracture mechanics of thin films"*, IBM Journal of Research and Development **38**(4): 367-377.

Tilbrook, M. T., et al. (2005). *"Effects of plastic yielding on crack propagation near ductile/brittle interfaces"*, Acta Materialia **53**(14): 3935-3949.

Ting, T. C. T. (1995). *"Generalized Dundurs constants for anisotropic bimaterials"*, International Journal of Solids and Structures **32**(3–4): 483-500.

Tvergaard, V. and J. W. Hutchinson (1992). *"The relation between crack growth resistance and fracture process parameters in elastic-plastic solids"*, Journal of the Mechanics and Physics of Solids **40**(6): 1377-1397.

Valoroso, N. and L. Champaney (2006). *"A damage-mechanics-based approach for modelling decohesion in adhesively bonded assemblies"*, Engineering Fracture Mechanics **73**(18): 2774-2801.

Vendroux, G. and W. G. Knauss (1998). *"Submicron deformation field measurements: Part 2. Improved digital image correlation "*, Experimental Mechanics **38**(2): 86-92.

Voi͡u͡tskiĭ, S. S. (1963)."*Autohesion and adhesion of high polymers"*, Wiley.

Volinsky, A. A., et al. (2002). *"Interfacial toughness measurements for thin films on substrates"*, Acta Materialia **50**: 441-466.

Volokh, K. Y. (2004). *"Comparison between cohesive zone models"*, Communications in Numerical Methods in Engineering **20**(11): 845-856.

Wake, W. C. (1978). *"Theories of adhesion and uses of adhesives: a review"*, Polymer (Guilford) **19**(3): 291-308.

Wang, H. and T. Vukanh (1996). *"Use of end-loaded-split (ELS) test to study stable fracture behavior of composites under mode-II loading"*, Composite Structures **36**: 71-79.

Wang, J.-S., and Suo Z. (1990). *"Experimental determination of interfacial toughness curves using Brazil Nut sandwiches"*, Acta. Metall. Mater. **38**: 1279-1290.

Wang, M., Liechti, K. M., White, R. M., and Winter, R. M. (2004). *"Nanoindentation of polymeric thin films with an interfacial force microscope"*, J. Mech. Phys. Solids: 52(10), 2329-2354.

Wiederhorn, S. M., et al. (1968). *"Critical analysis of the theory of the double cantilever method of measuring fracture-surface energies"*, Journal of Applied Physics **39**(3): 1569-1572.

Williams, J. G. (1989). *"End corrections for orthotropic DCB specimens"*, Composites Science and Technology **35**(4): 367-376.

Williams, J. G. and H. Hadavinia (2002). *"Analytical solutions for cohesive zone models"*, Journal of the Mechanics and Physics of Solids **50**(4): 809-825.

Williams, M. L. (1959). *"The stresses around a fault or crack in dissimilar media"*, Bulletin of the Seismological Society of America **49**(2): 199-204.

Yang, Q. D. and M. D. Thouless (2001). *"Mixed-mode fracture analyses of plastically-deforming adhesive joints"*, International Journal of Fracture **110**(2): 175-187.

Yang, S., et al. (2011). *"Modeling of separation behavior of epoxy/Cu interface using molecular dynamics simulation"*. Electronic Components and Technology Conference, IEEE 61st, Lake Buena Vista, FL.

Yang, S., et al. (2013). *"A molecular dynamics study of tensile strength between a highly-crosslinked epoxy molding compound and a copper substrate"*, Polymer **54**(18): 5064-5074.

Yu, H. H. and J. W. Hutchinson (2002). *"Influence of substrate compliance on buckling delamination of thin films"*, International Journal of Fracture **113**: 39-55.

Zhu, Y., et al. (2009). *"Direct extraction of rate-dependent traction–separation laws for polyurea/steel interfaces"*, International Journal of Solids and Structures **46**(1): 31-51.

Vita

Shravan Gowrishankar, the son of C. Gowrisankaran and Jayanthi Gowrishankar was born in Chennai, Tamil Nadu, India. After graduating high school from Rajhans Vidhyalay in Mumbai in 2003, he entered the National Institute of Technology at Trichy, India. He obtained his Bachelors of Technology degree in Metallurgical and Materials Engineeirng in 2007 graduating first class with distinction. He entered the Materials Science and Engineering PhD Program at the University of Texas at Austin in the Fall of 2007. In July 2010, he married Phrabha Shalini Raman in Chennai, India.

Email Address: shravan.g.shankar@gmail.com

This dissertation was typed by Shravan Gowrishankar.